Tungsten-Based Photoelectrodes for Photoelectrochemical Solar Energy Conversion

(Photoelektroden auf Wolframbasis für die Photoelektrochemische Solarenergieumwandlung)

Von der Fakultät für Mathematik und Naturwissenschaften
der Carl von Ossietzky Universität Oldenburg
zur Erlangung des Grades und Titels eines

Doktors der Naturwissenschaften
(Dr. rer. nat.)

angenommene Dissertation

von Frau **Sima Nouhi**, M.Sc

"Printed and/or published with the support of the German Academic Exchange Service".

This research project was carried out from October 2017 to September 2022 at the Carl von Ossietzky University of Oldenburg, School of Mathematics and Sciences, Department of Chemistry, research group of Technical Chemistry 1, Photocatalysis & Sustainable Raw Material Production, under the supervision of Prof. Dr. Michael Wark.

Erstgutachter: Prof. Dr. Michael Wark, Universität Oldenburg

Zweitgutachter: Prof. Dr. Rüdiger Beckhaus, Universität Oldenburg

Weiterer Prüfer: Prof. Dr. Jennifer Strunk, Technische Universität München

Tag der disputation: 18 July 2024

Acknowledgment

I am greatly thankful to my supervisor, Prof. Dr. Michael Wark, for welcoming me and giving me the opportunity to work in his research group. I am grateful that he gave me the freedom to pursue my interests, and all his constant support and valuable guidance through the years.

I am grateful to Dr. Dereje Hailu Taffa for acquainting me with diverse instrumental methodologies, all his precious advice and numerous help throughout my PhD.

I would like to express my gratitude to Prof. Dr. Rüdiger Beckhaus and Prof. Dr. Jennifer Strunk for accepting to be the reviewer and examiner of my thesis.

I am thankful to Rainer Bölts, for all his technical aid within the laboratory and his assistance beyond the confines of the academic institution. Thank you to Nicole Lenkering, for her support in all administrative matters. Moreover, thank you to Marco Weers and Enno Gent for introducing me to instrumental techniques within the laboratory and Frank Schröter for always being a helpful officemate whenever I needed help.

Thanks to German Academic Exchange Service (DAAD) for their financial support during my Ph.D.

My grateful is extended to my father, who provided encouragement for my pursuit of studying abroad and the pursuit of my personal aspirations. My mother has my deepest gratitude for her constant support throughout my life, her unending love, and for the thought of me even during challenging moments. The loss of my dear oldest brother, who was a pillar of support to me since I remember, during this stage of my journey, has been an unexpected blow. I am grateful for all his support and care in my life and will never forget the memories we shared.

Finally, I am thankful to Vahid and Farideh for always being there for me during these years.

For my parents and my late brother; Khosrow.

Table of Contents

List of Figures

List of Tables

Abstract

The escalation of interest in alternative and renewable fuels for energy production has been observed in recent decades owing to the depletion of global energy resources and the surge for a more eco-friendly environment. Hydrogen, due to its sustainability and environmentally conscious nature, has been widely acknowledged as an effective, sustainable, and green fuel of the future. Photoelectrochemical (PEC) water splitting represents a well-established and potent technology to convert and store solar energy into clean H_2 from a renewable source.

The present research conducted within the context of this doctoral thesis aimed to contribute to the advancement of efficient oxide-based semiconductor photoanodes for the water oxidation reaction, which presents the kinetic bottleneck of the overall PEC water splitting reaction. The investigation has been particularly directed towards WO_3-based ternary metal oxides, $CuWO_4/WO_3$ heterojunction photoanode, which are notable for their relatively narrow band gap, enabling efficient visible light harvesting, exceptional chemical stability in neutral pH, and a highly oxidative valence band edge. The one-step hydrothermal method as a cost-effective and simple synthesis strategy, which can generate a vast array of morphologies spanning from nanowires to nanoflower structures, was implemented to synthesize the $CuWO_4/WO_3$ films. Efforts have been devoted to optimizing the intrinsic properties of the dandelion-like $CuWO_4/WO_3$ films with different hydrothermal reaction parameters. The morphological and photoelectrochemical assessments reveal that the hydrothermal synthesis's parameters have a huge impact on the morphology and photoelectrochemical performance of the $CuWO_4/WO_3$ films and the optimal dandelion-like $CuWO_4/WO_3$ heterojunction facilitates charge separation in a neutral solution.

The second part of the work was improving the efficiency of $CuWO_4/WO_3$ thin films by anchoring NiCo-layered double hydroxide (NiCo-LDH) as catalysts onto substrate. The results of the electrochemical examinations for decorated $CuWO_4/WO_3$ heterojunction with LDHs co-catalysts indicate the enhancement in photon-to-current conversion efficiency (IPCE), cathodic shift of the photocurrent onset potential and increase in the photocurrent density to 0.17 $mA \cdot cm^{-2}$ at 1.23 V vs. reversible hydrogen electrode (RHE), which is twice as large as of pristine photoanode in a neutral pH value. The promoted performance of the modified photoanode can be assigned to the faster diffusion of reactants and products and efficient proton-coupled electron transfer process due to the presence of LDHs.

Zusammenfassung

In den letzten Jahrzehnten ist das Interesse an alternativen und erneuerbaren Brennstoffen für die Energieerzeugung aufgrund der Verknappung der weltweiten Energieressourcen und dem Streben nach einer umweltfreundlicheren Umgebung stark gestiegen. Wasserstoff ist aufgrund seiner Nachhaltigkeit und seines umweltbewussten Charakters weithin als effektiver, nachhaltiger und grüner Treibstoff der Zukunft anerkannt worden. Die photoelektrochemische (PEC) Wasserspaltung ist eine etablierte und leistungsfähige Technologie zur Umwandlung und Speicherung von Sonnenenergie in sauberes H_2 aus einer erneuerbaren Quelle.
Die im Rahmen dieser Dissertation durchgeführten Forschungsarbeiten zielten darauf ab, einen Beitrag zur Entwicklung effizienter oxidbasierter Halbleiter-Photoanoden für die Wasseroxidationsreaktion zu leisten, die den kinetischen Engpass der gesamten PEC-Wasserspaltungsreaktion darstellt. Die Untersuchung richtete sich insbesondere auf WO_3-basierte ternäre Metalloxide, $CuWO_4/WO_3$-Heteroübergangs-Photoanoden, die sich durch eine relativ schmale Bandlücke, die eine effiziente Nutzung des sichtbaren Lichts ermöglicht, eine außergewöhnliche chemische Stabilität bei neutralem pH-Wert und eine hoch oxidative Valenzbandkante auszeichnen. Für die Synthese der $CuWO_4/WO_3$-Filme wurde die einstufige hydrothermale Methode als kostengünstige und einfache Synthesestrategie eingesetzt, mit der sich eine breite Palette von Morphologien erzeugen lässt, die von Nanodrähten bis hin zu Nanoblütenstrukturen reichen. Es wurden Anstrengungen unternommen, um die intrinsischen Eigenschaften der löwenzahnartigen $CuWO_4/WO_3$-Filme mit verschiedenen hydrothermalen Reaktionsparametern zu optimieren. Die morphologischen und photoelektrochemischen Bewertungen zeigen, dass die Parameter der hydrothermalen Synthese einen großen Einfluss auf die Morphologie und die photoelektrochemische Leistung der $CuWO_4/WO_3$-Filme haben und dass der optimale pustelartige $CuWO_4/WO_3$-Heteroübergang die Ladungstrennung in einer neutralen Lösung erleichtert.

Der zweite Teil der Arbeit befasste sich mit der Verbesserung der Effizienz von $CuWO_4/WO_3$ Dünnschichten durch die Verankerung von NiCo-Doppelhydroxid (NiCo-LDH) als Katalysatoren auf dem Substrat. Die Ergebnisse der elektrochemischen Untersuchungen für dekorierte $CuWO_4/WO_3$-Heteroübergänge mit LDHs als Co-Katalysatoren zeigen eine Verbesserung der Photonen-zu-Strom-Umwandlungseffizienz (IPCE), eine kathodische Verschiebung des Photostrom-Anfangspotentials und einen Anstieg der Photostromdichte auf 0.17 $mA \cdot cm^{-2}$ bei 1.23 V gegen eine reversible Wasserstoff-Elektrode (RHE), die doppelt so

groß ist wie die der ursprünglichen Photoanode bei einem neutralen pH-Wert. Die gesteigerte Leistung der modifizierten Photoanode kann auf die schnellere Diffusion von Reaktanten und Produkten und den effizienten protonengekoppelten Elektronentransferprozess aufgrund der Anwesenheit von LDHs zurückgeführt werden.

Keywords: water splitting, oxygen evolution reaction (OER), semiconductor, catalyst.

1 Introduction

Since the discovery of the photoelectric effect by French scientist Edmond Becquerel, scholars and experts alike have been captivated by the concept of transforming light into electric power or chemical fuels. A shared aspiration among them is to harness the abundant energy of sunlight and convert it into either the coveted and significant resource of electric power or the production of fuels [1, 2].

The deleterious environmental contamination arising from frequent oil spills and the alarming climatic ramifications of the greenhouse effect resulting from the combustion of fossil fuels have provoked an escalation of public concern. The research efforts in this domain are predominantly directed towards the exploration and establishment of cost-effective and environmentally secure sources of renewable energy. There exist numerous renewable resources, such as sunlight, tides, wind, and geothermal heat, which are relatively less hazardous and contaminant-free, and more sustainable compared to the environmentally harmful fossil fuels. Nevertheless, each renewable resource possesses its own distinct constraints, making it quite challenging to replace the presently utilized non-renewable resources. Electricity generated through the utilization of wind energy poses a challenge in terms of storage feasibility. The creation of hydropower from dams may result in detrimental impacts towards the environment and is also deemed costly. Geothermal resources offer an inexhaustible energy source that is permanent in nature, although the execution of its operation is considerably pricey [3, 4]. Among the spectrum of renewable energy sources available, solar energy reigns supreme as the most abundant, available, and consistent source of power. Fortuitously, the provision of energy from the sun to the earth is enormous, amounting to 32×10^{24} joules annually, approximately 10,000 times more than the current global population's consumption. Solar energy is frequently employed to produce electricity or heat without turbines owing to its renewable characteristic and economical expense. Therefore, it is essential to devise an energy origin that is storable, environmentally friendly, cost-effective, and renewable to satisfy the worldwide demand for energy [1, 5].

In this regard, hydrogen is considered a potential energy transporter that can store and convey the natural form (chemical) of renewable energy. When burned in oxygen, hydrogen is an emission-free fuel and an extremely promising renewable energy source utilized in vehicles,

spacecraft propulsion, aircraft, and electric devices. Hydrogen is ensnared in water, hydrocarbons, and other organic substances. Thus, producing hydrogen on a massive scale from solar energy is an appealing proposition [6].

One of the promising methodologies for extracting hydrogen is through the process of water splitting. This process involves the separation of water into its constituent gases, oxygen and hydrogen. Various techniques have been proposed for water splitting, including photoelectrochemical (PEC) [7], photocatalytic [8], radiolysis [6], photobiological [9], and thermal decomposition [10]. However, it should be noted that radiolysis produces nuclear waste as a by-product [6], whereas photobiological water splitting, which relies on an algae bioreactor, transitions from oxygen production (i.e., normal photosynthesis) to low hydrogen production rates [9]. Meanwhile, the major drawbacks associated with thermal decomposition include its low yield of hydrogen and high temperature requirement. Ultimately, the simplest, most efficient, and cost-effective methods for producing hydrogen can be found in photocatalytic and photoelectrochemical water splitting [6, 11].

1.1 Aim of this study

This thesis aimed at playing part in development of WO_3-based photoanodes in order to explore the most effective, and economical approach to hydrogen generation through the process of water oxidation reaction. Given the numerous reports on the enhancement of photoelectrochemical activity of WO_3-based photoanodes using a variety of methods and catalysts, this research is focused on the investigation of applying layered double hydroxide (LDH) catalyst onto the $CuWO_4/WO_3$ photoanodes in neutral solution for the first time.

This objective was achieved through:

- Synthesis of $CuWO_4/WO_3$ photoanode with hydrothermal reaction.
- Study the effect of different precursor ratios on the structure and photocatalytic activity of the $CuWO_4/WO_3$ photoanode.
- Study the effect of different hydrothermal reaction's parameters on morphology and the photocatalytic activity of the $CuWO_4/WO_3$ photoanode.
- Enhancing the photoelectrochemical performance of the $CuWO_4/WO_3$ photoanode by employing layered double hydroxide (LDH) catalyst.

- Physiochemical characterization of photoanodes, catalysts, composite modified photoanodes; scanning electron microscopy (SEM), X-ray diffraction analysis (XRD), X-ray photoelectron spectroscopy (XPS), Raman spectroscopy, infrared spectroscopy (IR), ultraviolet-visible diffuse reflectance spectroscopy (UV-DRS).
- Photoelectrochemical characterization of photoanodes, catalysts, composite modified photoanodes; chopped light voltammetry (CLV), linear sweep voltammetry (LSV), electrochemical impedance spectroscopy (EIS), incident photon to current efficiency (IPCE), absorbed photon to current efficiency (APCE), Mott-Schottky.

2 Principles and background

This chapter centers on providing a mechanistic portrayal of the photoelectrochemical (PEC) water splitting reaction, along with the fundamental principles of PEC. Subsequently, information pertaining to metal oxides for employment in PEC water splitting, different co-catalysts for metal oxides photoanodes, synthesis methods of thin film metal oxides, and the impact of size and morphology of metal oxides in PEC water splitting reactions is presented.

2.1 Photoelectrochemical water splitting

After the primitive contributions of Fujishima and Honda in 1972 [12], the photoelectrochemical water splitting reaction has been extensively investigated as a promising approach for hydrogen production. Specifically, in the context of PEC water splitting, a photocatalyst material is subjected to *hv* irradiation of energy that is higher or equal to its bandgap. As a result, the photocatalyst semiconductor absorbs the light energy, leading to charge separation at the interface of the valence and conduction bands. This process generates holes and photo-excited electrons in the valence band and conduction band, respectively. At the surface of the VB, the produced holes act as inhibitors of the oxidation of water, while photoinitiated electrons at the conduction band serve to inhibit the conversion of H^+ ions to H_2 gas. In the majority of cases, semiconductor materials are employed as photocathodes or photoanodes in PEC water splitting, contingent upon the type of photocatalytic reaction under consideration. PEC water splitting may be accomplished through a two-step process referred to as the Z-scheme, which mimics natural photosynthesis. This system employs two distinct semiconductors for photoexcitation and a reversible shuttle redox mediator (donor/acceptor pair). A simple schematic depiction of the Z-scheme is presented in Figure 1. Upon the transfer of electrons between the semiconductor and the electrolyte solution, the Fermi level is equilibrated with the redox potential of the electrolyte solution. An electrolyte solution accepts (donates) electrons from (to) a semiconductor when the Fermi level of the semiconductor is more negative (positive) than the reduction potential of the electrolyte solution. Since the density of electrons in a semiconductor is finite and the potentials of the band positions at the interfaces can be assumed to be pinned, the transfer of electrons causes band bending. In the context of n-type semiconductor electrodes serving as photoanodes, the photoexcited holes are

known to accumulate on the semiconductor surface and subsequently undergo oxidation reactions. Conversely, electrons are transferred to a counter electrode through the back contact and external circuitry, where they are utilized in reduction reactions. This phenomenon is illustrated in Figure 1a. For a photoanode to generate oxygen, the top of the valence band must exhibit a more positive potential than the oxygen evolution potential. In contrast, a p-type semiconductor serves as a photocathode for hydrogen evolution when the conduction band edge is more negative than the hydrogen evolution potential, as depicted in Figure 1b. Notably, under photoexcitation, the potential of electrons on the counter electrode is equivalent to the Fermi level of the photoelectrode. Alternatively, the utilization of a photoanode and a photocathode may be connected in a tandem configuration, such as in Z-scheme water splitting (refer to Figure 1c), as opposed to the use of a solitary photoelectrode and counter electrode. This allows for simultaneous oxidation and reduction, resulting in a more efficient utilization of light energy [13].

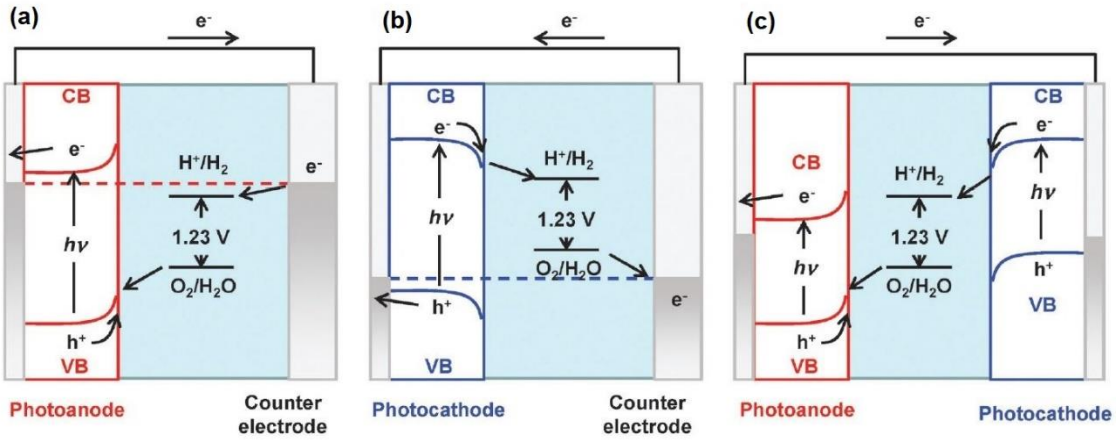

Figure 1. Illustration of PEC water splitting using (a) a photoanode, (b) photocathode, and (c) photoanode and photocathode in tandem configuration, adapted from [13].

2.2 Basic principle

The PEC water splitting reaction is composed of five distinct and sequential stages, as illustrated in Figure 2. These steps include a) the interaction between light and matter, b) the generation of electron-hole pairs, c) the separation and transportation of charges, d) the catalytic transfer of charges to the electrolyte, and finally, e) the water splitting reaction itself. Upon successful completion of this process, f) current flow between the two electrodes is obtained [11].

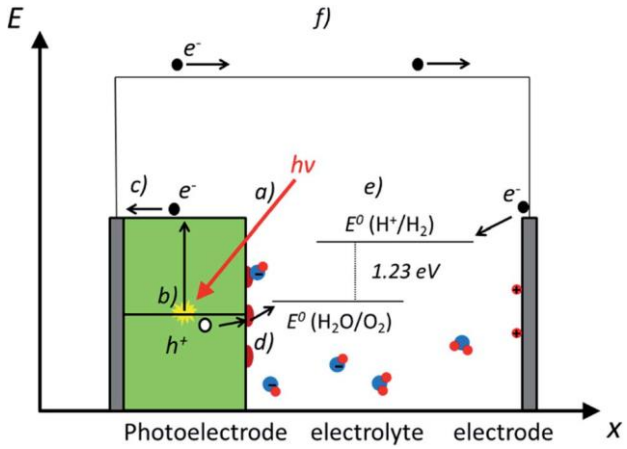

Figure 2. Scheme illustrating the principle of operation of a photoelectrochemical cell based on n-type semiconductor, adapted from [11].

Hence, the photoelectrolysis of water can be summarized as follows:

$$Semiconductor \xrightarrow{h\upsilon} e^-_{vb} + h^+_{cb} \quad (1)$$

$$e^- + H^+ \rightarrow \frac{1}{2} H_2 \qquad E^0_{H^+/H_2} = 0\ V\ vs.\ RHE \quad (2)$$

$$2h^+ + H_2O \rightarrow \frac{1}{2} O_2 + 2H^+ \qquad E^0_{O_2/H_2O} = 1.23\,V \quad vs.\ RHE \quad (3)$$

$$H_2O \rightarrow H_2 + \frac{1}{2} O_2 \qquad \Delta E = 1.23\ V \quad vs.\ REH \quad (4)$$

where h is the Planck's constant, υ is the frequency of light, e^- is photogenerated-electrons, and h^+ is photogenerated-holes.

The water splitting reaction involves two half-cell reactions: the cathodic hydrogen evolution reaction (HER) and the anodic oxygen evolution reaction (OER). The overall reaction (4) is endoenergetic, with a Gibbs free energy Δ_rG^0 = 237.2 kJ·mol^{-1} per mole of H_2 produced (according to the Nernst equation, ΔE = 1.23 V). Therefore, it is imperative that the semiconductor material utilized as a photoelectrode possesses the ability to assimilate light with a photon energy surpassing 1.23 [14-16]. In addition, the process of water splitting takes place at a significant cell potential range of 1.8-2.0 V in commercial electrolysers. This value is approximately 0.55 to 0.77 V higher than the theoretical value of 1.23 V. This additional

potential is necessary to overcome the energy barrier of the reaction system and is commonly known as overpotential. Overpotential can be attributed to various factors such as the resistance caused by the electrode, electrolyte, their separation distance, the circuit, and the hindrance in the activation steps of both the cathode and anode. Therefore, in order to practically execute the water splitting process, a potential higher than the thermodynamic potential is required [17].

Upon comparing Equation (2) with (3), it becomes evident that the half reaction of water oxidation is both thermodynamically and kinetically demanding. The energy barrier associated with this process is notably higher and the overall process exhibits a greater degree of complexity in comparison to water reduction. Notably, the production of a single mole of oxygen necessitates the involvement of four holes, while the generation of one mole of hydrogen only requires the participation of two electrons. Thus, the water oxidation half reaction represents one of the most challenging steps in PEC water splitting and has garnered significant attention over the years [18].

2.3 Metal Oxides for PEC Water Splitting

The photoanode material is the dominant factor determining the photo-to-chemical energy conversion efficiency of PEC OER. Several semiconductors have been invistigated as photoelectrodes for solar water splitting, and oxide-based photoelectrodes, in particular, are appealing due to their economical processing expenses and superior aqueous media stability in comparison to alternative types of semiconductor electrodes [19].

In accordance with fundamental principles, semiconductors of the n-type, possessing a valence band edge potential that is comparatively more positive than the potential of the O_2/H_2O redox couple (1.23 V vs standard hydrogen electrode (SHE)), have the potential to serve as photoanodes for OER [20]. Early studies on oxide-based photoelectrodes focused on development of binary oxides mainly including TiO_2 [21], Fe_2O_3 [22], ZnO [23], and WO_3 [24, 25] .Nevertheless, these compounds inherently suffer from some limitations. For instance, the large optical band gap (> 3 eV) of TiO_2 severely limits its absorption of the solar spectrum. Fe_2O_3 has low absorption coefficient, poor conductivity (~10^{-2} cm^2 V^{-1} s^{-1} at 20 °C), and short hole diffusion length (2–4 nm). ZnO has a large bandgap of 3.2 eV (active only in UV region of spectrum) and a high recombination rate of electron–hole pairs [25, 26].

In the meantime, WO_3 has been attracted a lot of interest due to its nontoxic composition, high hole mobility property (~10 cm^2 V^{-1} s^{-1}), high resistance against photo corrosion, and good

stability in acidic solutions. However, the comparatively large bandgap energy of WO_3 (2.7-2.8 eV) makes it active only in the near UV-blue visible region and narrow pH range for stable work (pH < 5), limiting its large-scale application [27, 28].

To overcome such drawbacks, one way is to create ternary and quaternary oxides, resulting by introducing some elements to binary oxides that could provides more opportunities to tune the composition and atomic and electronic structures of photoelectrodes, which can directly impact their photoelectrochemical properties. Based on this idea, several WO_3-based ternary oxides such as $CuWO_4$ [29], $ZnWO_4$ [30], and Bi_2WO_6 [31] have been synthesized and used as photoanodes for OER [20].

In the family of WO_3-based ternary oxides, $CuWO_4$ has the smallest bandgap energy of ca. 2.25-2.3 eV, therefore it can harvest a larger fraction of the visible spectrum (Figure 3) [32].

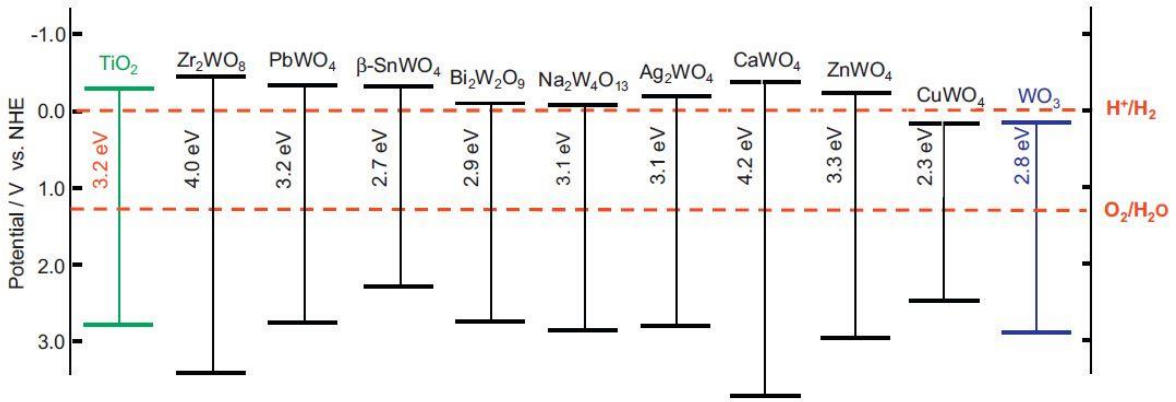

Figure 3. Comparison of the band positions of different W-based binary oxide semiconductors, adapted from [32].

$CuWO_4$ fits into a category of double oxides where each cation occupies a unique crystallographic site, and the d^9 configuration of Cu^{2+} leads to Cu(3d)−O(2p) hybridization. In fact, in $CuWO_4$, the late metal d-orbitals are sufficiently low in energy as to effectively hybridize with the O(2p) valence band. The VB is shifted upward, rationalized by mixing between Cu(3d) and O(2p) states [33, 34]. Concerning CB, the composition of $CuWO_4$ CB is extensively contested. Previous studies relying on first principal calculations revealed that the VB was mostly made up of O(2p) states with some Cu(3d) contributions. In addition, this model provided a CB dominated by W(5d) states [35, 36]. Furthermore, new experimental data suggests that the CB is displaced relative to that of WO_3, which the authors attribute to the incorporation of Cu(3d) states into the CB [37]. Although the specific contribution of Cu(3d)

states to the CB is unknown, the evidence supporting the contribution of Cu(3d) states to the VB is persuasive [34]. This hybridization results in a smaller band gap without adding mid gap impurity levels often associated with doping. Besides, this hybridization induces strong covalency in the metal–oxobonds and consequently reduces the formation of soluble tungstates [29]. $CuWO_4$ demonstrates enhanced chemical stability, light absorption, and selectivity for OER versus its binary oxide counterpart WO_3 (Figure 4) [33, 34].

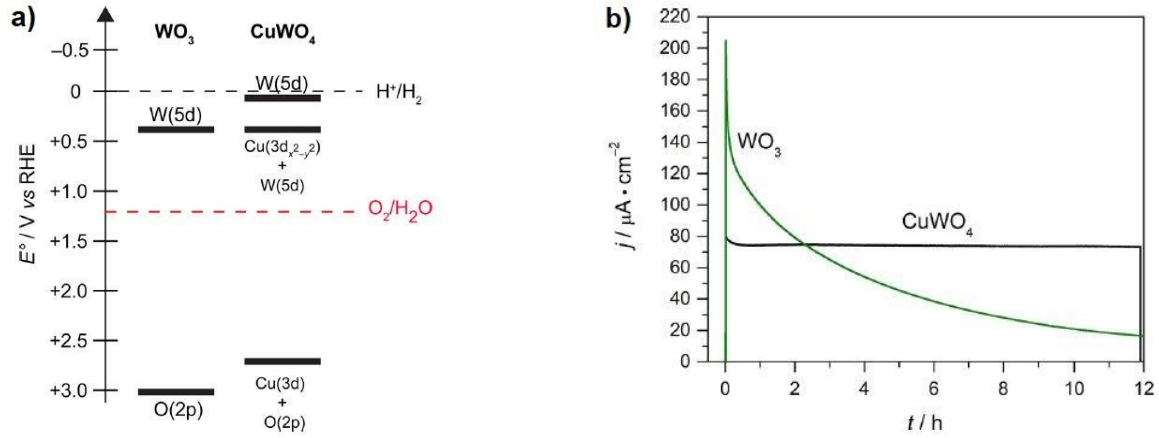

Figure 4. a) Electronic structures of $CuWO_4$ and WO_3. Band edge potentials are referenced to the reversible hydrogen electrode, RHE , b) Chronoamperometry j−t curve comparison in 0.1 M KB_i at pH 7 under AM1.5G illumination at 100 mW/cm^2 for WO_3 (green) and $CuWO_4$ (black), adapted from [33, 34].

Nevertheless, slow charge separation in the bulk of the electrode and slow surface water oxidation kinetics contributes to the poor overall efficiency for PEC water oxidation at $CuWO_4$ [38]. Accordingly, significant efforts have been focused to develop the PEC performance of $CuWO_4$, including fabrication of heterojunction through coupling with other semiconductors such as $BiVO_4$ [39], Mn_3O_4 [40], WO_3 [41], or carbon-based compounds such as multi-wall carbon nanotubes (MWCNT) [42], surface modification with plasmonic nanoparticles Au, Ag [43, 44], or with carbodiimides $(N=C=N)^{2-}$-based compounds like $Sn_2O(NCN)$[45], Ag_2NCN[46], nitrogen or hydrogen gas treatment to create oxygen vacancies [47, 48], and doping with metallic elements [20, 49]. Among these various approaches, loading oxygen-evolution cocatalysts (OECs) has been shown as an effective strategy to accelerate the surface reaction kinetics [50].

2.4 Cocatalyst

Cocatalyst is a distinct type of catalyst that lacks the property of optical absorption and cannot directly enhance light harvesting. Nevertheless, it exhibits high conductivity and effectively contributes to the improvement of PEC water oxidation by playing an indirect role. The cocatalyst may possess an amorphous structure with enriched reaction sites or a continuous layer with a certain level of crystallinity. The effective approach to enhance the performance of PEC water splitting is to couple the appropriate cocatalyst with a photoanode [51, 52].

2.4.1 Cocatalysts for Photoanodes

2.4.1.1 Metal Phosphates/Phosphides

Metal phosphates, particularly cobalt phosphates (Co-P_i), represent the pioneering cocatalyst candidates utilized in the PEC-OER process. These compounds are highly desirable due to their earth-abundant nature, amorphous structure, ion permeability, and ability to form on diverse surfaces comprised of varying semiconductor materials [51]. Notably, Sh. Chen and colleagues have demonstrated that the photocurrent of $CuWO_4$ electrodes catalyzed by cobalt phosphate complexes exhibits a 86% higher photocurrent response compared to unmodified $CuWO_4$ nanoparticles [53]. Additionally, X. Xiong and co-workers have reported a significant enhancement in both photocurrent and incident photon to current efficiency (IPCE) upon incorporating nickel phosphate (Ni-P_i) nanoparticles onto the surface of $CuWO_4$ photoanodes, thereby promoting the water splitting reaction [54].

2.4.1.2 Metal Oxides

Metallic oxides, such as IrO_x, RuO_x, NiO_x, CoO_x, and other hybrid compounds composed of metallic oxides, exhibit great potential as cocatalysts for water oxidation. This is primarily due to their facile preparation, exceptional stability, and activity in promoting the oxidation of water. The x index in the formula could differ according to the oxidation state of the metal oxide (transition metals). Among these metallic oxides, noble metal oxides, such as RuO_2 or IrO_2, are considered to be one of the most effective cocatalysts and display remarkable metallic electronic conductivity [55]. However, the employment of noble metal oxides as cocatalysts is

not without its flaws. One such drawback is observed in RuO_2, which displays a feeble resistance to corrosion in alkaline conditions, while IrO_x exhibits relatively poor conductivity. Moreover, the high cost of these precious metal-based cocatalysts is a significant impediment to their widespread implementation. Therefore, it is imperative to identify alternative cocatalysts that are highly active, possess good stability and are cost-effective. Earth-abundant transition-metal oxides are a promising option, owing to their low cost and exceptional resistance to chemical-corrosion or photocorrosion in specific electrolytes. Consequently, they are gradually gaining recognition as viable substitutes for noble metal-based cocatalysts [51]. And among these materials, cobalt- and nickel-based oxides are recognized as the promising PEC-OER cocatalysts. Liu et al. have successfully devised a highly proficient $Pt/CuWO_4/Co_3O_4$ photoanode system for the purpose of photoelectrochemical water splitting. The configuration entails the incorporation of p-type Co_3O_4 onto n-type $CuWO_4$, which not only establishes a p-n heterojunction but also serves as a co-catalyst to hasten the process of surface water oxidation. This novel ternary structure demonstrates an exceptionally amplified photocurrent that measures 4.4 mA/cm^2 at 1.23 V vs. RHE [38]. Zhang et al. engaged in the surface decoration of the photoanode consisting of $BiVO_4/WO_3$ through the incorporation of ultrafine CoO_x cocatalyst. The resultant composite photoanode ($CoO_x/BiVO_4/WO_3$) demonstrated a remarkable enhancement in its photoelectrochemical (PEC) water oxidation performance, as evidenced by a photocurrent density of 2.3 mA/cm^2 at 1.23 VRHE when subjected to simulated sunlight irradiation. This value was twice as high as that observed for the bare $BiVO_4/WO_3$ [56].

2.4.1.3 Metal (Oxy)hydroxides

Metal (oxy)hydroxides and their derivatives have been long established as catalysts for the PEC-OER process, owing to their low cost, abundance and ability to produce a substantial potential drop of Helmholtz layer at the photoanode/electrolyte junction [57-59]. A number of these materials have gained significant interest, particularly nickel-based, iron-based, cobalt-based (oxy)hydroxides, as well as layered double hydroxides (LDHs), as they exhibit superior performance. Fang et al. employed a photoelectrodeposition method to modify the $WO_3/BiVO_4$ film with NiOOH co-catalysts. The modification resulted in a quarter reduction in the interfacial carriers' transfer resistance of $WO_3/BiVO_4/NiOOH$ (148.2 Ω). The synergy between $WO_3/BiVO_4$ heterojunction and NiOOH cocatalyst was responsible for the charge separation

and injection efficiency of $WO_3/BiVO_4/NiOOH$ reaching 39.99% and 50.05%, respectively (7.04 and 6.11 times that of bare $BiVO_4$) [60].

In the study conducted by Zhao and colleagues, FeOOH catalysts were successfully produced through the implementation of a photoelectrodeposition technique onto a $CuWO_4/CdS$ photoanode. This led to a marked enhancement in the performance of the photoelectrochemical (PEC) system, with a substantial increase in photocurrent density reaching approximately 2.05 mA/cm^2 at a potential of 0.8 V versus RHE. Additionally, the system exhibited exceptional operational stability [61].

2.4.1.4 Layered double hydroxide (LDHs)

Layered double hydroxide (LDHs) nanosheets, which are part of the two-dimensional materials family, have garnered a significant amount of attention in the past few years, particularly since 2013, as potential transition metal-based OER catalysts [62]. LDHs possess numerous advantageous features, including a large surface-to-bulk ratio, a significantly more efficient exposure of catalytic active sites compared to 0D and 1D materials, controllable layered structure adjustment (intercalation, topological transformation, and assembly of other functional materials), tunable chemical composition with different cation ratios, hierarchical porosity facilitating the diffusion of water molecules and release of gaseous products [63]. Layered double hydroxides (LDHs) possess a crystal structure in which the transition metals are situated at the center of each octahedron, surrounded by oxygen anions on the eight corners, denoted as MO_6. As illustrated in Figure 5 the octahedrons conjoin by edge-sharing to form a two-dimensional layer structure. LDHs usually have a similar chemical formula $[M^{II}_{1-x} M^{III}_x (OH)_2]^{x+}(A^{n-})_{x/n} .mH_2O$, in which M^{II} and M^{III} are di- and trivalent metal cations, and A^{n-} are counter anions. Structure is consisting of a brucite like $M^{II}(OH)_2$ layer in which part of the M^{II} cations are isomorphously substituted by M^{III} cations, and the positively charged bulk layers are filled with anions in order to achieve charge balance. The value of x is equal to the molar ratio $M^{2+}/ (M^{2+} + M^{3+})$ and is generally in the range 0.2–0.33 [64, 65].

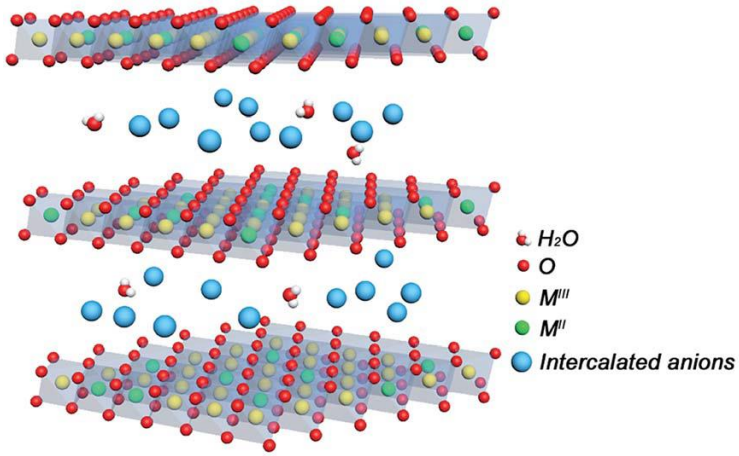

Figure 5. Schematic illustration of the crystalline configuration of LDH, adapted from [63].

The positively charged layers are constructed by divalent cations (e.g., Fe^{2+}, Ni^{2+}, Mg^{2+}, Ca^{2+}, Mn^{2+}, Co^{2+}, Cu^{2+}, and Zn^{2+}), or trivalent cations (e.g., Al^{3+}, Co^{3+}, Fe^{3+}, Cr^{3+}, Ga^{3+} and Ti^{3+}). The intercalated anions are commonly filled by CO_3^{2-}, which can be replaced easily by other anions (e.g., NO_3^-, SO_4^{2-}, ClO_4^-, Cl^- and Br^-) [66]. In all respect, this structure avails fast diffusion of reagents and products and efficient proton-coupled electron transfer process, making them become excellent catalyst candidates for PEC-OER. For instance, the authors Yue et al. have reported that the utilization of a super-hydrophilic H-CoAl-LDH/$BiVO_4$ photoanode resulted in a photocurrent of 3.5 mA/cm^2 at 1.23 V vs. RHE, which is a significant improvement of approximately 3.2 times when compared to a pure $BiVO_4$ photoanode [67]. Similarly, Bai et al. have demonstrated that the photocurrent density of the WO_3/Fe_2O_3 heterojunction, decorated by NiFe-LDH, reached a value of 3.0 mA/cm^2. This achievement is noteworthy as it represents a considerable increase in photocurrent density when compared to the values of WO_3 and α-Fe_2O_3, which were respectively 5- and 7-times lower [68].

2.5 Thin film synthesis approaches

A multitude of synthetic techniques have been devised for the fabrication of thin films. Broadly, they can be classified into four principal clusters contingent on the type of chemical reactions employed, namely, physical vapor deposition, chemical deposition, electrochemical deposition, and solution-based deposition approaches. The benefits and drawbacks of each method are presented in the Figure 6 [69].

2.5.1 Physical vapor deposition

The process of Physical Vapor Deposition (PVD) refers to methods of synthesis that utilize physical means to vaporize the target materials before depositing them onto the receiving substrates. A salient characteristic of PVD is the absence of chemical reactions. Techniques utilized in introducing the target materials comprise of plasma such as sputtering and molecular beam epitaxy, electron beam such as e-beam evaporation and molecular beam epitaxy, heat such as thermal evaporation and molecular beam epitaxy, and laser such as pulse laser deposition [69].

2.5.2 Chemical deposition

The disparity between chemical deposition and PVD is apparent, with the former involving chemical precursors and/or chemical reactions during the deposition. Chemical vapor deposition (CVD) or atomic layer deposition (ALD) are the preferred methods when the deposition is mainly performed via vapor-phase processes. Organometallic compounds, owing to their volatility, are predominantly utilized as the precursors to facilitate precursor delivery. Despite its advantages, the vapor phase technique is primarily limited by the high cost attributed to high-vacuum chamber assemblies, which introduce additional fabrication costs when compared with solution-based methods [69].

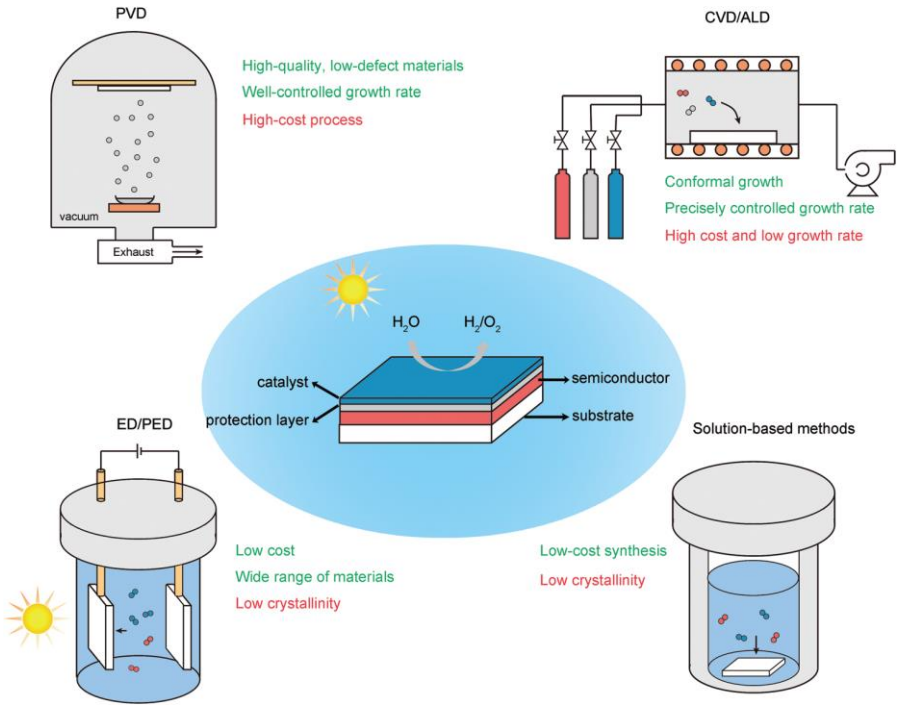

Figure 6. Schematics depicting the typical techniques employed in the deposition of thin-film materials, adapted from [69].

2.5.3 (Photo)electrochemical deposition

The distinctive nature of electrochemical deposition (ED) and photoelectrochemical deposition (PED) methods can be attributed to their utilization of an external bias and, at times, illumination. On one hand, this approach introduces additional parameters, including potential and current, to fine-tune the composition, morphology, and performance of the deposited materials. On the other hand, the application of light to aid in deposition during photoelectrochemical processes not only reduces the energy input required for synthesis, but also enhances the interface between the target materials (such as catalysts) and the receiving substrates, leading to improved charge transfer [69, 70].

2.5.4 Solution-based deposition methods

Solution-based growth methodologies confer numerous key benefits, encompassing cost-effectiveness, streamlined processing, and favorable scalability. An extensive array of morphologies, ranging from nanorods and nanowires to nanoflowers and nanotubes, characterized by diverse sizes and shapes, can be proficiently cultivated through solution-based

techniques. Hydrothermal/solvothermal methodology, which falls within this class of methodologies, is among the most widely employed approaches [71]. The solvothermal technique is nearly identical to the hydrothermal method, with the exception that a nonaqueous solvent is employed. Nevertheless, the temperature can be significantly increased compared to the hydrothermal approach due to the availability of diverse organic solvents with elevated boiling points [72].

2.5.4.1 Hydrothermal Method

Hydrothermal synthesis denotes a procedure that is conducted within a pressure vessel, wherein temperature and/or pressure are regulated, and aqueous or organic solutions are employed. In the case of the latter, the term "solvothermal" is preferred. Surfactant agents may also be included in some instances. The internal pressure and aspect ratio (i.e., diameter/length ratio) of the ultimate structure are significantly affected by the temperature, solution volume, and nature of the capping agent, such as F^- or SO_4^{2-} [72, 73]. The capping agents can adsorb onto the surface of growing nanoparticles, helping to control their growth and prevent agglomeration during the hydrothermal growth [74]. One noteworthy feature of hydrothermal methodologies is the ability to cultivate one-dimensional nanostructures, namely nanorods (NRs) and nanowires (NWs), which are attached to a conductive substrate (typically a fluorine-doped tin oxide (FTO) layer that is immersed within the reaction vessel). The resulting structures can be directly utilized as photoelectrodes. The FTO layers typically require positioning the F-SnO_2 side facing downwards towards the reactor's base to facilitate the growth of NRs/NWs on the conductive substrate [75]. Directly growing thin films from a substrate not only substantially improves the film's adherence and mechanical stability compared to standard deposition techniques, such as spin coating, dip coating, or doctor blading, but also provides better charge transfer and collection to the back-contact without resorting to additional binder layers that require tunnelling [76, 77]. In these circumstances, the formation mechanism relies on the continuous supply of H_2O molecules at the hydrophilic surface of FTO, i.e., the F-SnO_2 side, through the hydrolysis of the metal oxide precursor. Nuclei will appear throughout the substrate, and if their formation rate is controlled and restricted by the precipitation conditions, epitaxial crystal growth will occur from the nuclei. When the precursor concentration is high, a condensed phase of vertically aligned arrays perpendicular to the substrate will be created [77].

2.6 Size and morphology of MOXs in PEC water splitting

Moreover, the architecture and morphology of semiconductors hold considerable influence over the photoelectrochemical attributes of a photoelectrode. It is noteworthy that the characteristics of materials may differ significantly at the quantum, nano, and bulk scales. In comparison to bulk materials, nanomaterials (NMs) demonstrate exceptional size-dependent properties due to their elevated surface-to-volume ratio. Specifically, an enlarged specific surface area confers a significant advantage when a material is intended for catalytic applications: a greater number of active surface sites facilitates the adsorption of reactants, provides extended contact with solutions, and generally leads to enhanced reaction rates [14].

2.6.1 1D structures

In a vast range of applications, such as nanoelectronics, nanodevices, and energy-related fields, one-dimensional (1D) structures have been found to exhibit superior performances in terms of charge collection and transfer efficiencies [72, 75, 78]. The efficiency of charge collection is dependent on both the recombination lifetime of photogenerated charge carriers and their collection lifetime, which is the time required by e^- (h^+) to reach the semiconductor-electric contact (semiconductor/electrolyte interface) [79]. 1D nanostructures, including nanotubes (NTs), nanorods (NRs), and nanofibers (NFs), offer a preferential percolation pathway for charge carriers [75]. As demonstrated by Liu et al., the one-dimensional (1D) WO_3 nanorod can exhibit excellent PEC behaviors due to the direct electron transmission pathway provided by the 1D structure [80]. 1D nanostructure could significantly improve the charge collection efficiency, since the photogenerated electrons and holes will have to travel shorter distances to reach both end interfaces of the photoelectrode. Consequently, the recombination of photogenerated carriers could be limited, and the charge transfer efficiency could be increased [81].

2.6.2 2D structures

Two-dimensional nanostructures possess only one dimension at the nanoscale, such as nanoflakes, nanoplatelets, and thin films. This configuration concurrently provides (i) enhanced charge transport properties due to the directional transport of charges to the back-contact, (ii) facilitated access for electrolyte impregnation into the structure owing to the high

surface area, and (iii) a limited diffusion distance of photogenerated holes to the electrode/electrolyte interface, thus reducing the charge recombination rate [82, 83]. Ye et al. have successfully fabricated two-dimensional (2D) $CuWO_4$ nanoflake array photoanodes through the chemical conversion of a WO_3 template, resulting in a photocurrent density of 0.4 mA/cm^2, attributed to its substantial surface area and plentiful porosity [84].

2.6.3 3D Hierarchical structures

Hierarchical nanostructures (HNs) consist of a distinct backbone, typically arranged in one dimension, upon which nano-dimensional building blocks are grown. These building blocks typically include nanoparticles in zero dimensions, nanowires/rods/tubes in one dimension, and nanosheets in two dimensions. As a result, HNs often take on the appearance of nanotrees, which combine the properties of the one-dimensional backbone, such as enhanced carrier separation and directional charge transport, with a significantly increased surface area and a much higher number of active sites due to the highly porous arrangement provided by the branches [14, 85]. In comparison to one-dimensional and two-dimensional structures, the three-dimensional (3D) flowerlike structure displays unique properties, such as enhanced incident light utilization efficiency by increasing the times of reflection and shortened charge transport time and distance by special layered junctions [86, 87]. In Figure 7, the representation of SEM images exemplifies 1D, 2D, and 3D nanostructures.

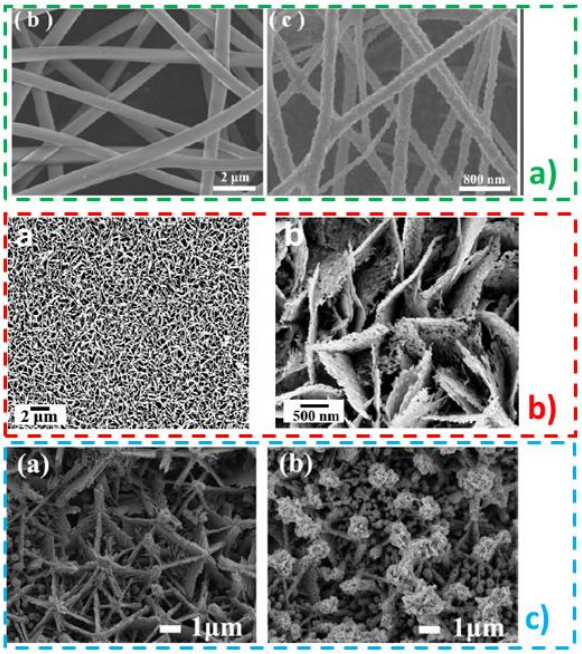

Figure 7. SEM images of a) WO_3 nanofiber, b) $CuWO_4$ nanoflake arrays, and c) flowerlike $CuWO_4$/CdS/FeOOH photoanode, adapted from [61, 81, 84]

3 Experimental methods and setups

This chapter provides an exposition of the research undertaken on the synthesis of $CuWO_4/WO_3$ thin films, NiCo-LDH co-catalyst, $CuWO_4/WO_3$/NiCo-LDH composite photoanode and their characterization methods.

3.1. Chemicals

The following chemicals were employed as supplied: ammonium metatungstate $[(NH_4)_6H_2W_{12}O_{40}]$ (Sigma-Aldrich), copper (II) chloride 99% anhydrate ($CuCl_2$) (Alfa Aesar), nickel (II) nitrate hexahydrate $[Ni(NO_3)_2 \cdot 6H_2O]$ (Alfa Aesar), cobalt (II) nitrate hexahydrate $[Co(NO_3)_2 \cdot 6H_2O]$ (Alfa Aesar), ammonium fluoride (NH_4F) (sigma aldrich), urea $[CO(NH_2)_2]$ (sigma aldrich), monosodium phosphate (NaH_2PO_4) (Alfa Aesar), disodium hydrogen phosphate (Na_2HPO_4) (Alfa Aesar), sodium hydroxide (NaOH) (Alfa Aesar), phosphoric acid (H_3PO_4) (Fisher Chemical), sodium sulfate (Na_2SO_4) (Fisher Chemical), Sodium sulfite (Na_2SO_3) (Fisher Chemical), Nafion (10%ethanolic,Sigma), EtOH (Fisher Chemical). Double distilled water was used for the preparation of all solutions. Fluorine-doped tin oxide (FTO)-coated glass sheets (2.2 mm thickness, 15 Ω) were purchased from Pilkington Glass and used as a substrate in preparation process.

3.2 Preparation of $CuWO_4/WO_3$ thin films

Herein, $CuWO_4/WO_3$ photoanodes were prepared by simple, one-pot hydrothermal method. The initial solution was prepared by mixing 2 mM of two precursors, equal ratio of (Cu:W)(1:1), ammonium metatungstate $(NH_4)_6H_2W_{12}O_{40}$ and copper chloride dihydrate $CuCl_2 \cdot 2H_2O$ in deionized water and stirring for 1 h. Subsequently, the resultant solution was transferred into a 20 mL Teflon-lined stainless-steel autoclave with the clean conductive fluorine-doped tin oxide (FTO) glass substrates immersed into the solution. The reaction was carried out at 180 °C for 8 h. Afterwards, the autoclave was cooled to room temperature naturally. The obtained films were subsequently annealed in furnace at 500 °C for 2 h. The films were heated and cooled at a rate of approximately 2 °C/min. After annealing, the resulting

bright yellow films were used in all subsequent experiments. The impact of varying ratios of Cu^{2+} and W^{6+} precursors was investigated. The hydrothermal synthesis process with two alternative ratios of Cu and W precursors, namely (Cu:W)(2:1), and (1:2) was studied. Figure 8 illustrates the synthesis process of $CuWO_4/WO_3$ thin film.

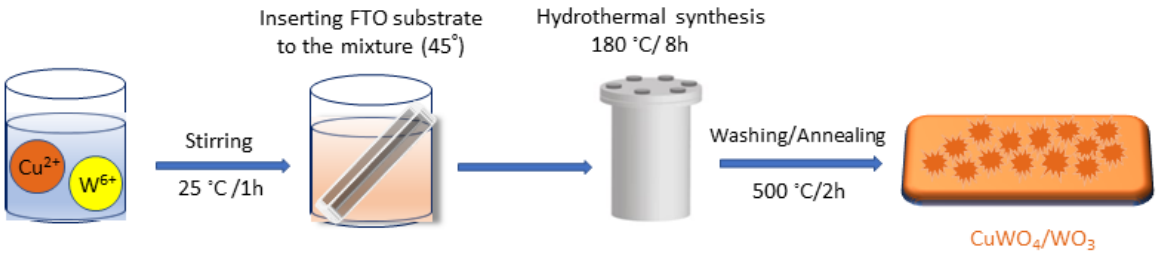

Figure 8. Schematic illustration of synthesis of $CuWO_4/WO_3$ thin film.

3.3 Preparation of NiCo-LDH co-catalyst

NiCo-LDH were synthesised through hydrothermal reaction as well. 0.5 mmol of $Ni(NO_3)_2 \cdot 6H_2O$, 1 mmol of $Co(NO_3)_2 \cdot 6H_2O$, 3 mmol of NH_4F, 7.5 mmol of urea were dissolved in 30 mL of deionized water. After stirring for 30 min, the obtained light pink-colored solution was poured into a 70 mL Teflon-lined stainless-steel autoclave, was kept at 120 °C for 10 h. After cooling to room temperature, the pink NiCo-LDH powder was washed with ethanol and deionized water three times, respectively. (Figure 9).

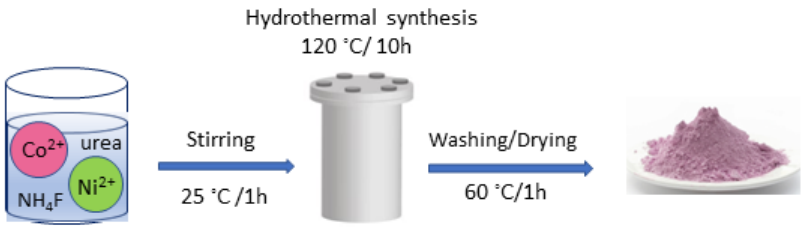

Figure 9. Schematic illustration of synthesis of NiCo-LDH

3.4 Preparation of $CuWO_4/WO_3$/NiCo-LDH photoanode

For loading the co-catalyst (NiCo-LDH) onto a $CuWO_4/WO_3$ photoanodes, the simple drop casting method was used. To begin with, a quantity of 2 mg of NiCo-LDH nanoparticles was dispersed in a solution of nafion measuring 2 mL. The resultant mixture was then subjected to sonication for a duration of 30 minutes, aimed at achieving a uniform nanoparticle "ink". The area of the drop-casted region was carefully regulated to 2 cm^2, while the mass of NiCo-LDH was controlled by the volume of ink used. Finally, the composites were thoroughly dried at 25 ºC (Figure 10).

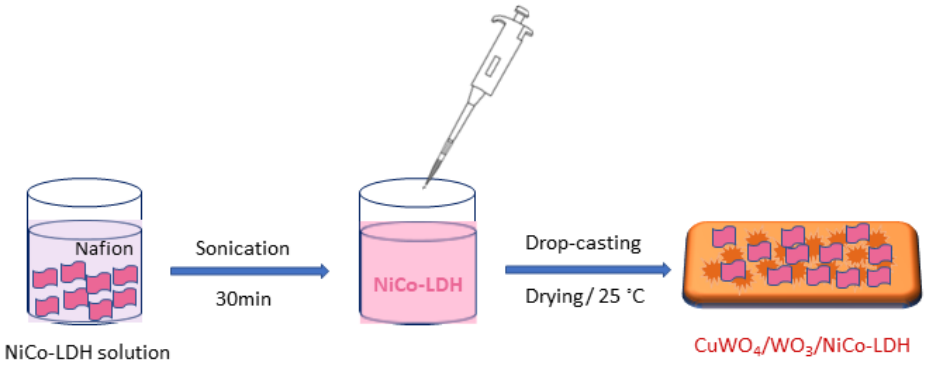

Figure 10. Schematic illustration of preparation of $CuWO_4/WO_{3\ 4}$/NiCo-LDH photoanode.

3.5 Characterization

3.5.1 Physicochemical characterization methods

3.5.1.1 Scanning electron microscopy (SEM)

Electron microscopy is a widely employed technique in the fields of solid-state physics and chemistry for the purpose of examining the surface topography of samples. Generally, electron microscopes use magnetic lenses to focus a beam of electrons onto a sample, thereby producing an enlarged image. Since electrons possess a much shorter wavelength than visible light photons, electron microscopes can achieve extremely high resolution. The interaction between the incident electron beam, with an energy ranging from approximately 1 to 40 keV, and the sample can occur in a variety of ways, as depicted in Figure 11a. The diverse kinds of interaction between the incident electron beam and the sample may be utilized for subsequent analysis of the material. The interaction of electrons with the sample can occur quasi-elastically

or inelastically. This interaction leads to the emission of Auger electrons from the upper 2 nm of the surface, secondary electrons (with energy less than 50 eV) from a depth of up to 5 nm, and backscattered electrons (with energy greater than 50 eV) from a depth of up to 100 nm. Signals from secondary electrons (from the surface) and backscattered electrons (from the bulk) are commonly used for imaging samples. Secondary electrons show the morphology and topography while back scattered electrons illustrate contrasts in composition in multiphase samples.

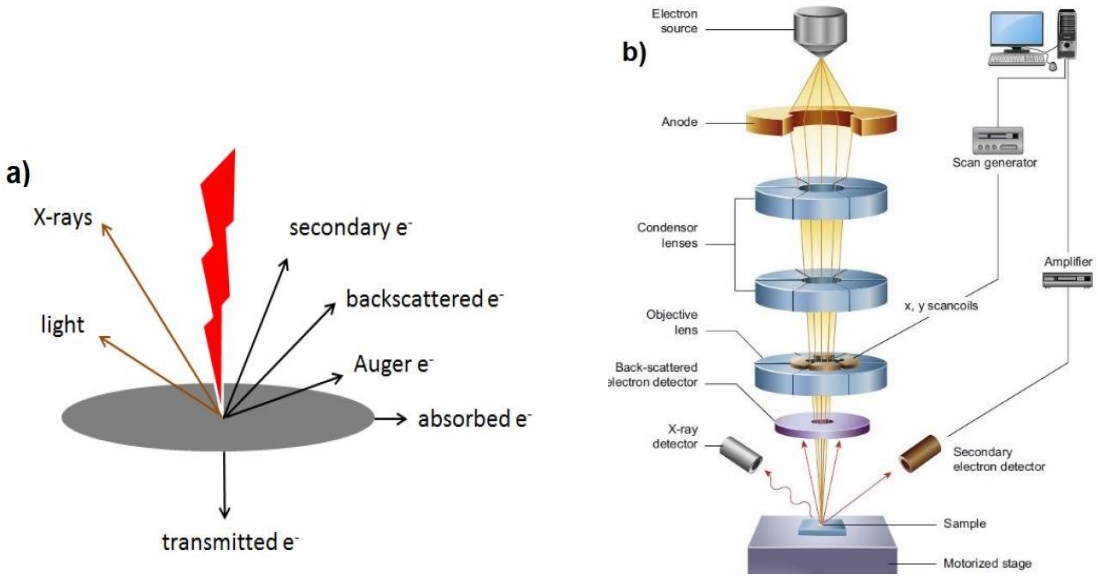

Figure 11. a) The interaction between a high-energy electron beam and a thin specimen produces various signals, b) schematic diagram of core components of a scanning electron microscope, adapted from [88, 89]

This signal is proportional to the average atomic number in the interaction volume. Henceforth, in BSE mode, the contrast of the image fluctuates as a function of the atomic number. This enables the differentiation between the boundaries of various elements and provides crucial knowledge concerning the surface structures of the sample. A typical microscope for SEM, as illustrated in Figure 11b, comprises of the electron gun, specifically the electron source and accelerating anode, which could be of either thermos ionic or field emission type. It also has electromagnetic lenses that focus the electron beam onto the specimen, a vacuum chamber that shelters the specimen stage, and a range of detectors that accumulate the signals released from the specimen. The application of ultra-high vacuum conditions (10^{-7}-10^{-8} Pa) is mandatory to circumvent any form of collision between the electron beam and air molecule [88-90].

Experimental methods and set-ups:

The morphology of the samples was determined by scanning electron microscopy (SEM) measurements, carried out by FEI Helios NanoLab 600i under vacuum atmosphere in the electron microscopy service of physics faculty at University of Oldenburg. Thin film samples were sprinkled lightly on a carbon tape fixed on an aluminum stub.

3.5.1.2 Energy Dispersive X-ray Spectroscopy (EDX)

Energy dispersive X-ray (EDX) spectroscopy is a frequently employed method for assessing the composition of a sample within an electron microscope. EDX method can afford high degree of relative precision, typically in the range of 2-4 %. The atoms of the matter under investigation are subjected to an incident electron beam, resulting in the ejection of inner shell electrons. These vacancies are subsequently filled by electrons from outer shells, and the associated energy is released in the form of X-rays and Bremsstrahlung (Figure 12). Various labels (e.g. K_1, K_2, L_1) are utilized to characterize the feasible electron transfers, and the energy discrepancies are unique to each atom. As a result, the elemental composition of a particular spot or area can be deduced from the acquired X-ray spectrum. The emission of X-rays is contingent on the atomic number of each atom (with heavier elements demonstrating greater efficiency), thus hindering the detection of lighter elements like hydrogen, helium, or lithium [91].

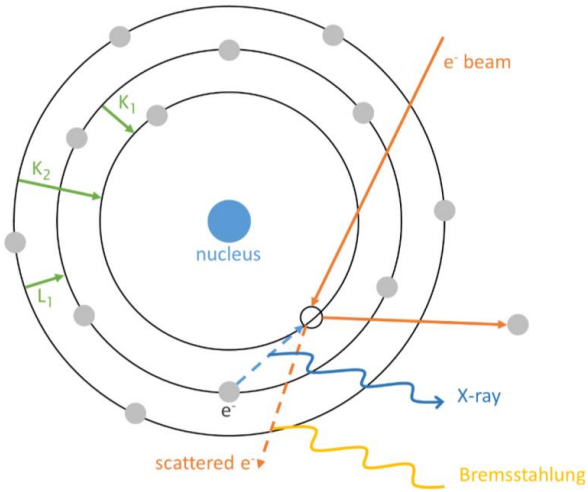

Figure 12. Schematic illustration of element-characteristic X-rays and Bremsstrahlung from the interaction of the electron beam with the sample, adapted from [91].

Experimental methods and set-ups:

The elemental dispersion of the specimens was determined through the utilization of energy-dispersive X-ray spectroscopy assessments, executed by the FEI Helios NanoLab 600i machine in a vacuum ambiance in the electron microscopy service of physics faculty at University of Oldenburg. All thin film samples were placed on a carbon tape affixed to an aluminum support for the measurements.

3.5.1.3 X-ray photoelectron spectroscopy (XPS)

X-ray photoelectron spectroscopy (XPS) is a quantitative technique utilized for surface spectroscopy that provides information about the elementary composition, oxidation states, and chemical environment of the elements that exist within a material. Surface analysis by XPS is accomplished by irradiating a sample with monoenergetic X-rays and analyzing the energy of the detected electrons. Typically, XPS uses either monochromatic Al Ka (1486.6 eV) or non-monochromatic Mg Ka (1253.6 eV) sources. These photons have limited penetrating power in a solid on the order of 1-10 micrometers. They interact with atoms in the surface region, causing electrons to be emitted by the photoelectric effect [92]. As illustrated in Figure 13b, the sample is placed in an ultrahigh vacuum (UHV) chamber and subjected to monochromatic X-ray irradiation, leading to the absorption of a photon (E= hν) by an electron. The photoelectron is subsequently emitted from the atom with a specific kinetic energy (E_{kin}), which can be ascertained by a hemisphere-shaped electron analyzer and a detector. The measured E_{kin} can be used to calculate the binding energy (E_b) of a photoelectron by the simple equation:

$$E_b = h\nu - E_{kin} - \phi$$

Where $h\nu$ is a photon (X-ray) energy, and ϕ is the detector work function.

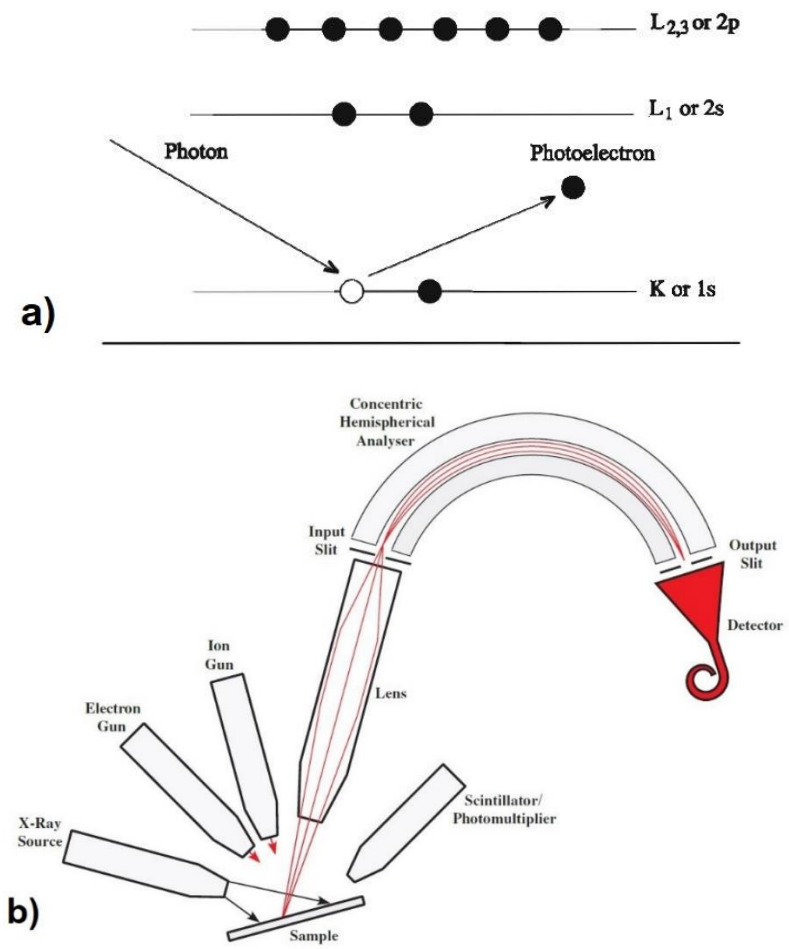

Figure 13. a) Schematic representation of the X-ray photoelectron process, b) and XPS spectroscopy setup, adapted from [92, 93].

In a typical X-ray photoelectron (XP) spectrum, the electron counts are reported as a function of their binding energy. The peaks observed at specific binding energy values are characteristic of the atomic composition of the analyzed sample and enable the identification of the elements present. Additionally, the relative shift in peak position, referred to as chemical shift, provides information about the local chemical environment such as the formal oxidation state of the atom and its chemical bonding state within the specimen. Furthermore, quantitative analysis can be conducted by integrating the XPS signals to estimate the relative abundance of several elements, which in turn permits the determination of the empirical chemical formula of the sample [94]. An accuracy of 10% is typically quoted for routinely performed XPS atomic concentrations.

Experimental methods and set-ups:

The surface composition and chemical state of the materials was examined by X-ray photoelectron spectroscopy (XPS) measurements with a Thermo Fischer ESCALAB 250 Xi photoelectron spectrometer with a monochromic Al Kα X-ray source (1486.6 eV) in XPS laboratory of Prof. Wittstock at University of Oldenburg. All peaks were calibrated using adventitious C1s peak of 284.8 eV to correct charge shift of binding energies after deconvolution. Powder sample was pressed to form a thin wafer while the film samples were fixed on the sample holder using a carbon tape.

3.5.1.4 FTIR and UV-Vis diffuse reflectance spectroscopy

Fourier transform infrared (FT-IR) spectroscopy is a technique used to acquire the infrared absorption spectrum of a solid, liquid, or gas. A wide spectral range is simultaneously collected by an FT-IR spectrometer in the typical range of 400-4000 cm^{-1}. The Fourier transform infrared spectras (FT-IR) of samples were recorded in the laboratory of Prof. Beckhaus at University of Oldenburg, operated in reflection geometry using a Bruker FT-IR Tensor 27 Spectrometer with a platinum ATR unit at room temperature.

UV-Vis absorption spectroscopy allows the monitoring of changes in light absorption due to electronic transitions within a material as a function of wavelength. UV-Visible spectrophotometers, commonly referred to as 'UV-Vis', examine the electromagnetic spectrum across the ultraviolet to visible range. Electron transitions frequently occur in molecules at these frequencies, especially in semiconductors with energy levels corresponding to allowed electron states [95]. As such, the determination of the magnitude and type of bandgap is possible. The most noted model describing diffuse reflection is from *Kubelka-Munk*, which displays a linear relationship between absorption and scattering [96]:

$$(R_\infty) = \frac{K}{S} = \frac{(1 - R_\infty)^2}{2R_\infty} \qquad (5)$$

with being the ratio of reflectivity of the sample to reflectivity of the white standard $\frac{R_{sample}}{R_{MgO}}$, absorption coefficient (K) and scattering of the probe (S). To calculate E_g, the empirical *Tauc*-Plot was introduced:

$$(F[R_\infty] * h\nu)^{\frac{1}{n}} \propto const.(h\nu - E_g) \quad (6)$$

where *hv* is the incident photon energy, *Eg* is the semiconductor optical band gap energy and *n* is a constant parameter denoting the nature of the band gap transition. Generally, for allowed transitions dominating the basic absorption processes, direct and indirect band gap transitions are described by n=1/2 or n=2, respectively.

Experimental methods and set-ups:

The diffuse reflectance spectra in the UV-Vis range were acquired utilizing a VARIAN Cary 4000 UV-Vis spectrophotometer, which was outfitted with an Ulbricht sphere. The white standard for this experiment was magnesium oxide (MgO), and the spectral range selected for analysis was between 200 nm and 800 nm at 1nm step resolution.

3.5.1.5 Raman spectroscopy

Raman spectroscopy is a scattering technique employed to observe lower energy transitions, specifically vibrational and rotational modes of the compound. Upon illumination of the sample with a monochromatic laser beam possessing an energy of $h\nu_0$, the sample molecules undergo excitation from either the ground state (E_0) or vibration state (E_1) to their corresponding virtual level ($E_0+h\nu_0$) or ($E_1+h\nu_0$). The scattering of the radiation occurs immediately after the sample molecules recover from the excited states. The scattering of the radiation can be comprehensively described by three distinct contributions. Firstly, there is the Rayleigh scattering (or elastic scattering), where the incident and scattered photons possess the same energy. Secondly, there is the Stokes Raman scattering, which is a form of inelastic scattering whereby the scattered photons possess lower energy than the incident photon. Lastly, there is the anti-Stokes Raman scattering, which consists of photons that are inelastically scattered with an energy greater than that of the incident photons. These phenomena correspond to the three different situations depicted in the afore mentioned description [97, 98].

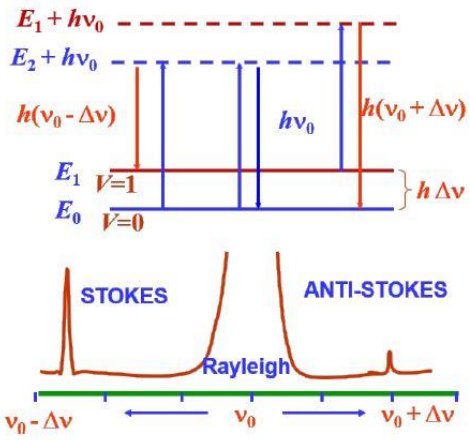

Figure 14. Principles of Raleigh and Raman (Stokes/Anti-stokes) scattering, adapted from [99].

During the process of inelastic Raman scattering, there is a quantized exchange in energy between the incident radiation and the sample. This exchange results in an energy shift between the incident and scattered photons, which is commonly known as Raman shift $\Delta\nu$. The Raman shift is defined as $\Delta\nu=\nu_0-\nu_1$, where ν_0 is the excitation wavenumber of the incident radiation and ν_1 is the wavenumber of the scattered photon that is monitored by the detector. As such, a Raman spectrum is typically presented as a function of Raman Shift (cm^{-1}) versus intensity. The vibrational bonds present in the sample can be identified by examining the different Raman shifts exhibited by each molecule's unique vibrational energy level [99].

Experimental methods and set-ups:
The Raman spectra were acquired at German Aerospace Center (DLR) in Oldenburg utilizing Bruker Senterra Raman spectrometer that operated within the range of 200 – 2000 cm^{-1}. The excitation line was provided by 488 nm laser with 0.2 mW laser power.

3.5.1.6 X-ray diffraction (XRD)

X-ray diffraction is a method employed by scientists to investigate the phase composition and crystal structure of materials. By utilizing monochromatic electromagnetic radiation with a wavelength of only a few angstroms, it has become one of the most significant techniques for structure determination. Diffracted X-rays experience constructive and destructive interferences when the wavelength of the incident radiation is similar to the distance (d) between the parallel crystallographic planes where atoms are arranged. This distance is

typically in the order of angstroms. Bragg's law describes the condition for observing constructive interferences between the diffused waves as:

$$n\lambda = 2dsin\theta \qquad (7)$$

the wavelength of the incident radiation is denoted by λ, while d represents the lattice plane distance. The angle of the incident beam on the crystallographic plane is indicated by θ, and n is an integer number that determines the order of the reflection (n = 1, 2, 3, …) [93, 100-102]. An X-ray directed with an angle θ onto a system with a lattice-plane distance d is depicted in Figure 15.

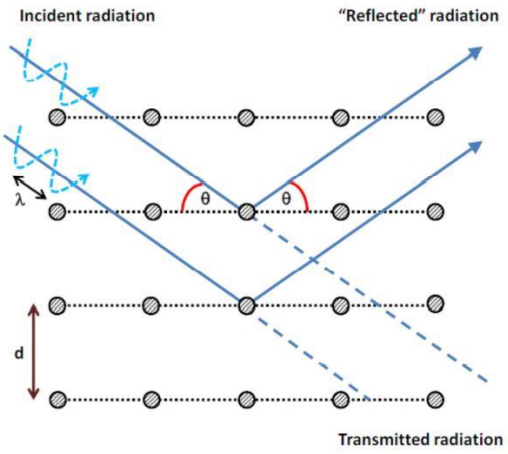

Figure 15. Schematic illustration of an X-ray scattering, adapted from [93].

Bragg-Brentano mode

The acquisition of X-ray diffraction patterns often involves the implementation of a measurement setup utilizing the Bragg-Brentano geometry. This mode, as illustrated in Figure 16, entails the synchronous scanning of both the X-ray beam source and the detector to maintain consistent incidence and diffracted angles during the scanning process. Detection of reflexes is restricted to those generated by crystallographic planes aligned parallel to the substrate.

Grazing Incidence XRD (GIXRD) mode

In Bragg-Brentano mode, the X-ray diffraction of thin films with a thickness in the range of tens of nm yields low intensity diffracted peaks and sensitivity to the layer structure. The limited path of the X-ray in the sample results in insufficient layer-to-substrate signal ratio at typical Bragg angles, and thus the X-ray patterns obtained are dominated by diffractions from the substrate due to the larger penetration depths of X-rays of the order of μm. To enhance the signal from the surface, various X-ray diffraction techniques have been developed, including the grazing incidence X-ray diffraction method (GIXRD). This technique utilizes very small, fixed incidence angles of the X-ray beam to limit penetration into the bulk material. In GIXRD mode, the incidence angle (ω in Figure 16b) is fixed, and the diffractograms are obtained by varying the detector position. This enables probing of crystals regardless of their orientation in the film [103].

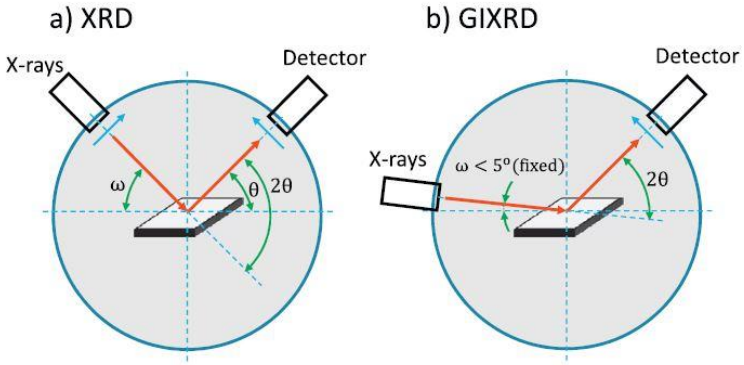

Figure 16. Scheme of: a) X-ray diffraction (XRD), b) grazing incidence X-ray diffraction (GIXRD) technique geometries, adapted from [104].

Experimental methods and set-ups:

Both powder and films X-ray diffraction patterns were obtained by BB and GIXRD modes by X-ray diffractograms (XRD) (PANalytical Netherlands, Empyrean Series 2) using Cu Kα radiation (λ = 0.154 nm). X-ray diffractograms were recorded over a range of 2θ of 5 - 80 at 40 kV and 40 mA.

3.5.2 Photoelectrochemical characterization methods

3.5.2.1 Photocurrent measurements

The evaluation of PEC photoelectrode performance is commonly conducted through the measurement of photocurrent density within a three-electrode configuration under 1 sun AM 1.5 G illumination (100 $mW \cdot cm^{-2}$). The fundamental experimental setup for PEC photocurrent measurements in a three-electrode configuration includes a PEC cell, a light source (a solar simulator or a xenon lamp with filters), and a potentiostat, as depicted in Figure 17.

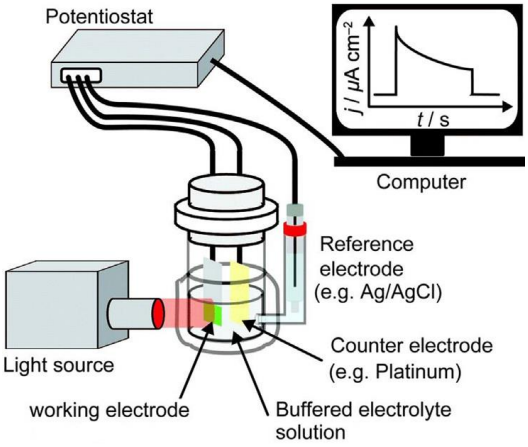

Figure 17. The experimental setup for PEC photocurrent measurement, adapted from [105].

The photoelectrochemical (PEC) cell is a reactor that comprises of a working electrode (WE), a counter electrode (CE), a reference electrode (RE), and an electrolyte for the oxygen evolution reaction (OER) and hydrogen evolution reaction (HER). The PEC cell is commonly designed as either an immersed-type glass cell or a compressed-type Teflon cell, each with distinct methods of mounting the WE [106, 107]. The compressed-type cell was implemented in our PEC cell design, wherein the WE is secured against an O-ring to establish contact with the electrolyte and has an exposed area of 0.785 cm^2 (Ø = 1.0 cm). Electrical connectivity to the working electrode was achieved by attaching a copper wire to the free edge of the fluorine-doped tin oxide (FTO) substrate using copper tape. A schematic of our PEC cell is presented in Figure 18.

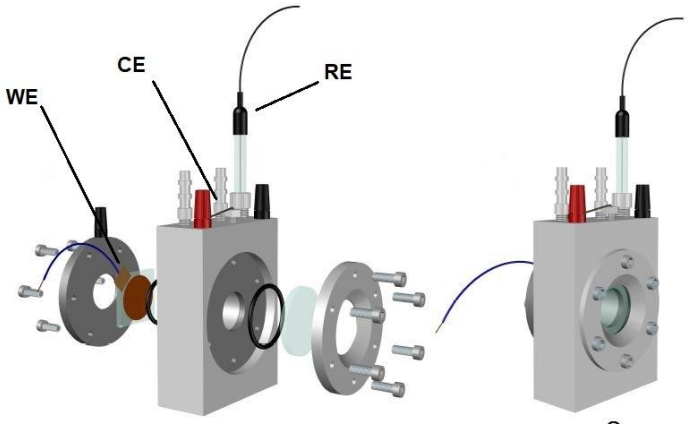

Figure 18. Custom-made PEC cell equipped with RE, WE and CE electrodes, adapted from [108].

The WE is the photoelectrode sample of interest (e.g., $CuWO_4/WO_3$ film), which is deposited on a conductive substrate as the back contact. The conductive substrate is typically composed of transparent conductive oxides (TCO), including fluorine-doped tin oxide (FTO) and indium tin oxide (ITO), which are highly affordable, corrosion-resistant, versatile, and exhibit excellent transparency [51]. The CE, on the other hand, serves as the reaction site for the other half-reaction of water splitting and should possess a large surface area and fast kinetics to avoid any limitations on circuit current. For the n-type photoanode and p-type photocathode, the commonly used CEs are Pt and RuO_2 (or IrO_2), respectively [107]. Finally, the RE in a three-electrode configuration ensures that the potential of the WE is applied and measured with respect to a well-defined electrochemical potential scale. Commonly used REs include saturated calomel electrodes (SCEs) and Ag/AgCl electrode [109]. The electrolyte utilized should be an aqueous solution that exhibits strong ionic conductivity and does not elicit a reaction with the photoelectrode. In instances where photoelectrodes necessitate an acidic electrolyte, it is common to employ 0.5–1 M solutions of H_2SO_4 [110]. For those photoelectrodes requiring an alkaline electrolyte, 0.5–1 M solutions of KOH or NaOH are frequently used [111, 112]. In cases where a neutral electrolyte is necessary, it is common to utilize 0.5m solutions of Na_2SO_4, K_2SO_4, or KH_2PO_4/K_2HPO_4 buffer [113]. It is important to note that electrolytes that undergo electrochemical reactions with WEs or CEs during PEC measurements should be avoided. In efforts to characterize photoelectrodes for use in water splitting, the potential is typically reported against the reversible hydrogen electrode (RHE). The utilization of the photovoltage, which is the discrepancy between the onset of photocurrent and the thermodynamic redox potential, can be easily calculated by displaying the

photoelectrode performance in relation to the thermodynamic water reduction potential at the specified pH. Additionally, comparing the efficiency of photoelectrodes that are operated in different pH conditions is made simpler by this method. Consequently, it is highly recommended that J-V plots and any other photoelectrochemical properties be reported against the RHE. The conversion of the potential measured against the Ag/AgCl RE to the potential against the RHE is shown in equation:

$$E_{RHE} = E_{Ag/AgCl(sat.KCl)} + 0.0591\ pH + E^{0}_{Ag/AgCl(sat.KCl)} \quad (8)$$

Current-voltage curves characteristic

To assess the response of photocurrent to applied potential, it is customary to employ the linear sweep voltammetry mode utilizing the potentiostat. This mode involves the linear sweeping of the potential of the working electrode (WE) with respect to the reference electrode (RE) at a constant scan rate ranging from 10-100 $mV \cdot s^{-1}$, while recording the current flowing between the WE and the counter electrode (CE). To obtain the photocurrent density value, the recorded photocurrent data must be normalized by the projected geometric surface area of the illuminated sample exposed to the electrolyte. Alternatively, the chronoamperometry mode of the potentiostat can be utilized to measure the photocurrent response at a fixed applied potential over time. In this mode, the potential applied to the WE is fixed, and the resulting photocurrent is monitored as a function of time. Plotting the photocurrent density at a fixed applied potential as a function of time will result in a J-t plot. The J-t plot is a commonly employed technique for the evaluation of the stability performance of the photoelectrode. It is generally accepted that a stable photoelectrode will exhibit a constant photocurrent density over a test duration of 1 to 24 hours, and even up to several days. Conversely, a reduction in the photocurrent density is often indicative of corrosion of the electrode in the electrolyte [114].

3.5.2.2 Incident Photon-to-Current Efficiency (IPCE)

The IPCE offers wavelength-specific external quantum yields (EQE) for a given photoelectrode. It characterizes the photocurrent that is gathered per unit of incident photon

flux as the electrons traverse an external circuit with respect to irradiation wavelength. The IPCE computes the efficiency in the form of "electrons out per photons in" while also factoring in the effects of spectral alterations in the incident photons [106]. The IPCE can be calculated using Equation (9) at a given bias voltage:

$$IPCE(\lambda) = \frac{electrons\ cm^{-2}\ s^{-1}}{incident\ photons\ cm^{-2}\ s^{-1}} \quad (9)$$

$$IPCE\ (\lambda) = \frac{J_{ph}(\lambda)/e}{P_{mono}(\lambda)(hc/\lambda)} = \frac{J_{ph}(\lambda) \times 1239.8}{P_{mono}(\lambda) \times \lambda} \quad (10)$$

where 1240 (V × nm) equals to h (Planck's constant, 6.63×10^{-34} J·s) multiplied by c (the speed of light, 3×10^{8} m·s^{-1}) and e (the charge of an electron, 1.6×10^{-19} J·eV^{-1}); J_{ph} is the measured photocurrent density (mA·cm^{-2}); λ represents the wavelength of incident light (nm); P_{mono} is the calibrated intensity of the incident light (mW·cm^{-2}) [115].

3.5.2.3 Absorbed Photon-to-Current Efficiency (APCE)

The metric of absolute photoluminescence quantum yield, commonly referred to as APCE, is equivalent to the measure of internal quantum efficiency (IQE). This parameter gauges the efficiency of a material based on the absorbed incident photons, thereby enabling a comprehensive understanding of its inherent properties. Specifically, APCE represents the percentage of absorbed photons used for the generation of photocurrent. The computation of APCE necessitates the acquisition of precise absorbance data via UV−vis spectrophotometry [107]. Using the absorbance data, a light harvesting efficiency (LHE) at each wavelength can be calculated using:

$$LHE = 1 - 10^{-A(\lambda)} \quad (11)$$

where A(λ) is the absorbance at a given wavelength. By dividing IPCE at each wavelength by the LHE at the corresponding wavelength, APCE can be calculated [116]:

$$APCE\% = \frac{IPCE}{LHE} \times 100 \quad (12)$$

3.5.2.4 Applied Bias Photon-to-Current Efficiency (ABPE)

The efficiency of water splitting in a PEC cell under bias conditions, when illuminated by broadband sunlight, is described by the ABPE. It serves as an indicator of the photoelectrodes' performance and the net current production resulting from electron extraction through the application of a suitable bias voltage. The following formula can be employed to calculate the ABPE:

$$ABPE\% = \frac{J_{PEC} \times (1.23 - V_{app})}{P_{light}} \times 100 \quad (13)$$

where J_{PEC} is the photocurrent density (mA/cm^2), V_{app} is the applied bias between the working electrode and counter electrode (V), and P_{light} is the incident illumination power density (AM 1.5G, 100 mW/cm^2). The ABPE is determined through the division of the output power density by the input power density of the device. The input power density, in turn, denotes the power density of incident light, which is precisely 100 mW/cm^2 for AM1.5G solar irradiation. The output power density for a water splitting PEC is given as the product of the photocurrent density (J_{PEC}) and the thermodynamic potential required for water splitting, 1.23 V. However, because an external bias is applied to facilitate water splitting, the amount of applied bias (V_{app}) between the WE and CE is subtracted from 1.23 V. It is important to note that the ABPE calculation requires J−V measurements using a two-electrode cell so that both the J_{PEC} and the V_{app} are measured between the WE and CE to represent accurately the device performance for overall water splitting [117].

3.5.2.5 Charge separation and charge injection efficiencies

The comparison of the J-V curves obtained under non-sacrificial circumstances and in the company of an appropriate hole scavenger is a customary technique to assess the effective photoinduced charge generation in photoelectrochemical procedures. Examining the

performance of the photoelectrode regarding efficiencies for three distinct processes, namely light absorption, charge separation, and interfacial charge injection, as illustrated in eq. 14, is beneficial.

$$J_{PEC} = J_{abs} \times \eta_{sep} \times \eta_{inj} \quad (14)$$

In this equation, J_{PEC} is the measured photocurrent density, J_{abs} is the photon absorption rate expressed as current density and can be calculated assuming 100 % APCE using the absorption spectrum of the photoelectrode. The parameter known as η_{sep} represents the efficiency of charge separation within the material's bulk. This is indicative of the proportion of photogenerated holes that can successfully traverse the bulk and reach the interface of the electrode/electrolyte without combining with electrons in the bulk. η_{inj} on the other hand, refers to the level of charge injection efficiency that occurs within the electrolyte. Specifically, this parameter indicates the fraction of holes that reach the surface and can transfer to the electrolyte to facilitate the oxidation of water. This transfer occurs without the interference of electrons located at surface trap states. The measurement of the charge-transport efficiency assumes that the oxidation kinetics of a hole scavenger, such as H_2O_2 or Na_2SO_3, is very fast and its charge-transfer efficiency is 100 %. Therefore, when J_{PEC} is measured with hole or electron acceptors with η_{inj} =1, η_{sep} can be easily calculated by measuring photocurrent density and the absorption spectrum of the photoelectrode (eq. 15):

$$\eta_{seperation} = \frac{J_{scavenger}}{J_{abs}} \quad (15)$$

The value of $J_{scavenger}$ can be measured by adding a hole scavenger (0.1–0.5 M) to the electrolyte for regular measurement of the photocurrent versus the applied potential under AM 1.5 G simulated solar light illumination. The value of J_{abs} is obtained from the measurement of light absorption and the integration of light absorption over the AM 1.5 G solar light spectrum:

$$J_{abs} = q \int_{\lambda_1}^{\lambda_2} N(\lambda)_{AM1.5}\, LHE\ (\lambda)\ d\lambda \quad (16)$$

$$LHE = 1 - 10^{-A(\lambda)} \quad (11)$$

$$J_{abs} = \frac{q}{hc} \int_{\lambda_1}^{\lambda_2} \phi(\lambda)_{AM1.5} \times \lambda \times \left(1 - 10^{A(\lambda)}\right) d\lambda \quad (17)$$

Here $N(\lambda)_{AM1.5}$ (unit of $m^{-2}s^{-1}$) is the photon flux density under standard conditions (AM 1.5G 100 $mW \cdot cm^{-2}$), $\Phi(\lambda)_{AM1.5}$ (unit of $Wm^{-2} \cdot nm^{-1}$) is the energy of photons from the solar simulator in unit area and unit time, E is the energy of one photon, λ (unit of nm) is the wavelength of photon, h (6.626×10^{-34} J·s) is Planck's constant, q (1.602×10^{-19} C) is the charge of one electron, LHE represents the light harvesting efficiency, $A(\lambda)$ is the measured absorbance of the photoelectrode [118].

The charge injection yield ($\eta_{injection}$), which is the yield of holes that have reached the electrode/electrolyte interface and that are injected into the electrolyte to oxidize the water, was calculated using equation:

$$\eta_{injection} = \frac{J_{PEC}}{J_{scavenger}} \quad (18)$$

3.5.2.6 Electrochemical impedance spectroscopy (EIS)

The electrical conductivity of the photoelectrochemical (PEC) system plays a crucial role in determining the efficiency of charge transfer within the electric circuit. Electrochemical impedance spectroscopy (EIS) is commonly employed to measure the conductivity of the PEC system, owing to its universal and powerful modulation techniques, which facilitate a comprehensive understanding of the complex reaction occurring at the photoelectrode surface. EIS experiments involve the application of a small amplitude sinusoidal signal to the photoanodes at a specific bias, while simultaneously measuring the system's response to the perturbation. During the EIS experiment, the current density of the electrode is recorded, while an alternating current signal with varying frequencies (usually between 0.1 Hz and 106 Hz) is

applied to the system [78]. By means of electrochemical impedance spectroscopy (EIS) characterization, it is possible to obtain a Nyquist plot illustrating the real versus imaginary impedance. On the spectrum, the X-axis corresponds to the real impedance (Z′), measured in Ohms, while the Y-axis represents the imaginary impedance (Z″), also in Ohms. In principle, a typical Nyquist plot can be divided into two distinct regions: the high frequency region and the low frequency region, as depicted in the Figure 19. The high frequency region is typically observed near the origin of the plot. In this region, the photo-electrochemical process is governed by the rate of charge transfer and the curve tends to exhibit the shape of a semicircle, which is indicative of the presence of an interface. In the low frequency region, where the impedance is large and far from the origin, the process is governed by the mass transfer rate. Regarding the spectrum, the charge-transfer resistance (R_{ct}) is directly proportional to the chord length of the arc. A larger chord length corresponds to a larger R_{ct}, which, in turn, denotes a poor charge-transfer ability or conductivity for water splitting [78, 119, 120]. The Nyquist plot could be fitted with equivalent electrical circuits as depicted in Figure 19. The electrical circuit is constructed for calculation and simulation of impedimetric data. The presented circuit model (Figure 19) is Randless cell circuit model, which includes solution resistance (R_s), charge transfer resistance of electrode (R_{ct}), Warburg impedance (W), and capacitance (C). This circuit model represents the electron transfer ability of the layer on electrode surface (R_{ct}), mass transfer (W) and electrode surface capacitance (C_{dl}) [121].

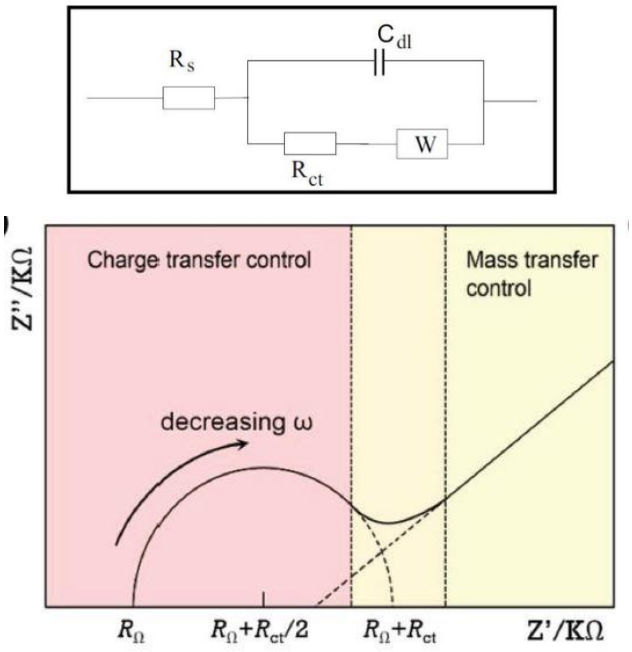

Figure 19. A typical Nyquist plot of a photoelectrode in the photo-electrochemical process, ω is the angular frequency, adapted from [122].

3.5.2.7 Mott–Schottky analysis

The determination of the flat-band potential (EFB) plays a fundamental role in regulating the photoelectrochemical characteristics of a photoelectrode. When considering the electronic configuration and conductivity of semiconductors, the Fermi level appears to be a critical position. Specifically, the Fermi level is defined as the energy level at which the occupation probability of an electron is ½. For instance, in the case of an intrinsic semiconductor, the Fermi level is situated at the midpoint of the band gap.

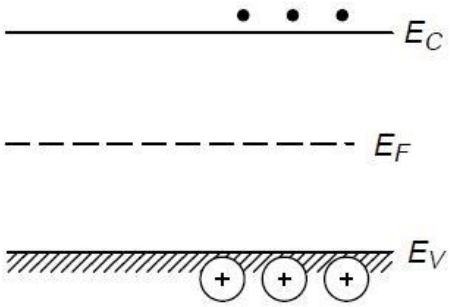

Figure 20. Schematic diagram of the energy levels of an intrinsic semiconductor, adapted from [123].

When a semiconductor electrode is brought into contact with an electrolyte solution, a potential difference is established due to the difference in electrochemical potential. The redox potential of the electrolyte solution determines the electrochemical potential of the solution, whereas the Fermi level determines the redox potential of the semiconductor. To equilibrate the two phases, a movement of charge between the semiconductor and the solution is required as there exists a potential difference between them. Upon equilibration, the excess charge located on the semiconductor extends into the electrode for a significant distance, typically ranging from 10-1000 nm, resulting in the formation of a space charge region. This region exhibits an associated electrical field that is of interest in semiconductor electrochemistry.

In the case of an n-type semiconductor electrode operating at open circuit, it is typical for the Fermi level to surpass the redox potential of the electrolyte. As a result, electrons tend to migrate from the electrode into the solution. This phenomenon results in a positive charge that is linked to the space charge region, also known as the depletion region. The upward bending of the band edges reflects this charge. Moreover, when the potential is negative with respect to

the flat band potential for an n-type semiconductor, there is an excess of majority charge carriers, namely electrons, in the space charge region. This region is referred to as the accumulation region. At a specific potential, the Fermi energy aligns with the solution redox potential. At this point, there is no net transfer of charge, and thus there is no band bending. This potential is known as the flat band potential, E_{fb} [123].

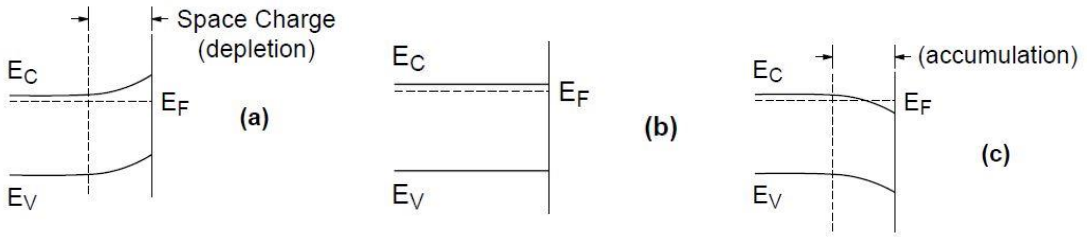

Figure 21. Effect of varying the applied potential (E) on the band edges in the interior of an n-type semiconductor. a) E > E_{fb}, b) E = E_{fb},c) E < E_{fb}, adapted from [123].

E_{FB} values can be measured using the Mott−Schottky equation which is based on measuring the apparent capacitance as a function of potential under depletion condition:

$$\frac{1}{{C_{sc}}^2} = \frac{2}{N_d \varepsilon_0 \varepsilon e}\left(E - E_{fb} - \frac{k_B T}{e}\right) \qquad (19)$$

where C_{sc} is the capacitance of the space charge region, N_d is the charge carrier density, e is the electron charge, ε represents the dielectric constant of electrode material, ε_0 is the permittivity of vacuum, E is the applied potential, E_{fb} stands for the flat band potential, k_B is the Boltzmann's constant, and T is the absolute temperature. The Mott-Schottky plot's linear region imparts three distinctive pieces of information. Firstly, the slope's sign enables the identification of the doping type; a positive slope indicates n-type materials, while a negative slope indicates p-type materials. Secondly, by extrapolating the linear region of the plot, the E_{fb} can be computed from the x-intercept, E_{fb}-(kT/e). Thirdly, the majority carrier density can be deduced from the slope's magnitude [107, 124].

Experimental methods and set-ups:

All photoelectrochemical measurements were performed using a ZAHNER ZENNIUM electrochemical workstation and a light source powered by a ZAHNER PP211 potentiostat (either a white light LED for IV and CLV measurements or a tunable light source plus monochromator for IPCE measurements). The experiments were controlled over a computer connected to the setup and running the THALES software package. The PEC cell had a configuration with the $CuWO_4/WO_3$ thin film as the working electrode, a Pt wire counter electrode, and an Ag/AgCl reference electrode. The actual geometric area of the working electrode with a A= 0.785 cm^2 geometric area was exposed to front-side illumination in the electrolyte (Na_2SO_4 0.1 M in phosphate buffer solution PBS, pH=7). For chopped light voltammetry (CLV) measurements a white LED light source (1200 $W \cdot m^{-2}$ incident photon flux) was used. The potential was scanned at a rate of 10 mV/s between 0 V and +1 V vs. Ag/AgCl with light on and off cycles each lasting for 10 s. For comparison purposes, the applied potentials versus Ag/AgCl (sat. KCl) were converted into potentials relative to the reversible hydrogen electrode (RHE) by using the Nernst equation (eq. 8). Electron impedance spectra (EIS) were recorded within the frequency range 10 mHz to 100 kHz with 10 mV amplitude of AC rms amplitude at 1.23 V vs. RHE under the illumination. Mott−Schottky measurements were carried out in the above three electrode cell within the potential range of 0.3–1.4 V vs. RHE in the dark at the frequency of 1000 Hz. Incident photon-to-current efficiency (IPCE) was measured with the same three-electrode setup described above for photocurrent measurements, using the smaller custom-made PEC cell and a Zahner TLS03 tunable light source coupled with a USB controlled monochromator. During the measurement, a potential of 1.23 vs. RHE was applied and the light intensity was set to 100 $mW \cdot cm^{-2}$. The simulated IPCE curves were obtained with the help of the THALES software package.

4 Results and discussion

This chapter expounds upon the outcomes derived from the fabricated photoanodes, catalysts, and composite structures and simultaneously analysis and discussion of the acquired data in correlation to prior literature.

4.1 Dandelion-like $CuWO_4/WO_3$ thin film

4.1.1 SEM results

The morphology of the thin films was analysed through the utilization of the scanning electron microscopy (SEM) approach. It is illustrated in Figure 22a, b, presenting both the top and lateral view images of the as-obtained sample. The top view indicates that the FTO substrate surface is enveloped with a planar film, in addition to the well-aligned dandelion-like structures that are situated on top of it. The dandelion structures possess a diameter of approximately 5 µm. Additionally, the cross-sectional view reveals that the average thickness of the film is approximately 0.8 µm, thereby affirming the film's formation on the surface of the substrate (Figure 22c).

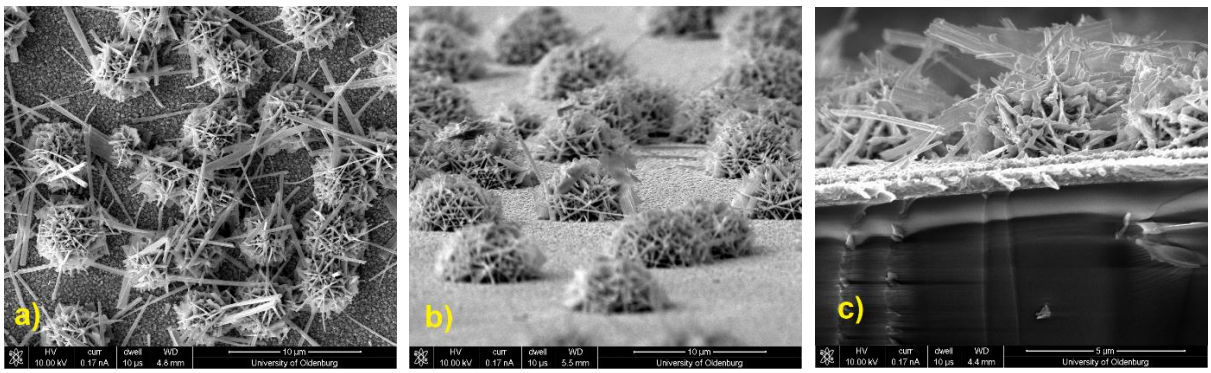

Figure 22. a) Top view b) lateral view c) cross-sectional view SEM images of dandelion-like $CuWO_4$ thin film.

4.1.1.1 Mechanism reaction

Herein, the formation mechanism of flowerlike $CuWO_4$ is analysed. First, from the reaction process, when $(NH_4)_6H_2W_{12}O_{40}$ and $CuCl_2 \cdot 2H_2O$ are dissolved in an aqueous solution under high temperature and high pressure, the following reactions are produced:

$$NH_4^+ + H_2O \leftrightarrow NH_3.H_2O + H^+ \quad (20)$$

$$6H^+ + H_2W_{12}O_{40}^{6-} + 8H_2O \rightarrow 12WO_4^{2-} + 24H^+ \quad (21)$$

Under acidic condition, the nucleation and growth of $CuWO_4$ structures are produced by the following reaction:

$$WO_4^{2-} + Cu^{2+} \rightarrow CuWO_4 \quad (22)$$

As reported previously, in the heterogeneous nucleation process, which is the formation of nanoparticles onto a substrate, the generation of particles begins with the formation of tiny nuclei on substrate followed by growth. This process is thermodynamically unstable until its free energy has reached a minimum. This is because the large interfacial area contributes to the free energy, that may be reduced by decreasing this area. Ostwald (1901) provided the first description of this process, which therefore was later called "Ostwald ripening." This term will be discussed in detail in section 4.1.3.1 [125].

Herein, $CuWO_4$ undergoes primary heterogeneous nucleation, which results in the formation of single crystals. The $CuWO_4$ crystals have crystalline boundaries and grains that are thermodynamically unstable and include more defects. Each grain of the original $CuWO_4$ crystals may have prioritized growing along one growth direction, and a significant percentage of growth units may result in secondary growth from the defects. Additionally, the crystal surfaces containing defects tend to further decrease their energy through surface reconstruction, providing active sites for secondary nucleation. As a result, dandelion-like structures were assembled during hydrothermal reaction [61, 126].

4.1.2 Influence of different ratios between precursors (Cu:W) on dandelion-like structures

4.1.2.1 SEM/EDX results

The understanding of the interconnections existing amongst the stoichiometry, morphology, and photoelectrochemical (PEC) properties of the produced composite structures is of great practical significance in enhancing the efficiency of composite fabrication. Therefore, an analysis was conducted to determine the influence of the precursor proportions on the stoichiometry, morphology, and PEC effectiveness of the $CuWO_4/WO_3$ composite synthesized through hydrothermal means. For this purpose, three different ratios of copper and tungsten precursors (Cu:W); (2:1), (1:2), and (1:1) were employed, respectively. The corresponding scanning electron microscopy images and elemental composition results are represented in following. The SEM images showed the significant change in the shape, size and distribution of synthesized structures can achieved through the variation of precursors ratios.

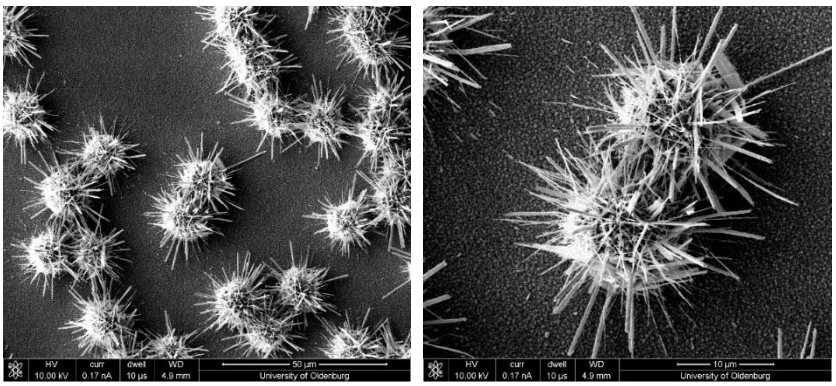

Figure 23. Top view SEM images of dandelion-like $CuWO_4$ thin film with the ratio of (Cu:W)(2:1).

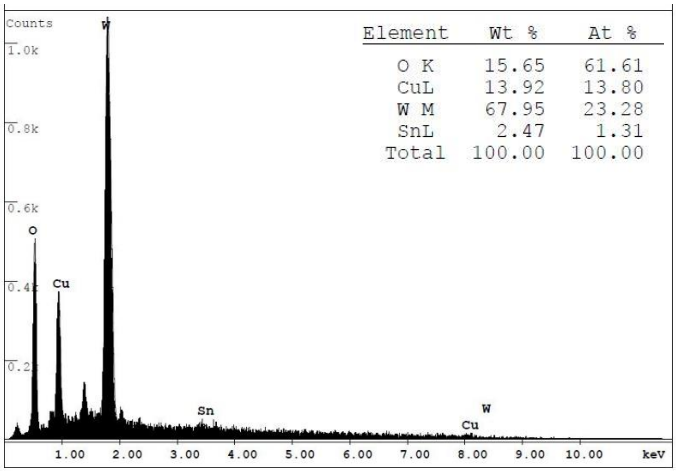

Figure 24. EDS spectra of $CuWO_4$ thin film with the ratio of (Cu:W)(2:1).

According to the scanning electron microscopy (SEM) images (Figure 23), it can be observed that the substrate, for the (2:1) (Cu:W) ratio, exhibits conspicuous microstructures that are significantly large, measuring approximately 13 µm on average. These microstructures are randomly dispersed on the surface of the photoanode. The elements composition of $CuWO_4$ film was analyzed by energy dispersive X-ray spectrometer (EDS) (Figure 24). The result of EDS analysis shows that the atom content of O, Cu, W in film was 61.61%, 13.80%, and 23.28% respectively. For the second ratio which is (1:2) (Cu:W), the substrate surface is fully covered with a blend of plate-shaped and flower-shaped arrays (Figure 25). It is worth noting that this particular configuration exhibits inferior photoelectrochemical performance, which can be attributed to the limited number of active sites available for surface reactions. The result of EDS analysis depicts that the atom content of O, Cu, W in film was 64.41%, 2.48%, and 27.18%, respectively (Figure 26).

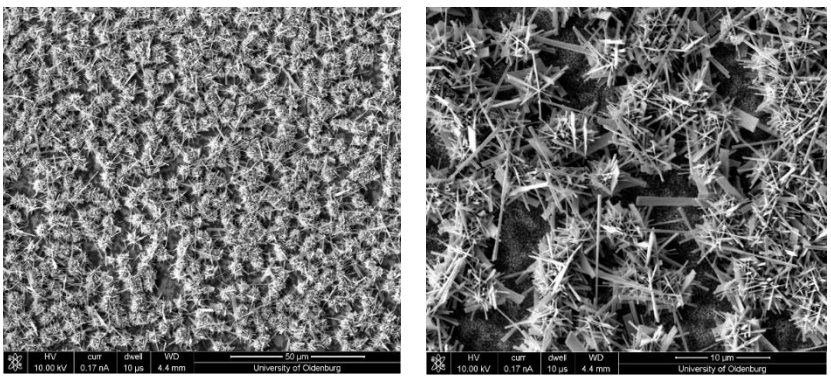

Figure 25. Top view SEM images of dandelion-like $CuWO_4$ thin film with the ratio of (Cu:W)(1:2).

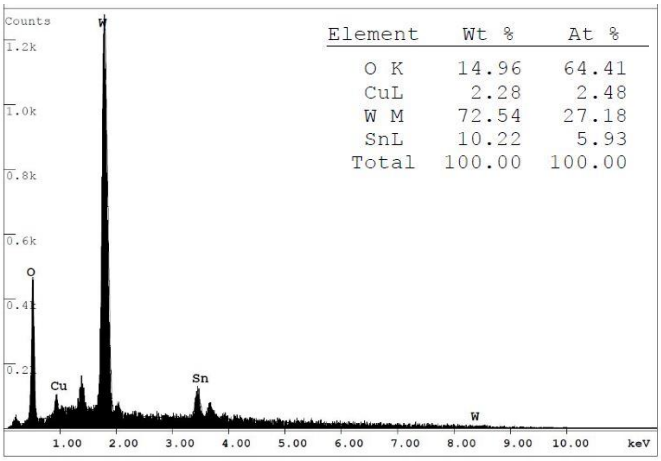

Figure 26. EDS spectra of $CuWO_4$ thin film with the ratio of (Cu:W)(1:2).

Ultimately, the SEM images of equal ratio of precursors (Cu:W)(1:1), indicate the equel distribution of dandelion-like microstructure arrays with the average size of 5 μm onto a substrate (Figure 27). The result of EDS analysis displays that the atom content of O, Cu, W in film was 62.22%, 8.25%, and 21.27%, respectively (Figure 28). These results suggested that as-prepared $CuWO_4$ films are W-rich on the surface [29].

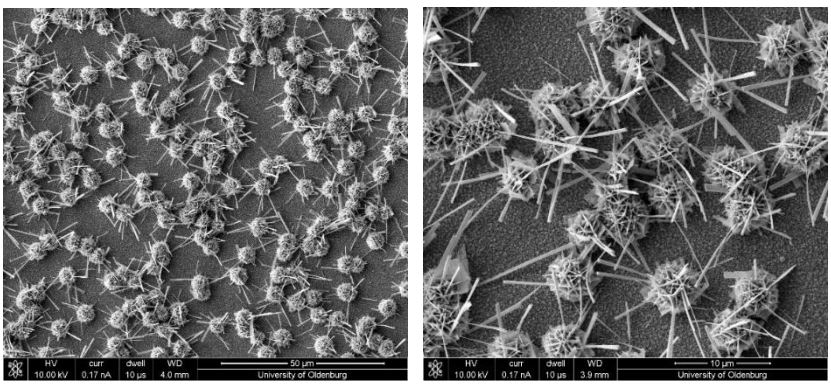

Figure 27. Top view SEM images of dandelion-like $CuWO_4$ thin film with the ratio of (Cu:W)(1:1).

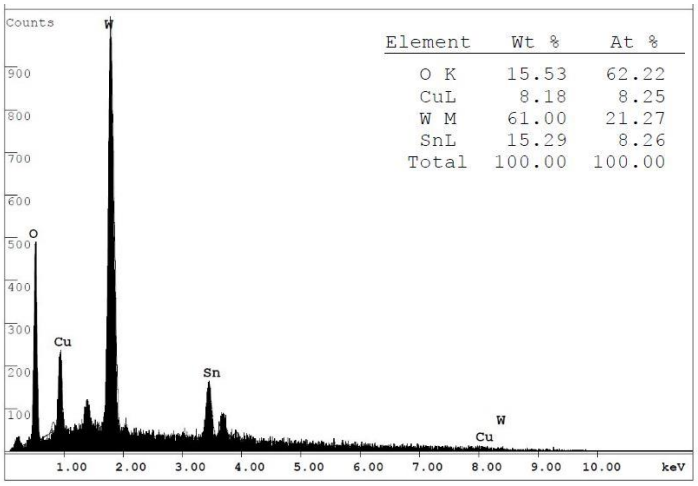

Figure 28. EDS spectra of $CuWO_4$ thin film with the ratio of (Cu:W)(1:1).

The EDX results for all three precursors ratios demonstrate that the quantity of Cu on the surface of the thin film is significantly lower than that of W. This observation aligns with findings reported in previous studies [53, 127]. Based on the earlier studies, during the initial stage of the hydrothermal reaction, a compact layer primarily composed of Cu element is formed on the FTO substrate. As the reaction proceeds, an excess amount of W precursor in the solution leads to the formation of spherical structures, which subsequently undergo a transformation into dandelion-like formations. This in-situ deposition method results in a greater contribution of W on the uppermost layer of the thin film compared to Cu. Detailed information can be found in the section 4.1.4.1 [127].

4.1.2.2 Photoelectrochemical results

As depicted in Figure 29, the optimal photoelectrochemical performance can be attributed to the balanced proportion of copper and tungsten in the precursors mix. The SEM images indicate that the enhanced photoelectrochemical activity is correlated with the photoanode's morphology. Specifically, when the surface features homogeneous distribution of dandelion-like microstructures, the highest performance is achieved. It is noteworthy that there exists an optimal level of this distribution, and deviation from this optimal amount leads to a decrease in activity. This optimal level of distribution implies that the microspheres do not aggregate densely on the surface in a manner that completely covers the entire surface, as depicted in Figure 25. Similarly, they are not randomly distributed on the surface with significant gaps

between them, as shown in Figure 23. Conversely, the superior 3D dandelion-like arrays on the photoanode's surface facilitate efficient charge carrier separation.

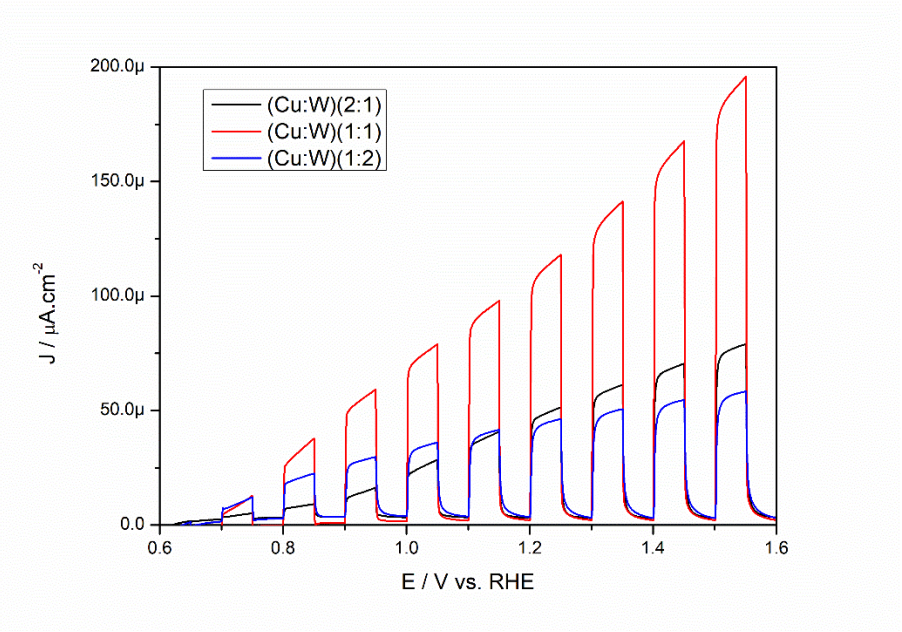

Figure 29. Chopped light linear sweep voltammogram of $CuWO_4/WO_3$ photoanode with various precursor's ratios (Cu:W) under chopped illumination measured in 0.1 M Na_2SO_4 (pH 7 PBS).

4.1.3. Influence of hydrothermal reaction parameters on dandelion-like structures

4.1.3.1 SEM results

Through controlling the hydrothermal reaction parameters, the morphological evolution and crystal growth mechanism of $CuWO_4$ were evaluated. Figure 30.1 show the scanning electron microscopy (SEM) images of the $CuWO_4$ samples which were synthesised with different precursors concentration. At the beginning, in low concentration of precursors, small and compact plate-like and wire-like structures were formed on a surface of uniform dense layer which composed of small grains on the FTO surface. By further increasing a concentration, new wire-like structures with a growth orientation outward of the surface emerged. The wire-like structures are well-arranged in parallel way, consisting of several sub-wires extending radially outward which created a dandelion-like microsphere structure with average diameters of ca. 5 µm (Figure 30(b.1)). The further increase of concentration impelled dandelion-like structures with larger diameters which even possesses a magnitude around 35 µm with longer wires around them (Figure 30(f.1)). Subsequently, the effect of various reaction temperatures reveals when the temperature is increased to 200 ˚C and higher, a significant difference in

morphology appears and the wire-like parts began to grow laterally on the outer surfaces of the microsphere and covering the whole surface (Figure 30(e.2)). Moreover, by changing the time of reaction, the coverage of dandelion structures on the surface were tuned and the highest coverage was achieved after the duration of 8 h. (Figure 30(c.3)).

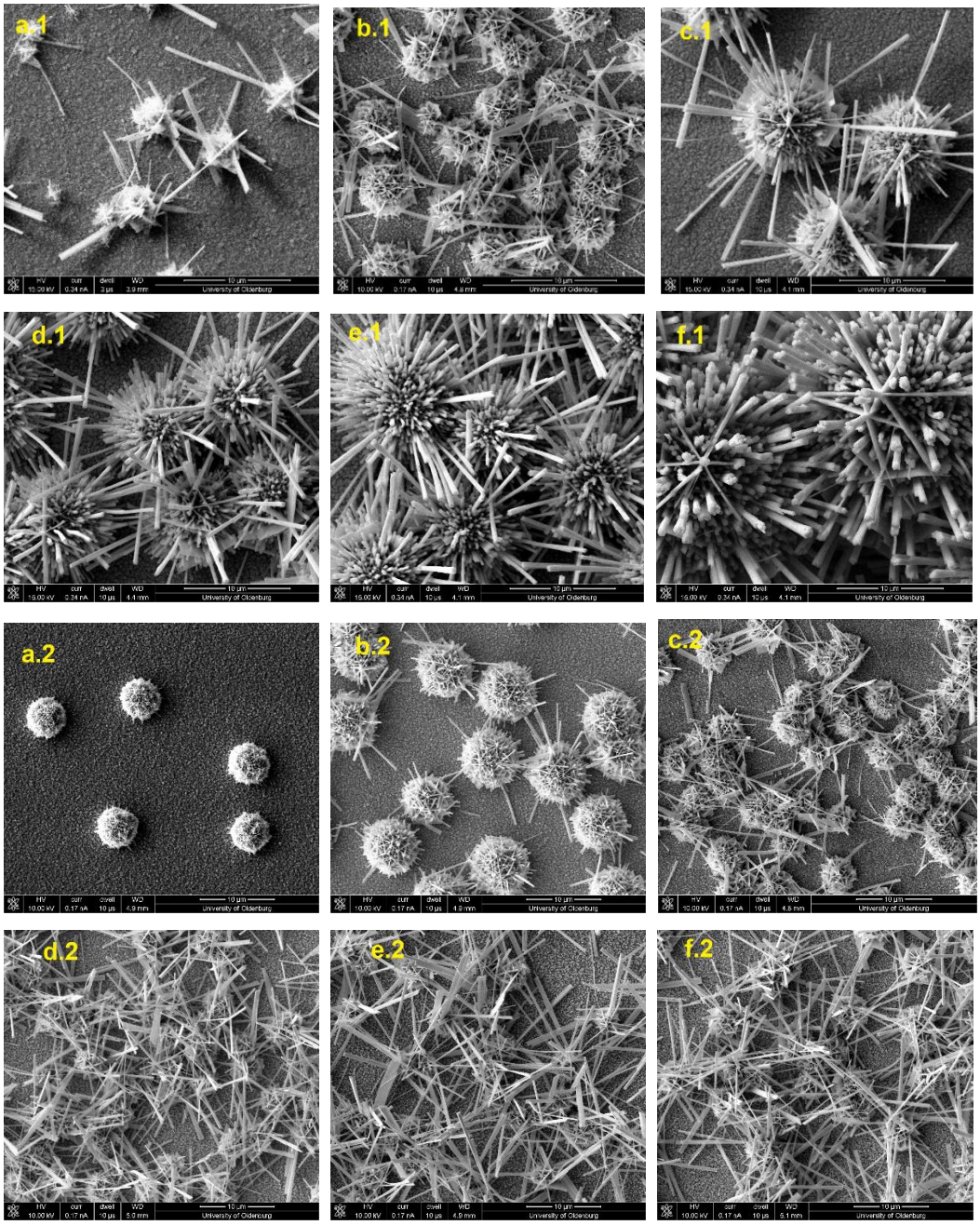

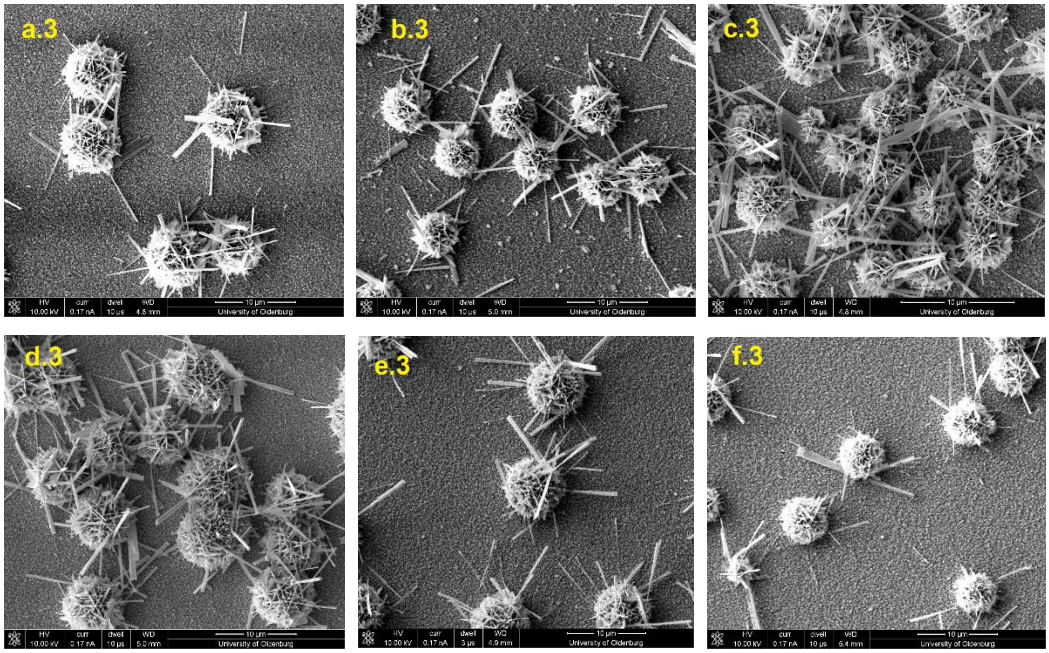

Figure 30. Top view SEM images of $CuWO_4/WO_3$ films with different hydrothermal parameters, **(a.1-f.1)** *Precursor Concentration (mM):* 1 mM(a.1), 2 mM(b.1), 3 mM(c.1), 4 mM(d.1), 5 mM(e.1), 10 mM(f.1); **(a.2-f.2)** *Temperature (˚C):* 140 ˚C (a.2), 160 ˚C (b.2), 180 ˚C (c.2), 200 ˚C (d.2), 220 ˚C (e.2), 240 ˚C (f.2); **(a.3-f.3)** *Time (h):* 4 h(a.3), 6 h(b.3), 8 h(c.3), 10 h(d.3), 12 h(e.3), 14 h(f.3).

Growth mechanism:

The capability to grow and align anisotropic nanoparticles into extensive arrays on a substrate necessitates the consideration of both homogeneous and heterogeneous nucleation phenomena. Typically, the nucleation of solid phases (specifically metal oxide) through homogeneous means demands a greater activation energy barrier. As a result, hetero nucleation is encouraged and proves to be energetically more advantageous. This is due to the interfacial energy between the crystal and the substrate is smaller than the interfacial energy between the crystal and the solution. Consequently, nucleation may occur at a lower saturation ratio on a substrate compared to in a solution. Nuclei will emerge across the entire substrate, and if their rate is regulated and restrained by the precipitation conditions, epitaxial crystal growth will occur from these nuclei, following the easy direction of crystallization [77].

The phenomenon of phase transformation in solution, as observed in crystallography, usually occurs by means of a process involving dissolution and subsequent recrystallization. This process aims to minimize the overall surface energy exhibited by the system. It is worth noting that when a solid material possesses multiple allotropic phases, it is typically the phase characterized by the lowest stability and the highest solubility (also known as the crystallographic metastable phase) that undergoes precipitation first. This can be

comprehended by analysing the kinetics of nucleation exhibited by the solid material. According to the principle established by Ostwald, the driving force in precipitation is the difference in solubility between the particles of the solid phase, as given by the well-known Gibbs-Thomson equation, Eq. (23). The Gibbs-Thomson equation links crystal size with the equilibrium solubility. For crystal-solution equilibrium, the solubility $C_{eq}(r)$ of spherical crystals of radius r is related to the solubility $C_{eq}(\infty)$ of crystals of very large sizes by the equation:

$$\ln \frac{C_{eq}(r)}{C_{eq}(\infty)} = \frac{2\sigma V_m}{RT_r} \qquad (23)$$

where σ is the surface energy of the solid phase, V_m is the molar volume, R is the universal gas constant, and T is the absolute temperature. According to Eq. (23), the solubility of a substance increases with decreasing crystal size. Principally, the surface tension forces between the crystal and the solution cause this larger solubility of small crystals [77, 125].

Based on the above definitions and the findings from additional examinations (EDX (4.1.4.1), Raman (4.1.4.2), GIXRD (4.1.4.3)) in the subsequent sections, the growth mechanism of CWO films can be described as follows. During the initial stages of the hydrothermal reaction, under specific conditions of a particular supersaturation ratio, when the interfacial tension of the system is at a diminished level, nucleation commences on the FTO substrate. Subsequently, the growth of CWO crystals ensues from these nuclei. Considering the initial crystals possess thermodynamically unstable boundaries and grains, crystallization tends to progress in the most facile direction to minimize energy. Consequently, surface reconstruction further contributes to the formation of a dandelion-like structure.

In greater detail, during the initial stages of the hydrothermal reaction, there is a growth of a dense layer on the FTO substrate. This layer primarily consists of the $CuWO_4$ phase, with an additional presence of excess W element leading to the formation of the WO_3 phase. As the reaction time increases, the surplus W precursor in the solution leads to the generation of spherical structures, which subsequently evolve into a dandelion-like configuration [127]. By considering the Ostwald step rule, it can be deduced that the $CuWO_4$ crystals constitute the most soluble phases and are the least thermodynamically stable phases, thereby precipitating first on the FTO substrate.

4.1.3.2 Photoelectrochemical results

The photoelectrochemical (PEC) studies of each $CuWO_4/WO_3$ thin films which were prepared with various hydrothermal reaction parameters are shown in this section; different precursor concentrations, different temperatures of hydrothermal reaction, different periods of hydrothermal reaction; (Figures 31, 32, 33), respectively.

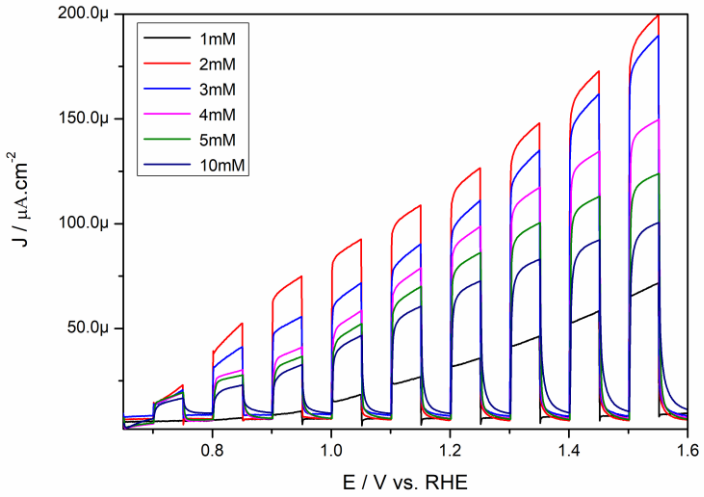

Figure 31. Chopped photocurrent density of $CuWO_4/WO_3$ thin films prepared with different precursor concentrations.

For various concentrations of precursors, the results obtained from photoelectrochemical (PEC) analysis indicate that the highest response is observed in the sample prepared with a concentration of 2 mM precursors. As the concentration is increased more than 2 mM, the photocurrent decreases. The corresponding scanning electron microscopy (SEM) images demonstrate that at higher concentrations, the diameter of the dandelion-like microstructures increases and covers the entire surface of the photoelectrode. (Figure 30, a1-f1).

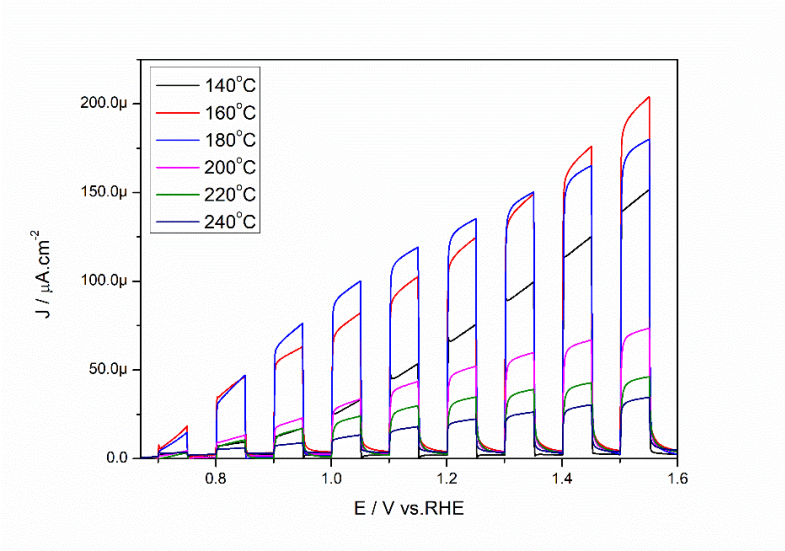

Figure 32. Chopped photocurrent density of $CuWO_4/WO_3$ thin films prepared at different temperatures of hydrothermal reaction.

The PEC results obtained for the samples prepared at different hydrothermal reaction's temperatures reveal that the highest photocurrent is attributed to the sample synthesized at a temperature of 180 °C. As the temperature increases beyond this point, the photocurrent intensity decreases. The SEM images of the same samples show that at synthesis temperatures higher than 180 °C, the wire-like parts of the dandelion structures grow more prominently than the spherical parts, eventually covering the entire surface of the photoanode. (Figure 30, a2-f2).

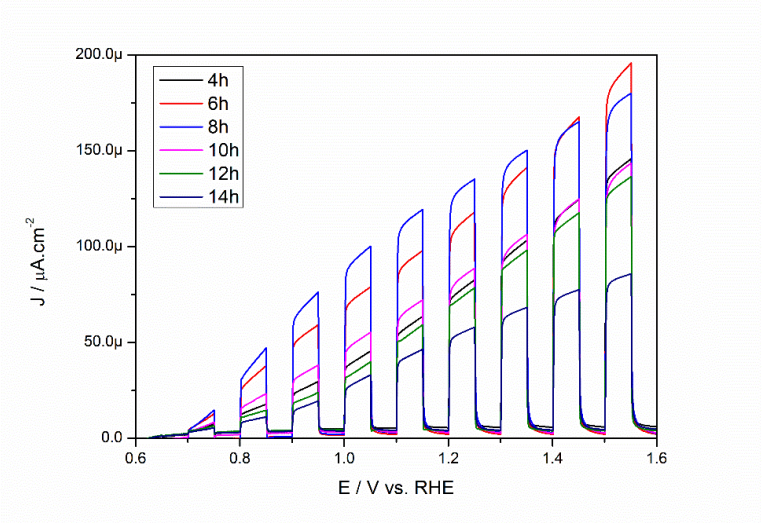

Figure 33. Chopped photocurrent density of $CuWO_4/WO_3$ thin films prepared at different periods of hydrothermal reaction.

In regard to the time of reaction, the PEC observation exhibits a positive correlation between the highest photocurrent and an 8-hour duration. Similar trends were observed like other

parameters, wherein a longer reaction time led to a decrease in the magnitude of the photocurrent. The SEM images further revealed that the coverage of the surface with microspheres varied over time. In the case of a sample prepared for 8 hours, the microspheres were evenly distributed across the surface, whereas in longer reaction times, the coverage was inferior compared to the 8-hour sample.

Overall, the SEM observations have verified the findings of PEC measurements. It has been determined that achieving full coverage of the photoanode's surface leads to a reduced number of available active sites for photoelectrochemical reactions at the electrode/electrolyte interface, resulting in a diminished photocurrent response. Similarly, the presence of randomly distributed microspheres with significant gaps on the photoanode's surface leads to a decrease in photoactivity at the electrode/electrolyte interface. With respect to the reaction time parameter, in addition to the quantity of accessible active sites on the surface, the obstacle of the PEC reaction may reside in the thickness of the film. By prolonging the reaction time, the film's thickness was enhanced, and a thick film could potentially impede the transportation of charge carriers and result in an elevated rate of recombination.

These PEC measurements indicated that the highest photocurrent is corresponding to $CuWO_4/WO_3$ photoanode prepared from 2 mM precursor concentration, at 180 $^{\circ}$C for the duration of 8 h of hydrothermal synthesis process. This photoanode was chosen as an optimum sample for further investigation.

4.1.3.3 Raman spectroscopy results

Raman analyses were applied to further determine the surface property and phase information of the as prepared photoanode. Regarding the SEM images from $CuWO_4$ samples, they consist of two different areas - dense flat surface and microsphere dandelion-like structures on top. The Raman spectra of these two different areas of samples which were prepared in the lowest and highest regimes of hydrothermal reaction parameters e.g., concentration of precursors (1 mM, 10 mM), time of reaction (4 h, 14 h), and temperature of reaction (140 $^{\circ}$C, 240 $^{\circ}$C) were studied. The Raman spectra and corresponding SEM images are presented in Figures 34, 35, 36, respectively.

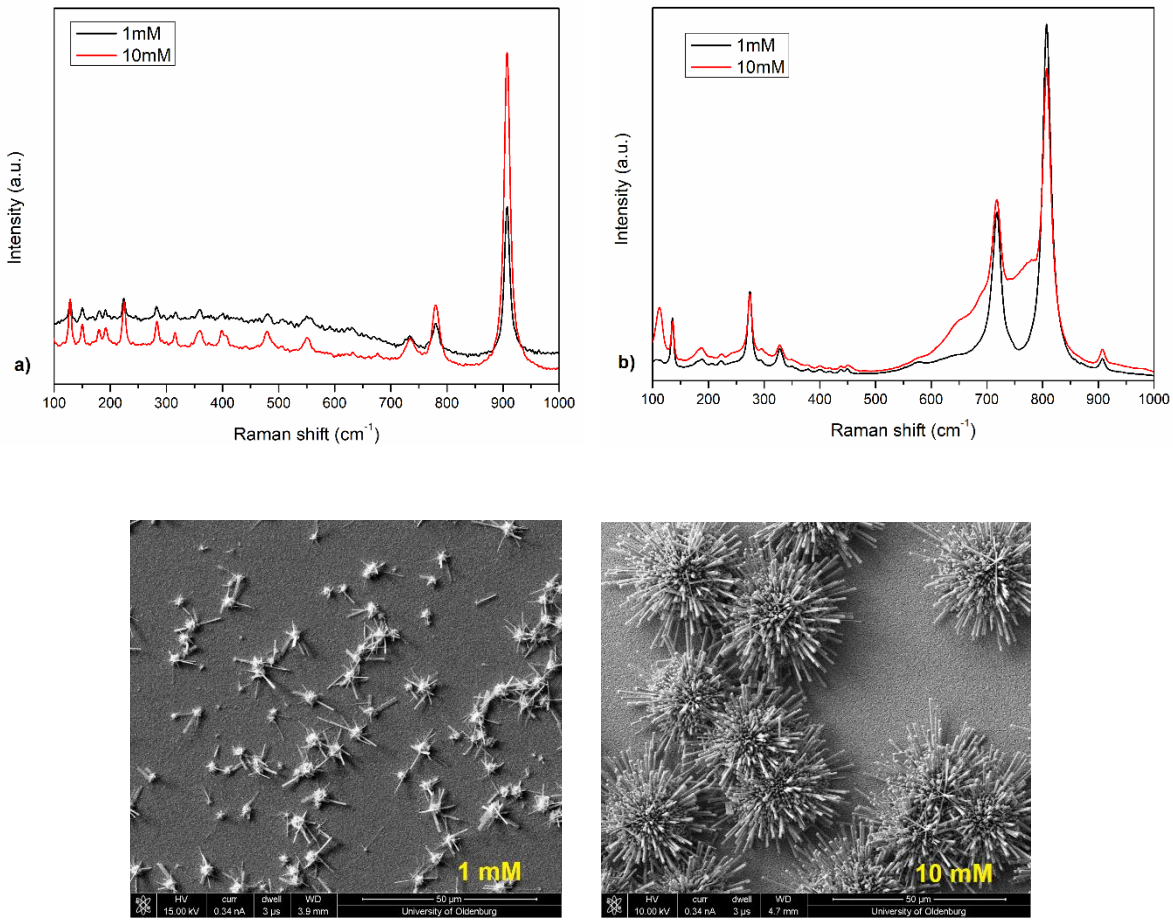

Figure 34. Raman spectra a) flat area, b) sphere area of $CuWO_4/WO_3$ composite film prepared with precursor concentration of 1 mM and 10 mM and corresponding SEM images.

The Raman spectra of flat area for all samples (Figures 34a, 35a, 36a) demonstrate the sharp and intense vibrational Raman mode at around 905 cm^{-1} in agreement with triclinic structural $CuWO_4$ reported in the previous literature [128]. Only in sample related to the high temperature (240 ˚C) the intensity of $CuWO_4$ peak is decreased and intense peaks at 805 and 715 cm^{-1} are visible, which are attributed to the stretching vibrations of bridging oxygen in O–W–O. It means that in high hydrothermal temperature conditions the dominant phase is WO_3. The Raman peaks at 274, 327, 715, and 805 cm^{-1} are assigned to monoclinic type WO_3 structure. The peaks located in 274 and 327 cm^{-1} Raman mode are corresponding to bending vibration of O–W–O. Raman spectra of sphere area of all the samples clearly exhibit the intense peaks of monoclinic type WO_3 structure. For samples prepared in high concentration and high temperature, a wide shoulder in the 590–690 cm^{-1} region may result from the transition between different WO_3 crystallographic phases. Meanwhile, there is a peak at the lower wavenumber of 140 cm^{-1} which can be attributed to lattice modes [127, 129].

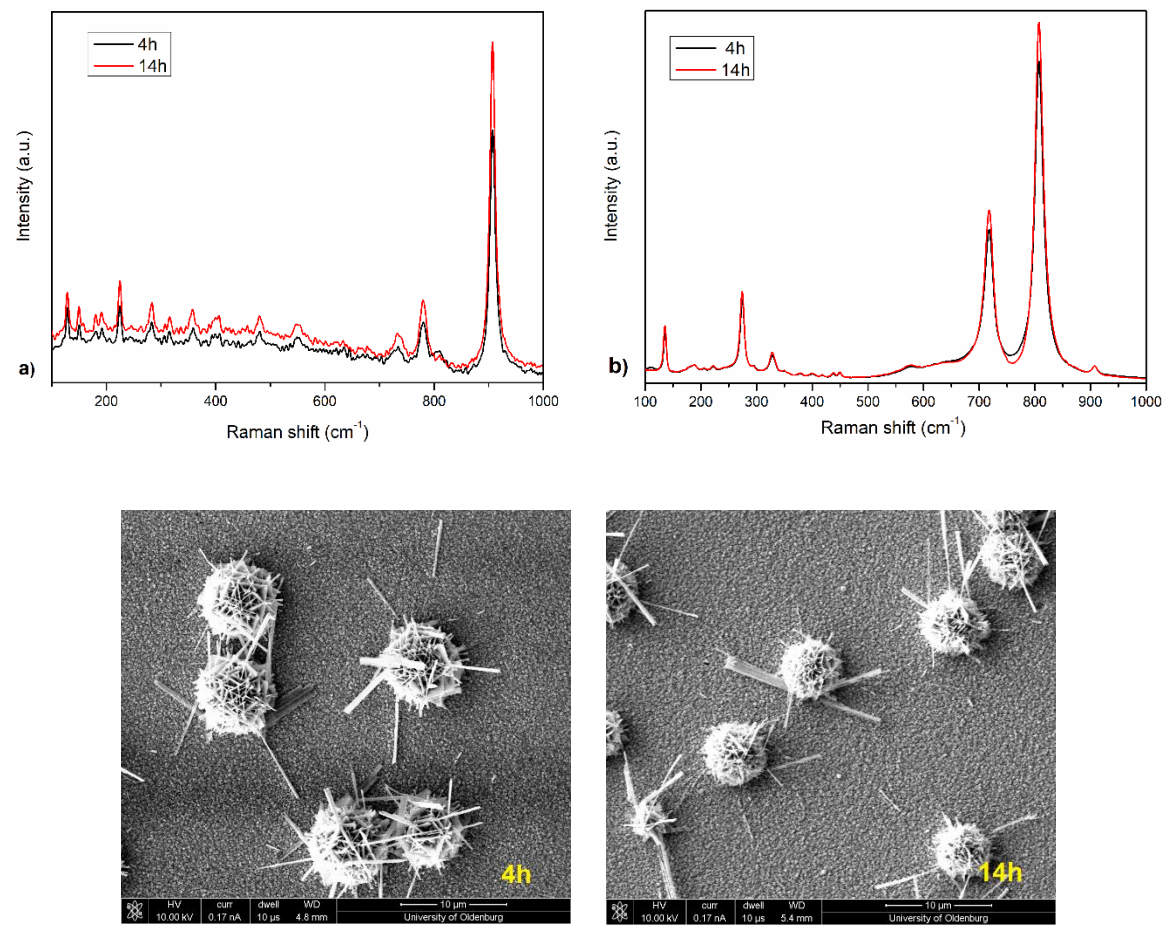

Figure 35. Raman spectra a) flat area, b) sphere area of $CuWO_4/WO_3$ composite film prepared with hydrothermal method in a period of 4 h and 14 h and corresponding SEM images.

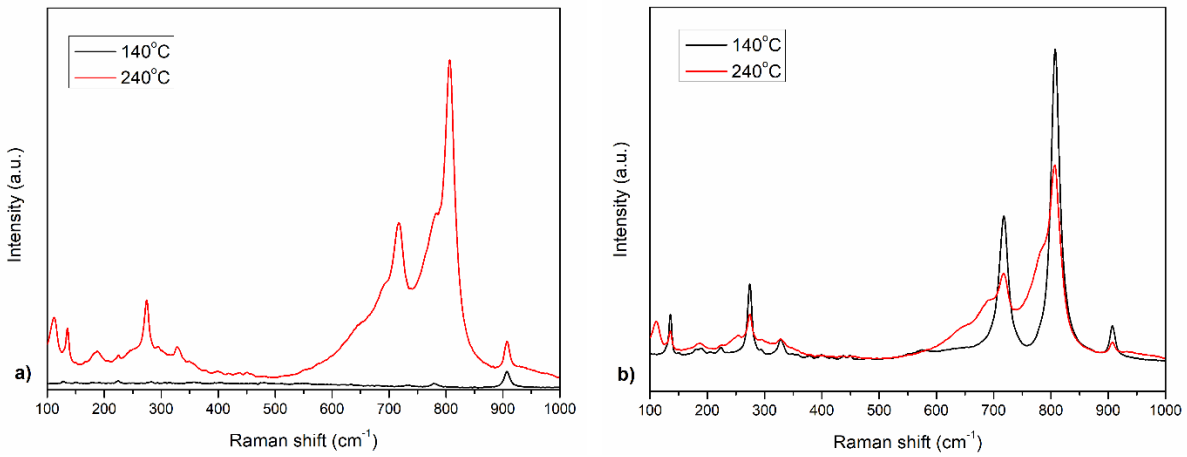

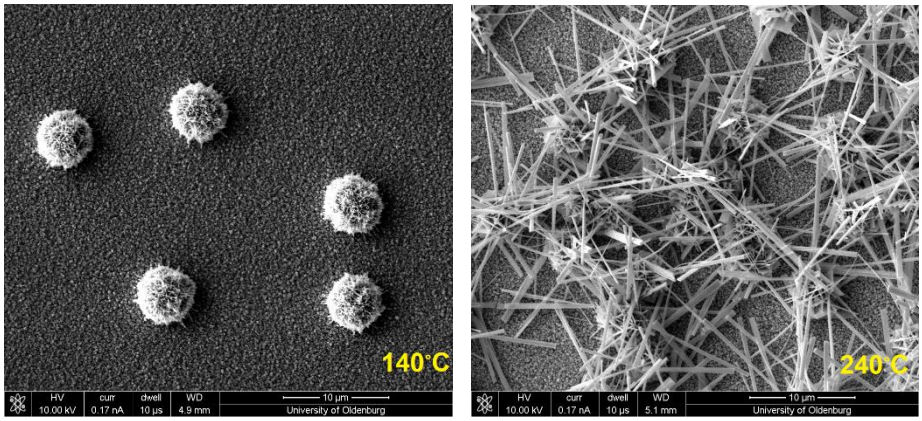

Figure 36. Raman spectra a) flat area, b) sphere area of $CuWO_4/WO_3$ composite film prepared with hydrothermal method with temperatures at 140 ˚C and 240 ˚C and corresponding SEM images.

4.1.4 Characteristics of optimum dandelion-like $CuWO_4/WO_3$ thin film

4.1.4.1 EDX results

The elements composition of correlated dandelion-like $CuWO_4/WO_3$ thin film was analzed by energy dispersive X-ray spectrometer (EDS) (Figure 37).

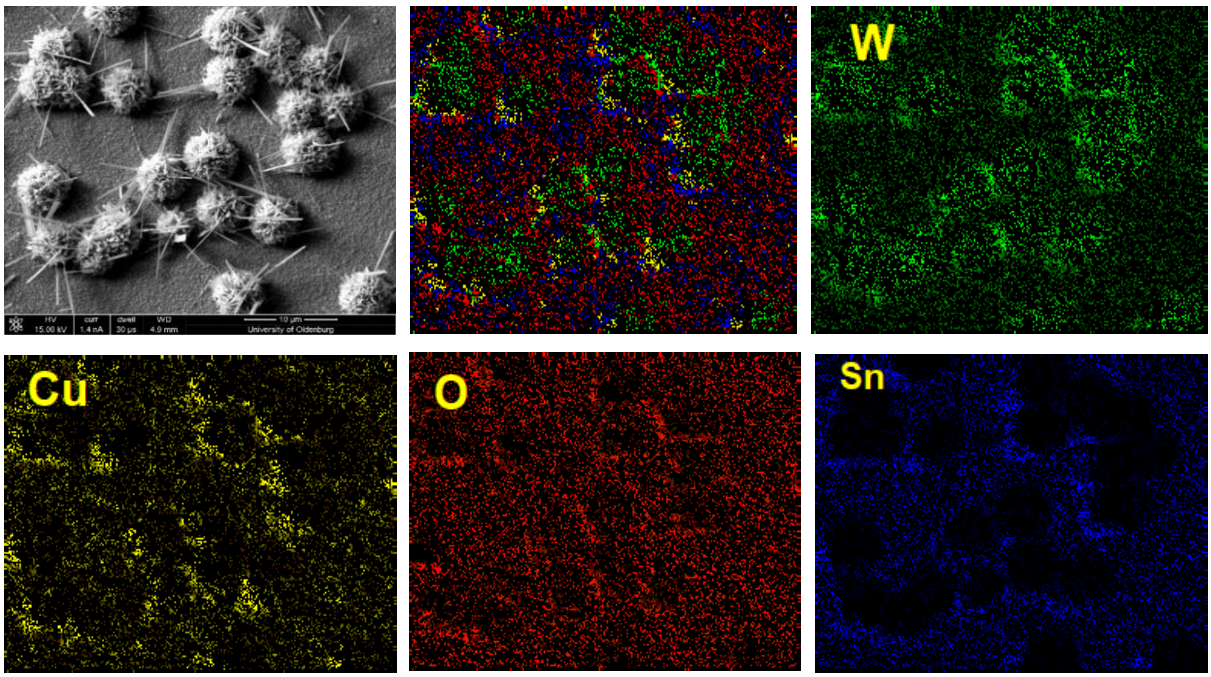

Figure 37. SEM image and element distribution mapping of $CuWO_4/WO_3$ film with hydrothermal reaction for 8 h at 180 ˚C.

The result of EDS analysis verifies the presence of Cu, W, O, and Sn elements onto the thin film. The W element mostly exists on a microsphere of the dandelion-like structures. The Cu element is mainly distributed on a flat part of the film near the Sn element. The O element has uniform distribution along the film. Since the FTO is F doped SnO_2, the Sn element and substrate correlate well. This observation aligns well with the findings in the existing literature, which have demonstrated a consistent distribution pattern for the $CuWO_4$ film on the FTO substrate. A previous study using cross-sectional elemental mapping revealed that the copper (Cu) element tends to predominantly follow a path along the condensed layer, particularly close to the Sn element while exhibiting a decrease in cohesion as it moves away from the substrate. Conversely, the tungsten (W) element shows a greater distribution in the upper layers, further away from the substrate [127].

Furthermore, EDS spectra, mass, and atomic percentages for all elements are demonstrated in Figure 38 and Table 1, respectively.

Table 1. Elemental composition

Element	Weight%	Atomic%
O K	15.53	62.22
Cu L	8.18	8.25
W M	61.00	21.27
Sn L	15.29	8.26
Total	100.00	100.00

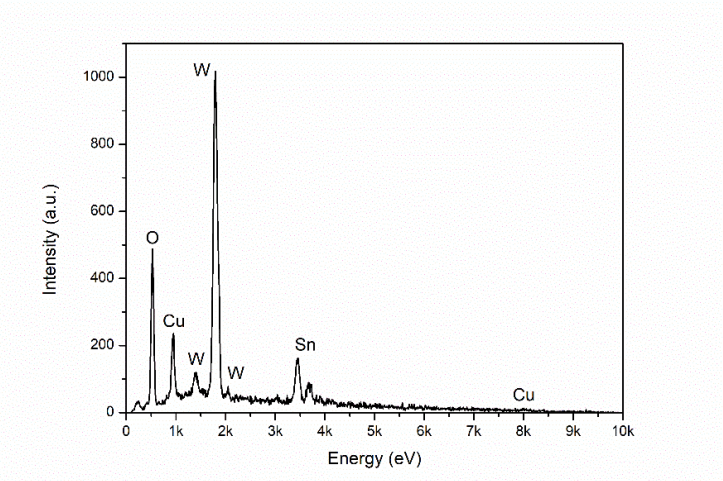

Figure 38. EDS spectra of $CuWO_4/WO_3$ composite film.

This specific distribution pattern (Figure 37) and elemental composition table (Table 1) indicated that the synthesized thin films possess a higher quantity of W element on the top layer compared to Cu.

4.1.4.2 Raman spectroscopy results

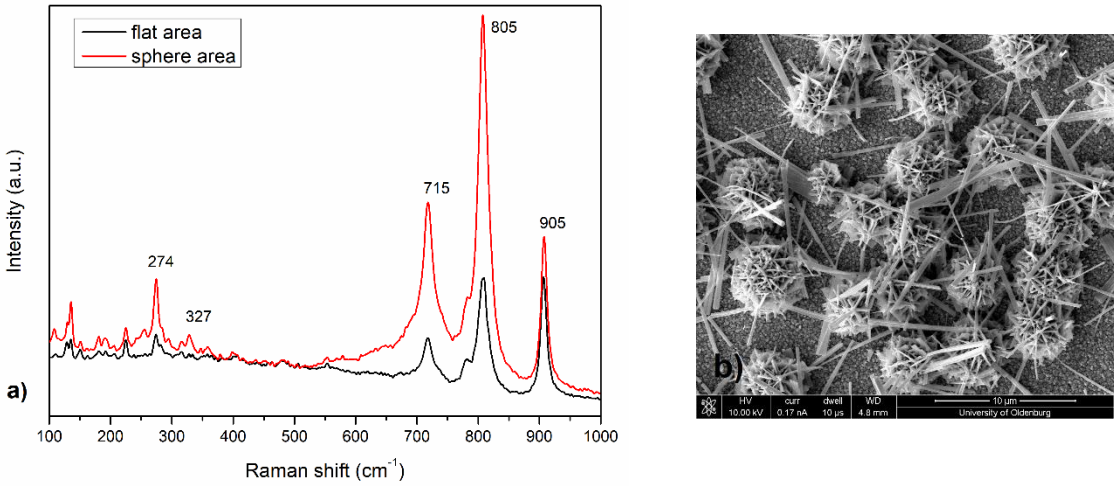

Figure 39. a) Raman spectra, b) top SEM image of $CuWO_4/WO_3$ composite film.

Figure 39 depicts the Raman spectra and SEM image of the optimum $CuWO_4$ sample regarding its PEC performance which was prepared by following parameters: Concentration: 2 mM, Time: 8 h, Temperature:180 ˚C. The Raman analysis reveals that as-prepared photoanodes are the composite of $CuWO_4/WO_3$ with a structure consisting of $CuWO_4$ as a dense homogenous layer on surface of FTO and dandelion-like microsphere of WO_3 onto the dense surface.

4.1.4.3 GIXRD results

The utilization of the X-ray diffraction technique can effectively disclose the structures of materials due to its quantitative and non-destructive analytical features. In the scenario of thin films, the implementation of grazing geometry is imperative in elevating the interaction of X-rays with the materials in the films. This method facilitates the acquisition of information from planes perpendicular to the surface, resulting in a reduction of the sufficient depth of X-ray penetration perpendicular to the surface as the angle of incidence declines until it reaches the critical angle limit, beyond which total reflection occurs [130]. The present geometry employed for measurement is commonly referred to as Grazing Incidence X-ray Diffraction (GIXRD).

In Figure 40, the GIXRD patterns of the optimal $CuWO_4/WO_3$ film, in terms of its photoelectrochemical (PEC) performance, are exhibited, where the measurements were conducted at different incident angles of 0.5°, 1° and 2°. At a low incident angle of 0.5°, the penetration depth of X-rays into the film is limited to a few nanometers. As a result, the diffraction pattern obtained in this case solely reflects the structure of the surface layer, which is characterized by the main diffraction peaks of monoclinic WO_3 structures located at 2θ angle of 23.1, 23.6 and 24.4 which corresponds to (002), (020) and (200) planes, respectively. Additionally, the low-intensity peak at 2θ = 19.0° corresponds to the (100) plane of triclinic $CuWO_4$. The observed alterations in intensity under the higher angle indicate the presence of a greater quantity of $CuWO_4$ near to FTO. When the angle of incidence was set at 0.5°, the diffraction peaks of the monoclinic WO_3 phase were found to be dominant, while the peaks of the triclinic $CuWO_4$ phase were comparatively weak. This is due to variations from the surface to the interface corresponding to the incident angle from 0.5° to 2°.

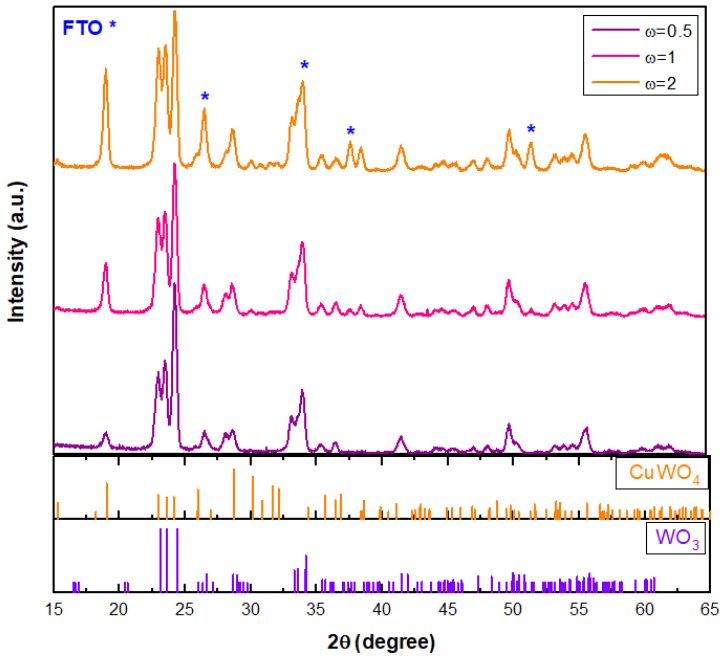

Figure 40. GI-XRD pattern of $CuWO_4/WO_3$ composite film at different incident angles (ω= 0.5°, 1°. 2°).

It can be concluded from these observations that there are composite of $CuWO_4$ and WO_3 present on the FTO surface. During the initial stages of film growth, $CuWO_4$ was deposited on the surface and, with further growth of the film, WO_3 gradually accumulated on the $CuWO_4$ layer. This finding is consistent with the results obtained from Raman and EDX measurements.

4.1.4.4 XPS results

The utilization of the X-ray photoelectron spectroscopy (XPS) technique facilitated the investigation of the chemical states and elemental nature of the synthesized thin films' surface. Analysis of the core-level Cu 2p XPS revealed that the Cu $2p_{3/2}$ and Cu $2p_{1/2}$ peaks' positions, centered at binding energies of 934.6 and 954.4 eV, were characteristic of Cu^{2+} located in the $CuWO_4$ lattice sites, as depicted in Figure 41a [48]. Furthermore, the high-resolution W4f XPS spectra could be separated into a pair of W $4f_{7/2}$ and W $4f_{5/2}$ peaks with binding energies of 35.4 and 37.6 eV, respectively, as shown in Figure 41b. These peak energies are assigned to the W^{6+} standard peaks. The high-resolution spectrum of O1s was comprised of two peaks situated at 530.1 and 531.3 eV, which were identified as the lattice oxide and surface hydroxide, respectively, as illustrated in Figure 41c [127].

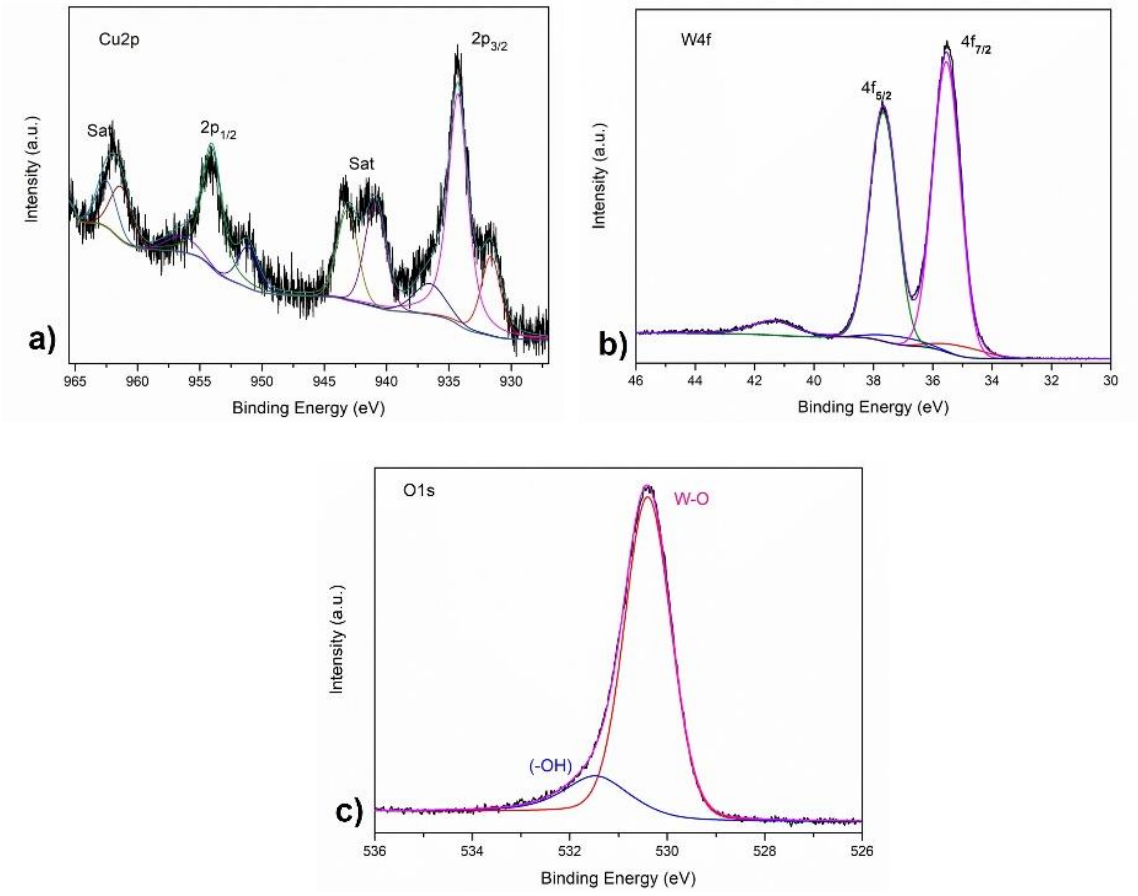

Figure 41. High resolution a) Cu 2p, b) W 4f, and c) O 1s XPS spectra of $CuWO_4/WO_3$ composite film.

4.2 NiCo-LDH catalyst

4.2.1 Mechanism reaction

The procedure for producing the NiCo-LDH compound is delineated as follows. Initially, ammonia was gradually generated through the process of urea hydrolysis, as illustrated in equation 24. Subsequently, the ions Co^{2+} and Ni^{2+} exhibit the highest tendency to function as Lewis acids, thereby resulting in their inclination to form complex ions. Concurrently, present ammonia in a solution is a stronger base in comparison to H_2O with a lone pair of electrons which allows amines to act as Lewis bases, meaning it can donate an electron pair to form a coordinate covalent bond with a Lewis acid. Conversely, the high formation constant (K_f) values of both $[Ni(NH_3)_6]^{2+}= 5.5\times10^8$ and $[Co(NH_3)_6]^{2+}= 1.3\times10^5$ has led to the development of ammonia complexes, as demonstrated in equation 25. Furthermore, an excess amount of NH_3 molecules gave rise to OH^-, and as a consequence, the nickel and cobalt ions formed $Ni(OH)_6$ and $Co(OH)_6$ octahedra with OH^-, as depicted in equations 26 and 27.

$$CO(NH_2)_2 + 2H_2O \rightarrow H_2CO_3 + 2NH_3 \quad (24)$$

$$Ni^{2+} + 6NH_3 \leftrightarrow [Ni(NH_3)_6]^{2+} \; ; \; Co^{2+} + 6NH_3 \leftrightarrow [Co(NH_3)_6]^{2+} \quad (25)$$

$$NH_3 + H_2O \leftrightarrow NH_4^+ + OH^- \quad (26)$$

$$2OH^- + Ni^{2+} \leftrightarrow Ni(OH)_2 \; ; \; 2OH^- + Co^{2+} \leftrightarrow Co(OH)_2 \quad (27)$$

The nuclei of $Ni(OH)_6$ and $Co(OH)_6$ octahedra underwent self-assembly to generate infinite 2D sheets comprised of metal cations residing at the center of the octahedra's edges and hydroxide ions positioned at the vertexes. These 2D sheets subsequently extended to produce the NiCo-LDH nanosheets, which were subsequently cleaned with ethanol and water. It is anticipated that H_2O molecules and NO_3 ions shall be conserved within the interlayer cavity of LDH through hydrogen bonding [131].

4.2.2 XRD results

The X-ray diffraction (XRD) patterns of the NiCo layered double hydroxide (LDH) with varying mass ratios between Ni and Co are illustrated in Figure 42. In the mixed samples of Ni and Co with different ratios, the reflection peaks at 2θ of 11.3, 23.0, and 34.3° are attributed to the (003), (006), and (009) planes of the hydrotalcite-structured NiCo-LDH [131, 132]. Conversely, the pure Ni sample exhibited intense and sharp diffraction peaks of (001), (100), (101), and (102) planes at 2θ values of 19, 33, 38, and 51°, respectively, assigned to the β-$Ni(OH)_2$ phase [133]. As-prepared Co-LDH exhibited diffraction patterns of α-hydroxides with low crystallinity, characterized by relatively weak diffraction peaks at 25, 33.69, 37.96° which correspond to the (006), (012), and (015) planes, respectively, and are consistent with the findings reported in previous studies [131, 134].

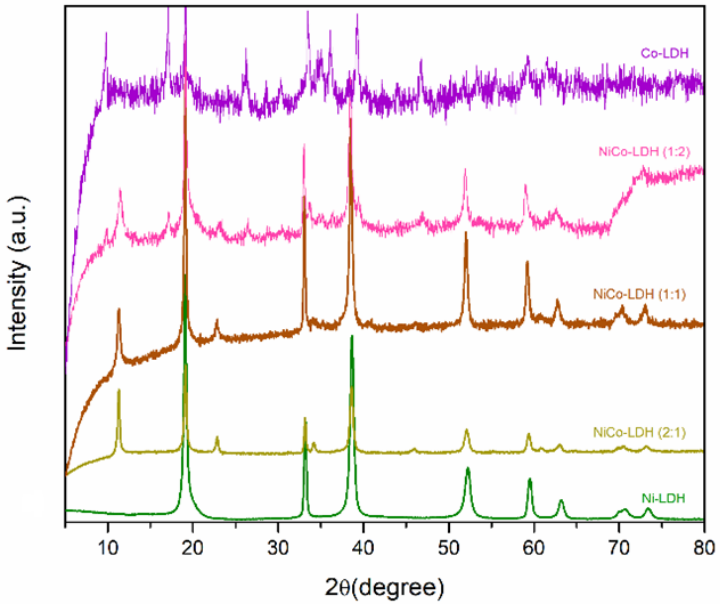

Figure 42. XRD pattern of NiCo-LDH with various ratios between Ni and Co: (1:0), (2:1), (1:1), (1:2), (0:1).

The NiCo-LDH exhibits two distinct phases, namely the α-phase and the β-phase. The β-phase is thermodynamic stable, and it is attributed to the hexagonal close-packed structure of M^{2+} ions (M = Ni, Co) and OH^- ions, which results in higher crystalline structure with an interlayer spacing of approximately 0.46 nm. On the other hand, the α-phase is composed of $M(OH)_2$ interlayers (M = Ni, Co) with low crystallinity and an interlayer spacing ranging from 0.75 to 0.81 nm [135]. Hence, the XRD results reveal that the Co-LDH, as it is originally prepared,

possesses a crystalline structure of α-phase $Co(OH)_2$, whereas the pure Ni-LDH exhibits a crystalline structure of β-phase $Ni(OH)_2$.

4.2.3 IR spectroscopy results

The identification of functional groups present in the synthesized LDH samples was conducted through the utilization of Fourier transform infrared (FT-IR) spectroscopy. The FT-IR spectra of the NiCo-LDH samples, which had varying mass ratios of Ni^{2+} and Co^{2+}, within the range of 500 to 4000 cm^{-1}, were depicted in Figure 43. It is worth noting that the sharp peak centered at 3626 cm^{-1} within the spectra originates from free -OH groups of the typical β-phase hydroxides [136]. Additionally, the bands located at 3525 and 1630 cm^{-1} can be attributed to the O–H stretching vibration and bending modes of the interlayer water and hydroxyl group, respectively [137, 138]. Furthermore, another band situated around 1383 cm^{-1} is linked to the vibration of interlayer CO_3^{2-} and NO_3^- anions. In general, CO_3^{2-} participated to form the carbonate hydroxide hydrate with Ni^{2+} and Co^{2+} ions via coordinate bonds, while NO_3^- was retained in the interlayer of LDH which can be attributed to the high solubility of NO_3^- in comparison to the CO_3^{2-}[131]. Finally, the peaks observed within the range of 500 to 700 cm^{-1} correspond to metal-oxide, oxo-metal-oxo, metal-oxo-metal bonds, and bending vibrations [139].

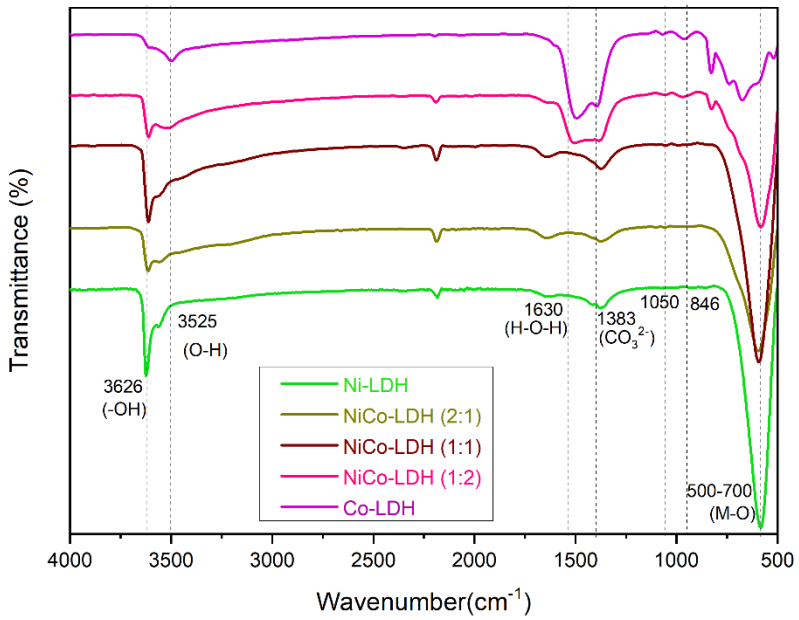

Figure 43. FT-IR spectra of NiCo-LDH with various ratios between Ni and Co: (1:0), (2:1), (1:1), (1:2), (0:1).

Apparently, there is remarkable difference in FT-IR peaks of β-$Ni(OH)_2$ and α-$Co(OH)_2$. A typically broad O–H stretching vibration band at around 3525 cm^{-1} in the spectra corresponds to interlayer water molecules that are hydrogen-bonded to Co–OH groups. For the as-prepared α-$Co(OH)_2$, four absorption bands located at 846, 1050, 1383, and 1630 cm^{-1} are attributed to the characteristic absorption peaks of carbonate ions, as reported previously [140, 141]. It is hard to eliminate the presence of carbonate anions due to the high affinity between CO_3^{2-} and Co–OH host layers [141]. In the FT-IR spectrum of the β-$Ni(OH)_2$ sample, in contrast, the absorption bands around 3525 and 1630 cm^{-1} were not observed, suggesting the absence of interlayer water molecules. The intense and sharp band at 3626 cm^{-1} is attributed to the O-H stretching mode, which is characteristic of free OH groups in brucite-like structures; the broad absorption at low-frequency region (400-600 cm^{-1}) is ascribed to Ni-O stretching and Ni-OH bending vibrations in the brucite-like octahedral sheet [140].

4.2.4 XPS results

X-ray photoelectron spectroscopy (XPS) measurements were employed to analyse the element composition of as-prepared NiCo-LDH. The X-ray photoelectron spectroscopy (XPS) results of (1:2) ratio between the Ni and Co precursors, which functions as the most effective catalyst in our system due to its photoelectrochemical (PEC) performances (see section 4.3.4), are displayed in the following. The high-resolution Ni 2p spectrum presents the individual peaks of Ni $2p_{3/2}$ and Ni $2p_{1/2}$ at the binding energy of 855.4 eV and 873.5 eV, accompanied with two main satellites peaks at 861.9, and 880.1 eV which demonstrate that the oxidation state of Ni is 2+ (Figure 44a) [142, 143]. The Co 2p core-level spectrum displays the two major peaks around 781.6 eV and 797.0 eV which are in accordance with Co $2p_{3/2}$ and Co $2p_{1/2}$, along with two principal shakeup satellite peaks at 803.2 and 786.8 eV, which are an indicative of a high-spin Co^{2+} in as-prepared NiCo-LDH (Figure 44b) [144, 145]. The O1s region can be deconvoluted into two peaks at 531.1 and 532.4 eV, which confirmed the presence of hydroxyl groups (M–OH) and oxygen bonds of H_2O (H–O–H), respectively (Figure 44c) [146].

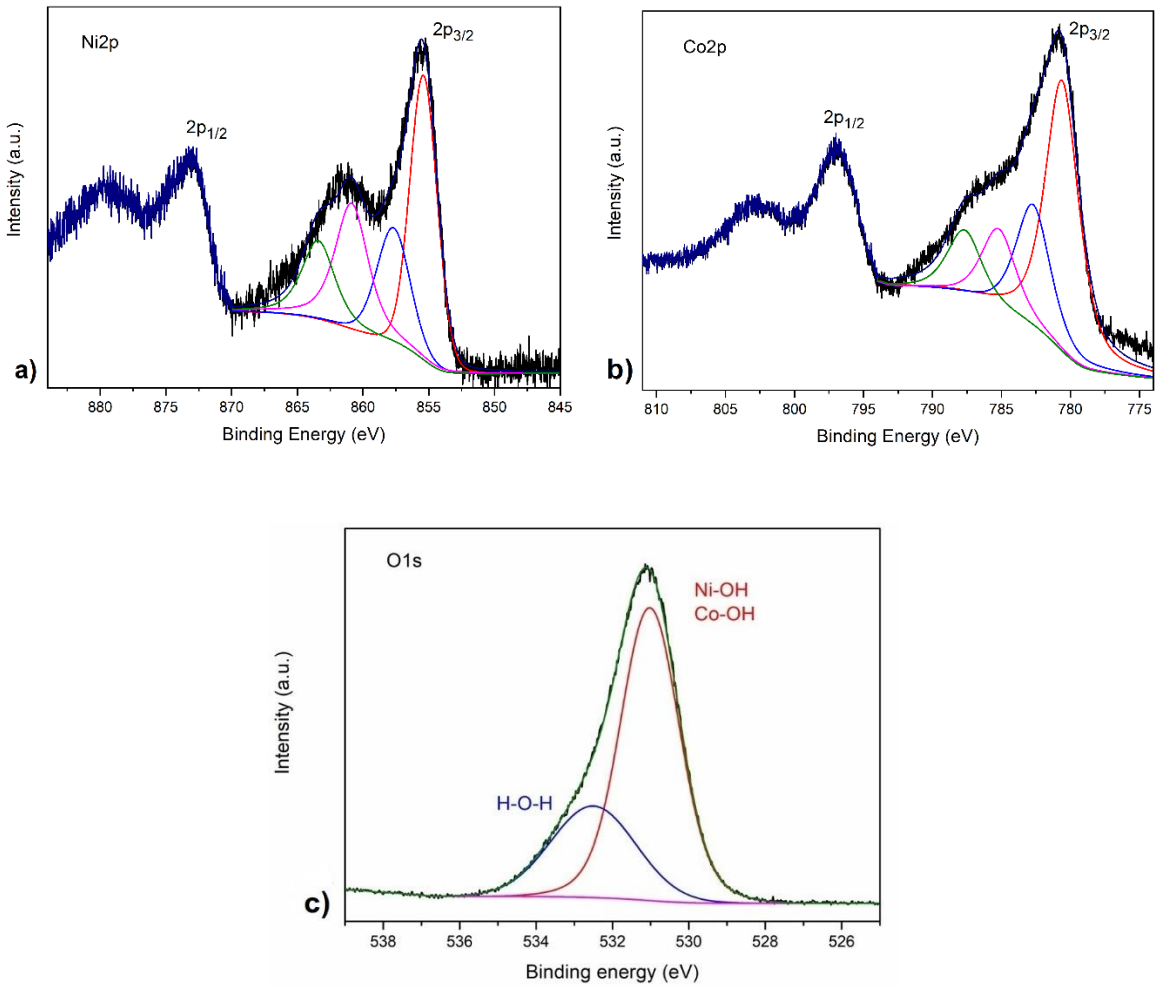

Figure 44. High resolution a) Ni 2p, b) Co 2p, and c) O 1s XPS spectra of NiCo-LDH.

The XP spectrum of other ratios between Ni and Co precursors; (Ni:Co)(1:1) and (Ni:Co)(2:1), and the quantity of elements are presented subsequently. The output of XPS measurements revealed that the oxidation state for both Ni and Co in other combined samples is 2+. From table 2, it can be seen that the atomic proportion between Ni and Co in the different catalyst contents are in agreement with the synthesis procedure.

Table 2. XPS atomic percentage results

Element	(Ni:Co)(1:2)	(Ni:Co)(1:1)	(Ni:Co)(2:1)
O	73.52	72.86	71.83
Ni	9.48	13.75	19.5
Co	17	13.39	8.67
Total	100.00	100.00	100.00

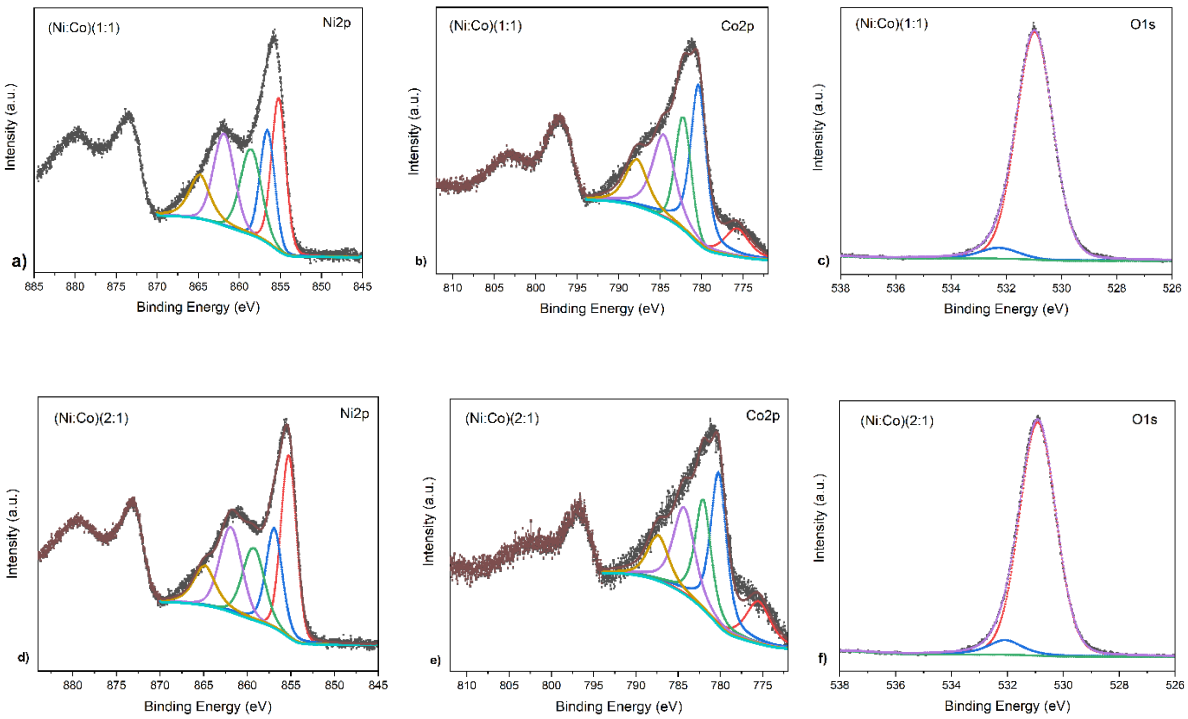

Figure 45. High resolution XPS spectra of NiCo-LDH catalyst with various ratio between precursors a) Ni 2p (Ni:Co)(1:1), b) Co2p (Ni:Co)(1:1), c) O1s (Ni:Co)(1:1), d) Ni2p (Ni:Co)(2:1), e) Co2p (Ni:Co)(2:1), and f) O1s (Ni:Co)(2:1).

4.3 Modified $CuWO_4/WO_3$ with optimum NiCo-LDH

4.3.1 SEM/EDX results

As revealed by the SEM images shown in Figure 46a,b, the deposited NiCo-LDH co-catalyst (Ni:Co)(1:2) (refer to section 4.3.4) formed islands rather than a layer over the $CuWO_4/WO_3$ 3D dandelion-like microstructures on the FTO substrate after the drop casting route. The composition of modified film with NiCo-LDH was further confirmed by the EDX mapping analysis (Figure 46), which clearly indicated the presence of all expected elements in the corresponding films, particularly cobalt and nickel as catalysts that were uniformly available within the LDH stacks.

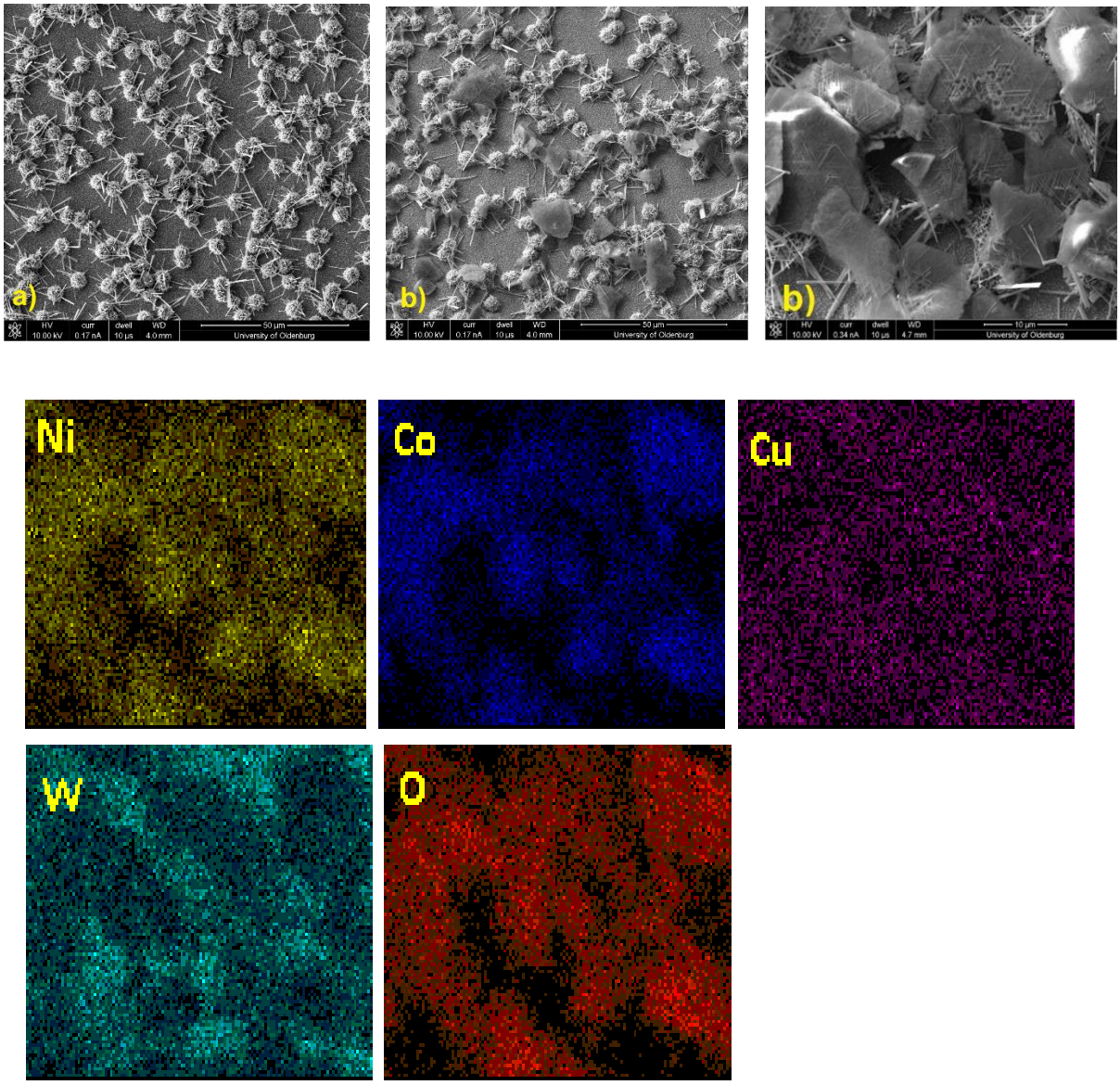

Figure 46. Top view SEM images of a) $CuWO_4/WO_3$ film, b) decorated $CuWO_4/WO_3$ film with NiCo-LDH (Ni:Co)(1:2) and corresponding element distribution mapping.

Table 3. Atomic percentage and elemental distribution.

Element	(XPS) At%	(EDX) At%
O	32.01	84.08
Co	26.16	5.28
Ni	13.34	2.95
Cu	4.83	1.35
W	23.66	6.78
Total	100.00	100.00

The XPS and EDX analyses validate that the atomic ratio of Ni to Co in the cocatalyst content is approximately 1:2, which is highly consistent with the intended loading values, table 3 (refer to section 4.3.4). These findings collectively demonstrate the successful formation of the $CuWO_4/WO_3$/NiCo-LDH composite.

4.3.2 GIXRD results

Figure 47, depicts the GIXRD pattern of $CuWO_4/WO_3$ and modified one with NiCo-LDH (Ni:Co)(1:2) catalyst (refer to section 4.3.4), at the incident angle of 0.5°. The noticeable change after deposition of LDH catalyst, is the intensity increasing of $CuWO_4/WO_3$ film's diffraction peaks around 2θ at 19, and 34° which are corresponding to the sharp and symmetrical diffraction peaks of NiCo-LDH catalyst, originating from β-$Ni(OH)_2$ phase in NiCo-LDH. Additionally, a new peak with 2θ value at 38.5° appears, referring to the (101) reflection of $Ni(OH)_2$. To clarify this, XRD patterns in the region of 37–40° were magnified and inserted in Figure 47. Importantly, no other impurity peak is observed, indicating that LDHs have been of pure phases and the crystal structure of $CuWO_4/WO_3$ remains unaltered by the deposition of LDHs.

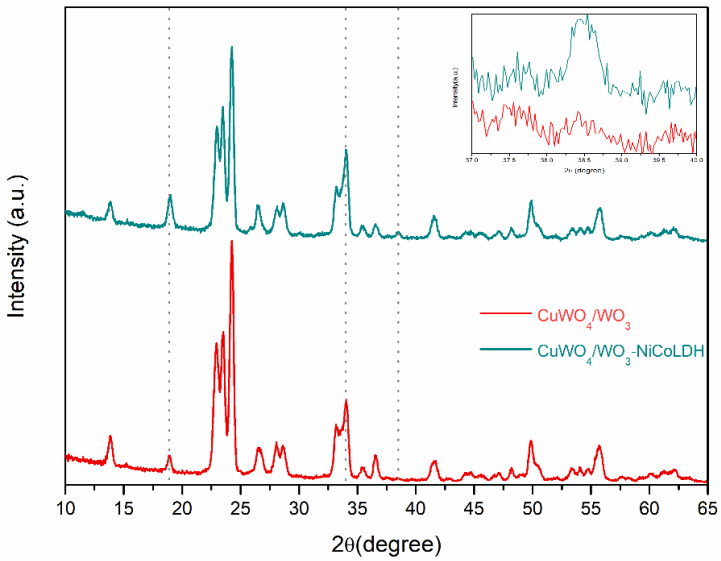

Figure 47. cof $CuWO_4/WO_3$ photoanode and modified one with NiCo-LDH; (Ni:Co)(1:2).

4.3.3 UV-Vis diffuse reflectance spectroscopy results

The optical characteristics of $CuWO_4/WO_3$ films that have been subjected to modification with NiCo-LDH were evaluated by means of UV-Vis diffuse reflectance absorption spectroscopy, as depicted in Figures 48 a,b. Evidently, the absorption edge of $CuWO_4/WO_3$ bare film is roughly 520 nm, while the Tauc formula calculated band gap is 2.30 eV [147]. Accordingly, a suitable cocatalyst should be as optically transparent as possible in the UV and visible-light regions [27]. The results show that the light absorbance of the modified film with NiCo-LDH is slightly greater than that of the $CuWO_4/WO_3$ film, the absorption edge and Tauc plot of the modified film indicate nearly identical values. This implies that loading a LDH has a negligible impact on both light absorption and the electronic states of $CuWO_4/WO_3$ photoanode. The observation testifies that synthesized NiCo-LDH with its weak light absorption capacity, is an ideal OER cocatalyst candidate [27, 53].

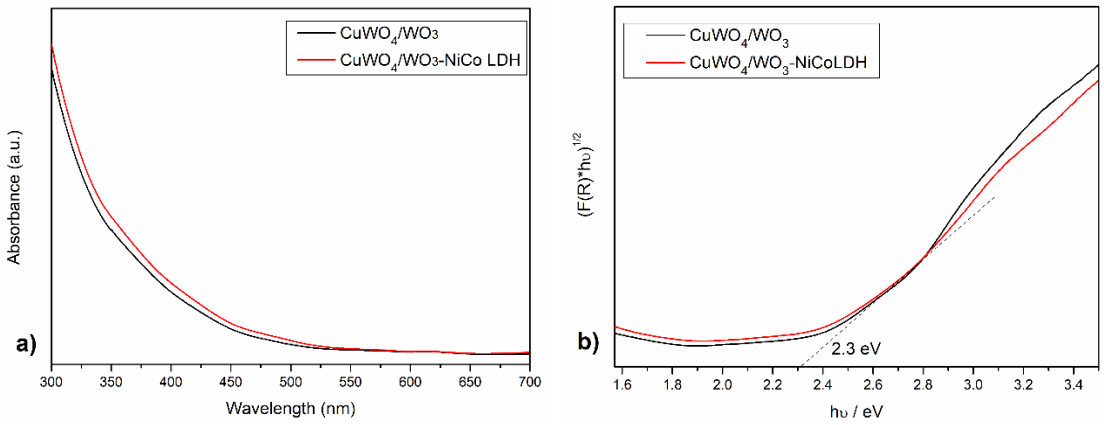

Figure 48. a) UV-Vis absorption spectrum, b) Tauc plot of $CuWO_4/WO_3$ photoanode and modified one with NiCo-LDH; (Ni:Co)(1:2).

4.3.4 Photoelectrochemical results

The effect of loading LDH catalyst on the photoelectroactivity of $CuWO_4/WO_3$ semiconductor were explored by a series of PEC measurements. All measurements were conducted in Na_2SO_4 0.1 M in phosphate buffer solution (PBS) pH=7. Considering the PEC performance of the modified $CuWO_4/WO_3$ photoanode with various ratio of NiCo-LDH Figure 49a, the highest activity was observed for NiCo-LDH with a ratio of (Ni:Co)(1:2). Based on the XRD findings (section 4.2.2), it can be observed that the NiCo-LDH catalyst is composed of α-$Co(OH)_2$ and

β-$Ni(OH)_2$ crystals. Taking into account that the higher proportion of Co exists in the mixture (Ni:Co)(1:2), the dominant phase is α-$Co(OH)_2$. The inherently and relatively wide interlayer spacing (≈ 0.75 - 0.81 nm) of the α-LDH nanostructures, in comparison to ≈ 0.46 nm of traditional metal hydroxides (especially β-phase hydroxides), will allow electrolyte ions and water molecules to get access to the active sites quickly and efficiently. Consequently, these interlayer regions can serve as reservoirs for ion buffering in the aqueous electrolyte, thereby accelerating the electrochemical reactions [136]. Subsequently, this LDH sample was selected as the optimal catalyst for our system and was used for further characterization of modified composite samples. The assessment of chopped light voltammetry (CLV) in Figure 49b reveals that, in comparison to the pure $CuWO_4/WO_3$ photoanode, the photocurrent density of the $CuWO_4/WO_3$/NiCo-LDH composite photoanode enhances with an increase in loading of co-catalysts. The use of 0.05 mg of NiCo-LDH (Ni:Co)(1:2) exhibits the highest improvement in photocurrent density.

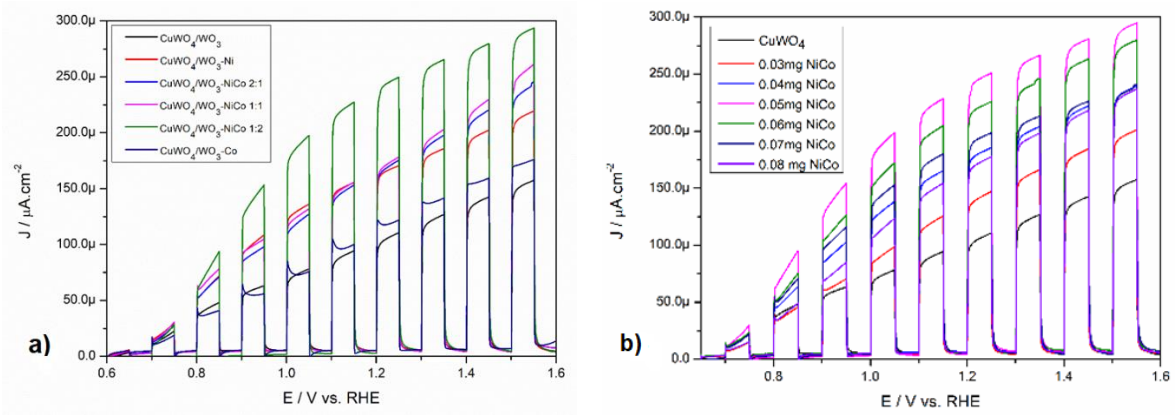

Figure 49. Chopped light linear sweep voltammogram of modified $CuWO_4/WO_3$ with 0.05 mg of a) various ratio between (Ni:Co), b) various loading amount, NiCo-LDH (Ni:Co)(1:2) under illumination measured in 0.1 M Na_2SO_4 (pH 7 PBS).

The findings of the study indicate that the photocurrent density of the modified $CuWO_4/WO_3$ photoanode is significantly higher than that of the pristine $CuWO_4/WO_3$ photoanode as demonstrated by the linear sweep voltammograms (LSV) (Figure 50a). At 1.23 V vs. RHE, the photocurrent density reaches 0.17 $mA \cdot cm^{-2}$, which is approximately twice the value of the pristine photoanode. The enhanced photocurrent density of $CuWO_4/WO_3$ electrodes is caused through the transfering of photogenerated holes from the valence states of irradiated $CuWO_4/WO_3$ to the NiCo-LDH catalysts, which could potentially oxidize the Ni^{2+}/Co^{2+} species into their high-valence state Ni^{3+}/Co^{3+}. Since at standard conditions (25 °C, pH 7), the redox potential for the Ni(III/II) and Co(III/II) has been reported to be 1.39 and 1.81 V *vs.*

RHE, respectively, the generated Ni^{3+}/Co^{3+} are capable of oxidizing the water molecules into O_2 since the water oxidation potential is 1.23 V *vs.* RHE [54, 148]. As a result, by utilizing an alternative pathway involving NiCo-LDH for photoinduced hole transfer, there is a notable reduction in interfacial charge recombination. This results in an improved efficiency in collecting holes and ultimately enhances the overall photoactivity [68, 149].

Since in our study, a low content of catalysts was loaded to the surface of the photoelectrode with a negligible impact on crystal structure (Figure 47) and light absorption (Figure 48), the increase in photocurrent activity can only be attributed to modifications in charge transfer and recombination rate [54]. To confirm this, electrochemical impedance spectroscopy (EIS) measurements were carried out to qualitatively assess the properties of charge transport between the electrodes and the electrolyte. The typical Nyquist plot shows a semicircle which represents the charge transfer resistance at the electrode/electrolyte interface [150]. Figure 50b. shows a semicircle of large diameter for the $CuWO_4/WO_3$ photoanode. Following the loading of the co-catalyst onto the surface of the photoanode, a decrease in the diameter of the semicircle was observed, providing clear evidence that electron transfer was facilitated in a presence of the catalyst.

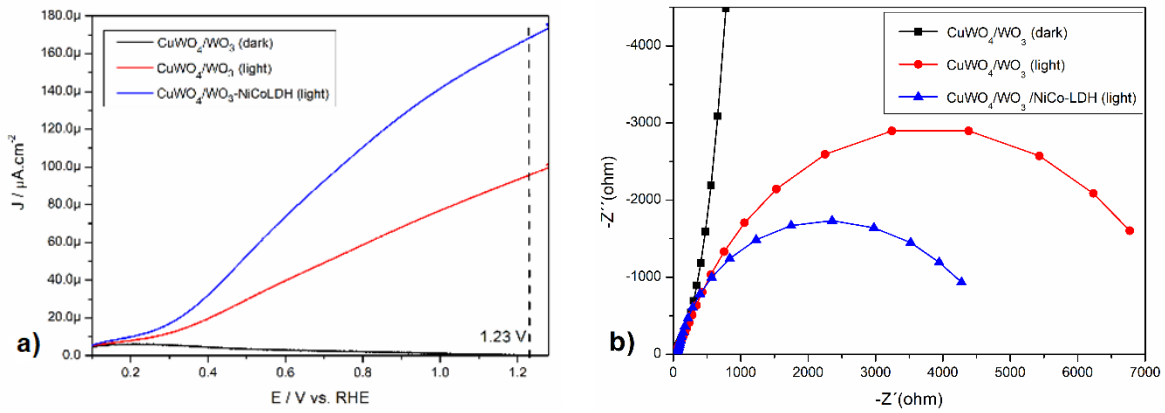

Figure 50. a) Linear sweep voltammogram, b) EIS Nyquist plot of $CuWO_4/WO_3$ photoanode and modified one with NiCo-LDH in 0.1 M Na_2SO_4 (pH 7 PBS).

Based on these results, the NiCo-LDH catalyst used in this study has the ability to promote the separation of photogenerated charge carriers through consuming holes that accumulate on the electrode surface and accelerating charge transfer.

In the following, a comparison of PEC performance of reported data in literature for $CuWO_4$ thin films for the oxygen evolution reaction (OER) is presented. As is evident, the recorded values for photocurrent density demonstrate a clear correlation with our research. Furthermore,

the observed increase in the J value following modification process in our work, exhibits a comparable trend to the data reported in previous literature. The augmented J_{ph}^{b} value of modified photoanode is approximately two times the original J_{ph}^{a} value.

Table 4. PEC performance for $CuWO_4$ thin films for the oxygen evolution reaction reported in the literature.

Synthesis method	Modified with	Electrolyte	$J_{ph}^{a,b}$ *(mA/cm^2) at 1.23 V vs. RHE	Ref.
Electrodeposition	__	0.1 M PBS pH=7	J_{ph}^{a} = 0.16	[29]
Spin coating	__	0.1 M PBS pH=7	J_{ph}^{a} = 0.15	[33]
Electrodeposition	Mo (doping)	0.1 M PBS pH=7	J_{ph}^{a} = 0.07 J_{ph}^{b} = 0.16	[151]
Spray pyrolysis	Fe (doping)	0.1 M PBS pH=7	J_{ph}^{a} = 0.19 J_{ph}^{b} = 0.30	[152]
Thermal solid-state reaction	Co-P_i	0.1 M PBS pH=7	J_{ph}^{a} = 0.34 J_{ph}^{b} = 0.42	[153]
HT/Drop casting	Ni-P_i	0.1 M PBS pH=7	J_{ph}^{a} = 0.3 J_{ph}^{b} = 0.5	[54]
Spray pyrolysis	Au	0.1 M PBS pH=7	J_{ph}^{a} = 0.03 J_{ph}^{b} = 0.1	[43]
Hydrothermal	H_2 treatment	0.1 M Na_2SO_4 solution (pH = 6.8)	J_{ph}^{a} = 0.03 J_{ph}^{b} = 0.19	[48]
Hydrothermal	NiCo-LDH	0.1 M Na_2SO_4 PBS solution (pH = 7)	J_{ph}^{a} = 0.1 J_{ph}^{b} = 0.17	This work

*J_{ph} represents the photocurrent density. PBS represents phosphate buffer solution. HT represents hydrothermal. J_{ph}^{a} is assigned to the J value of pristine $CuWO_4$, and J_{ph}^{b} is assigned to the J value of the modified $CuWO_4$ photoanode.

The incident photons to current efficiency (IPCE) and absorbed photons to current efficiency (APCE) were evaluated via measurements taken at varying wavelengths at an applied bias of 1.23 V versus RHE, in order to assess the photoanode's conversion efficiency (refer to section 4.3.4). With the implementation of the NiCo-LDH catalyst in the modified photoanode, both IPCE and APCE values were amplified. These findings demonstrate that the NiCo-LDH effectively captures holes and leads to enhanced electron flow to the FTO back contact, ultimately resulting in higher photocurrent (Figure 51a,b). The outcomes of the applied bias photon to current efficiency (ABPE) reveal that the NiCo-LDH catalyst is notably efficacious

in segregating charge carriers and enhancing the photoelectrochemical (PEC) capability of $CuWO_4/WO_3$ photoelectrodes in the absence of a hole scavenger (Figure 51c). It has been suggested that the negative shift of the flat band potential could lead to an increase in the band bending of the photoanodes, consequently enhancing the process of interfacial transfer [154]. Due to this reason, the flat band potentials (E_{fb}) of the original photoelectrodes and the ones modified with LDH were investigated using the Mott-Schottky relationship.

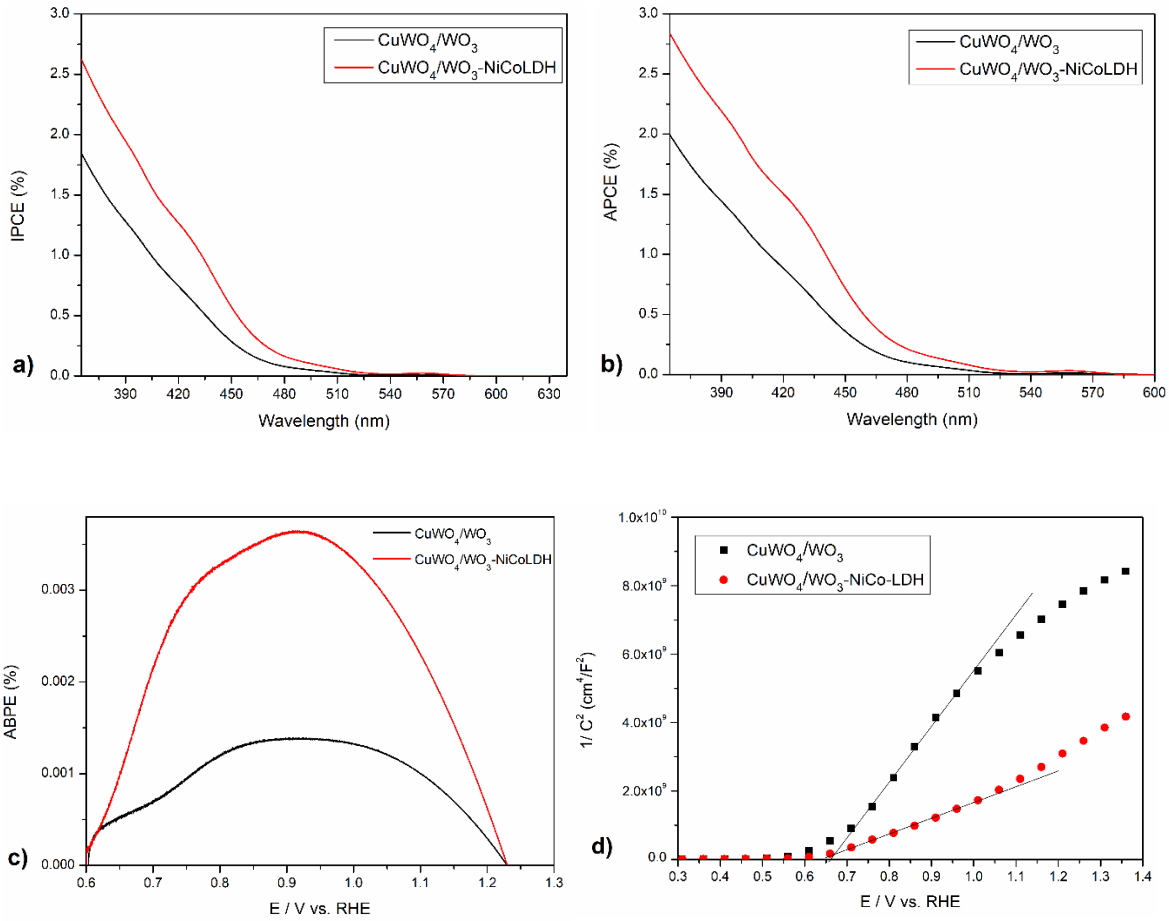

Figure 51. a) IPCE, b) APCE, c) ABPE, and d) Mott- Schottky plots of $CuWO_4/WO_3$ photoanode and modified one with NiCo-LDH.

By extrapolating the X-intercepts of the linear region within Mott-Schottky plots, the determination of E_{fb} can be made based on the intercept on the E axis, as exemplified in Figure 51d. The V_{fb} of the pristine $CuWO_4/WO_3$ film was found to be approximately 0.65 V vs. RHE. Conversely, for the modified $CuWO_4/WO_3$ film with NiCo-LDH, there was not a noticeable change in V_{fb}, implying that the loading of catalyst onto the photoanode does not alter the position of the energy band of the composite. This suggests that the enhancement in the rate of hole transfer is not attributed to the alteration in the flat band potential. Both films demonstrated

linear dependence with a positive slope ranging from 0.3 to 1.4 V vs. RHE, which represents a typical feature of an n-type semiconductor [40].

4.3.5 Charge separation and charge injection efficiencies

In addition to exploring the J-V characteristics of water oxidation/reduction, the evaluation of the photoelectrode's performance in terms of charge separation efficiencies and interfacial charge injection is often achieved through J-V measurements using hole and electron acceptors that possess fast interfacial charge transfer kinetics. One viable approach involves introducing scavengers into the aqueous electrolyte. For this investigation, we utilized Na_2SO_3, a well-known hole scavenger that exhibits the ability to rapidly consume photogenerated holes and oxidize itself to Na_2SO_4 [117, 153]. Therefore, the PEC performance of modified $CuWO_4/WO_3$ with NiCo-LDH was also examined in the presence of 0.5 M Na_2SO_3 which is served as a hole scavenger. As can be seen in Figure 52a, the water oxidation photocurrent density (J_{PEC}) of $CuWO_4/WO_3$/NiCo-LDH is lower than that of sulfite oxidation photocurrent density ($J_{sulfite}$), demonstrating that recombination at the electrode/electrolyte interface was the primary cause of the loss of surface-reaching holes. To quantify the contribution of NiCo-LDH in improvement of surface charge transfer, namely the surface water oxidation reaction kinetics, the charge injection yield ($\eta_{injection}$), which is the yield of holes that have reached the electrode/electrolyte interface and that are injected into the electrolyte to oxidize the water, was computed using equation:

$$\eta_{injection} = \frac{J_{PEC}}{J_{sulfite}} \tag{28}$$

where J_{PEC} is the water oxidation photocurrent density in 0.1 M Na_2SO_4 (pH=7 PBS) and $J_{sulfite}$ is the photocurrent density in the presence of the hole scavenger (0.5 M Na_2SO_3) in the PBS electrolyte. The charge separation efficiency ($\eta_{separation}$) on the surface of $CuWO_4/WO_3$/NiCo-LDH photoanode can be obtained by dividing the photocurrent measured in the electrolyte containing Na_2SO_3 as a hole traper by the maximum theoretical photocurrentcurrent (J_{abs}) (Eq. 29).

$$\eta_{separation} = \frac{J_{sulfite}}{J_{abs}} \quad (29)$$

Figures 52b and c show the calculated η_{inj} and η_{sep} curves for the photoanodes versus the applied potential. At 1.23 V vs. RHE, the η_{inj} for $CuWO_4/WO_3$/NiCo-LDH reached approximately 82%, which is almost three-fold higher than that of the $CuWO_4/WO_3$ photoanode (29%). It demonstrated that the NiCo-LDH played a key role in accelerating the surface reaction by efficiently and quickly consuming photogenerated holes. Accordingly, the obtained η_{sep} indicated higher amount for $CuWO_4/WO_3$/NiCo-LDH photoelectrodes than that pristine $CuWO_4/WO_3$ one, which concluded the better charge separation efficiency of modified samples with NiCo-LDH catalyst in the bulk. These findings indicate that loading NiCo-LDH catalyst can significantly improve the separation and transfer of the photogenerated charge.

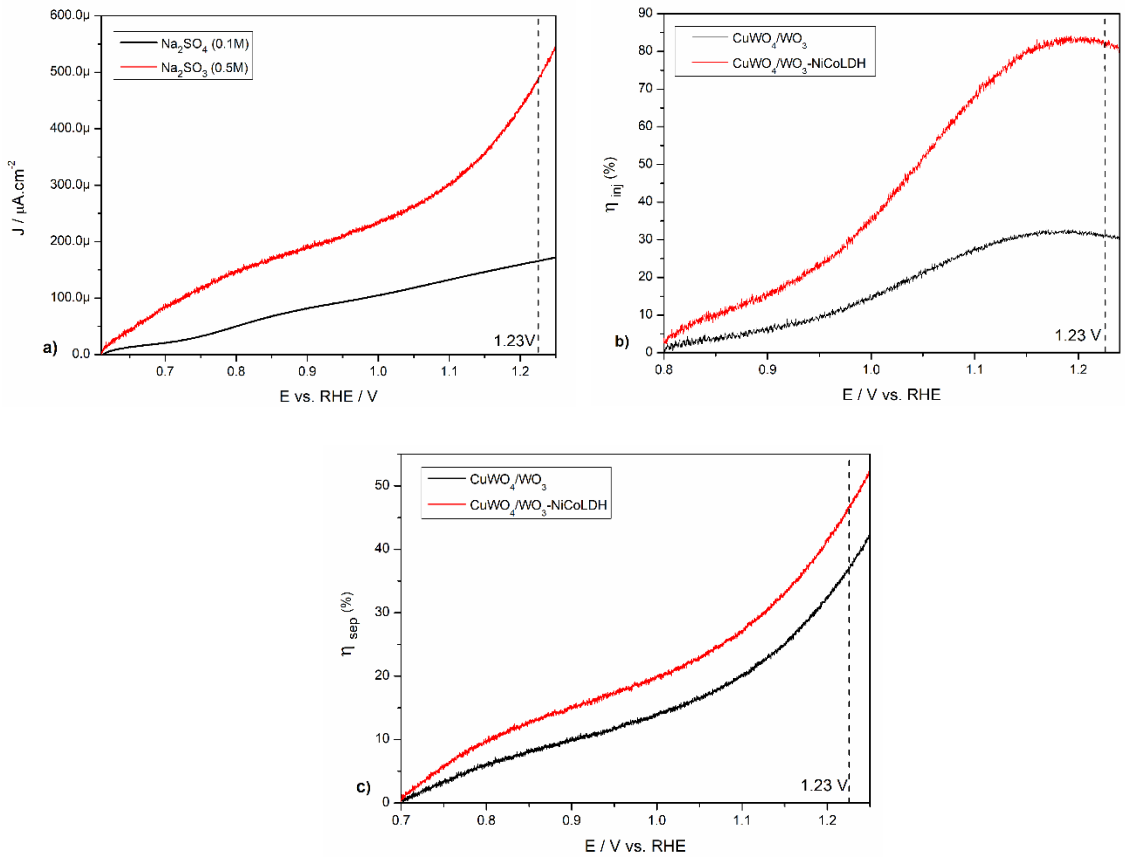

Figure 52. J−V curve of $CuWO_4/WO_3$/NiCo-LDH photoanode for a) water oxidation (without 0.5 M Na_2SO_3) and sulfite oxidation, b) charge injection efficiency, and c) charge separation efficiency of $CuWO_4/WO_3$ and photoanode and modified one with NiCo-LDH.

4.3.6 Stability test

The stability is another important property to assess the performance of photoanode material during solar water splitting. The measurement was conducted using chronoamperometry method at applied potential of 1.23 V vs. RHE under chopped illumination at 100 mW/cm^2 intensity for 2 hours. From transient photocurrent curves of as obtained photoanodes shown in Figure 53, it can be observed that when the light is turned on and off, the photocurrent density of all photoanodes rises and falls rapidly which indicates the current response resulting from visible light illumination.

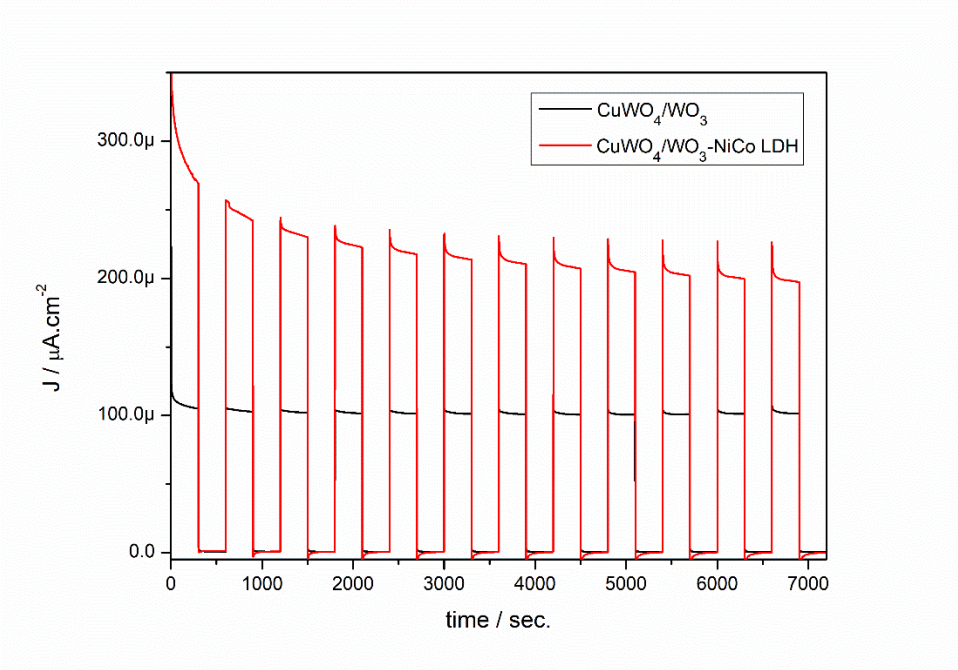

Figure 53. Chronoamperometry (i–t) curve of $CuWO_4/WO_3$ photoanode and modified one with NiCo-LDH collected at 0.6 V vs. RHE under chopped illumination in 0.1 M Na_2SO_4 (pH 7 PBS).

The corresponding transient chronoamperometric analysis demonstrates that in the constant potential measurements, the functionalized $CuWO_4/WO_3$ photoanode exhibits superior PEC activity compared to bare $CuWO_4/WO_3$ photoanode, which is consistent with the results of linear potential sweep measurements. The photocurrent density of the modified $CuWO_4/WO_3$ photoanode is above 0.2 mA·cm^{-2} after 2 h measurement which is twice as large as of pristine photoanode. The responsive photocurrent density of pristine $CuWO_4/WO_3$ remains almost constant at about 0.1 mA·cm^{-2} during 2 h measurement. The modified $CuWO_4/WO_3$ photoanode show an acceptable stability though it was not as stable as the untreated $CuWO_4/WO_3$ photoanode. Figure 53 clearly shows that the photocurrent density of LDH-

modified $CuWO_4/WO_3$ was initially above 0.25 $mA \cdot cm^{-2}$ and decreased to 80% of its original value after 2 h of the reaction. The main reason of a such observed photocurrent loss can be assigned to loading method of co-catalyst onto the surface of photoanode. The implemented method for loading of co-catalyst was drop-casting route which can lead to unproper contact of catalysts and primary substrate result in unstable performance during long-term irradiation. In transient amperometry photocurrent plot, the sharper transient spikes were visible for modified $CuWO_4/WO_3$ photoanode during each on-off cycle, indicated the the accumulation of photogenerated holes at the electrode surface. This phenomenon can be referring to the not robust contact of active catalyst on fixed substrate which prevent the efficient separation of photogenerated electron-hole pairs.

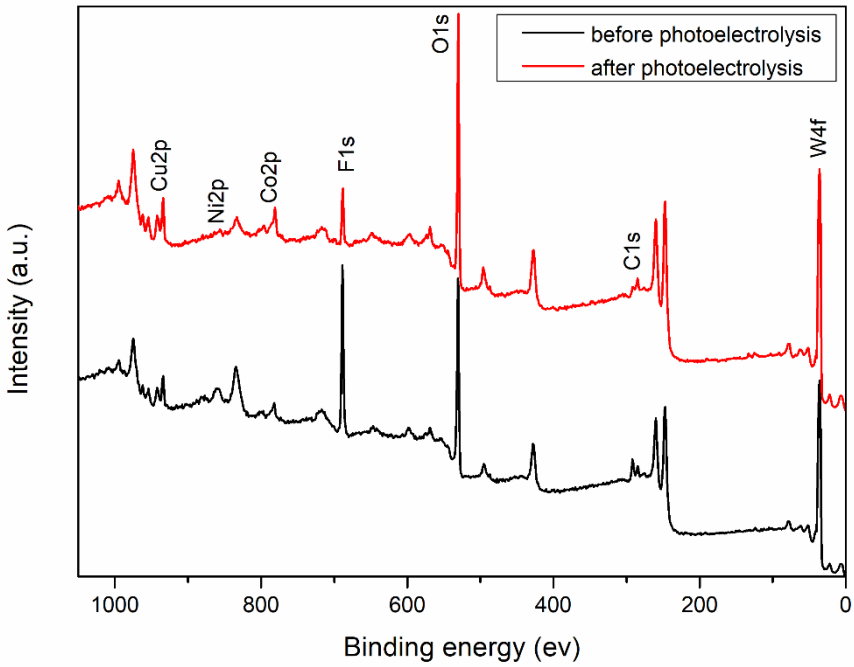

Figure 54. Survey XPS spectrum of $CuWO_4/WO_3$/NiCo-LDH photoanode before and after chronoamperometry measurements for 2h.

The X-ray photoelectron spectroscopy (XPS) survey spectrum of a modified $CuWO_4/WO_3$ thin film is presented in Figure 54. The peaks attributed to both W and Cu elements before and after the photoelectrolysis exhibit identical behavior, thus confirming the outcome of the stability test. On the other hand, the intensity of Ni and Co elements was found to be reduced. Similarly, the intensity of F, which is indicative of the Nafion-based solution utilized for catalyst deposition on the substrate, was also decreased. This experiment serves to confirm the instability of the drop-casting method for loading of catalysts onto photoanode for long-term

PEC studies. To prolong the system's lifespan, it may be beneficial to explore alternative methods of modification, such as electrodeposition technique.

4.3.7 Possible Mechanism

The schematic illustration of $CuWO_4/WO_3$/NiCo-LDH photoanode combined with a Pt counter electrode for the PEC water oxidation mechanism is shown in Figure 55. Upon being exposed to visible light, the valence band electrons were excited to the conduction band, thus creating electron-hole pairs. The electrons subsequently moved to the Pt counter electrode via an external circuit, where they became involved in the water possible reduction reaction. The holes then migrated to NiCo-LDH, which caused the low-valence M^{2+}(Ni^{2+}/Co^{2+}) to oxidize into the high-valence state of M^{3+} (Ni^{3+}/Co^{3+}) because of a lower energy barrier. This high-valent metal ion serves as the actual active site, enabling the oxidation of water to oxygen and then reducing it to its original valence state of M^{2+}. As a result, the LDH cocatalyst enhances electron transfer and promotes charge separation by completing this cyclic process, which leads to the acceleration of OER kinetics and the improvement of the PEC properties for water splitting [155, 156].

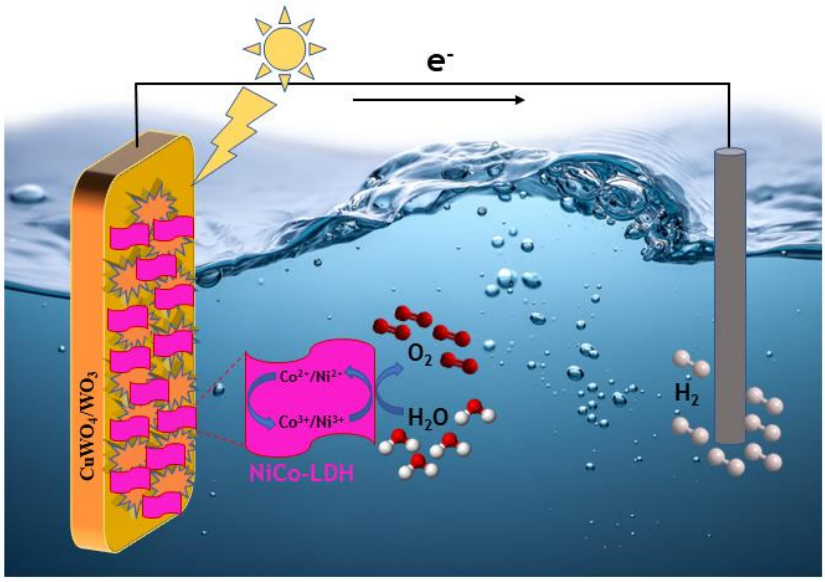

Figure 55. Mechanism diagram of PEC water oxidation on $CuWO_4/WO_3$/NiCo-LDH photoanode.

5 General Conclusion

In this study, the direct deposition of dandelion-like $CuWO_4/WO_3$ heterojunction microarray onto the FTO substrate was utilized. This approach combines the advantageous features of solution chemistry, such as precise control and adaptability, with the simplicity, non-toxicity, and cost-effectiveness of aqueous precursors in the technology for processing thin solid films. Furthermore, the utilization of metal salt precursors and aqueous solutions presents considerable benefits. Apart from the evident environmentally friendly aspect, the purity of the material is significantly enhanced due to the absence of organic compounds or solvents in the process.

The synthesized thin film was investigated with respect to the effect of various precursor ratios. The results indicated that the most favorable photoelectrochemical performance was achieved with a (1:1) (Cu:W) ratio. This variation in photoelectrochemical activity can be attributed to the significant alteration in the morphology of the composite microarray, which was influenced by the stoichiometry effects. The highest level of activity was observed when the dandelion-like microstructure of the $CuWO_4/WO_3$ composite was evenly distributed across the substrate, providing suitable active sites for surface reactions. It is important to note that there existed an optimal degree of this distribution, and any deviation from this optimal level resulted in decreased activity. This optimal distribution suggests that the microspheres are not densely aggregated on the surface, covering it entirely. Likewise, they are not randomly scattered with significant gaps between them. Conversely, the superior 3D dandelion-like arrays on the surface of the photoanode could facilitate efficient separation of charge carriers.

Furthermore, a systematic investigation into the influence of various synthesis parameters, including temperature, duration, and concentration, on the prepared samples demonstrated a significant impact on both the phase composition and morphology of the resulting materials. The photoelectrochemical analyses revealed that the dandelion-like $CuWO_4/WO_3$ microstructures, synthesized using precursors at a concentration of 2 mM and subjected to a temperature of 180 °C for a duration of 8 hours, exhibited the most pronounced photoelectrochemical activity. This particular sample displayed a homogeneous distribution of microspheres on the substrate, characterized by neither complete coverage of the surface nor randomly scattered microspheres. This distribution facilitated the provision of an appropriate

quantity of accessible active sites on the surface, conducive to the facilitation of photoelectrochemical reactions at the electrode/electrolyte interface.

The growth mechanism underlying the formation of the dandelion-like structure can be delineated as follows: during the initial phase of the hydrothermal reaction, under specific conditions of a particular supersaturation ratio and reduced interfacial tension, nucleation occurred on the FTO substrate. The nuclei primarily consisted of the $CuWO_4$ phase, with an additional presence of excess W ion. Subsequently, the growth of $CuWO_4$ crystals proceeded from these nuclei. Given the initially thermodynamically unstable boundaries and grains of the crystals, crystallization tended to progress in the most favorable direction to minimize energy. With increasing reaction time, the surplus W precursor in the solution led to the formation of spherical structures. This, in turn, contributed to surface reconstruction and the development of a dandelion-like structure. Consequently, this in-situ deposition method resulted in a higher concentration of W compared to Cu on the uppermost layer of the thin film.

The examination via Grazing Incidence X-ray Diffraction (GIXRD) and Raman spectroscopy corroborated the presence of two distinct phases on the FTO surface. GIXRD analysis revealed that at a low incident angle of 0.5°, the diffraction peaks corresponding to the monoclinic WO_3 phase were predominant. However, upon increasing the angle from 0.5° to 2°, the diffraction pattern indicated the presence of the triclinic $CuWO_4$ structure. This observation suggests that during the initial stages of film growth, the surface was primarily deposited with $CuWO_4$, followed by the gradual accumulation of WO_3 on the $CuWO_4$ layer during further film growth. Consequently, dandelion-like $CuWO_4/WO_3$ microstructures formed, enveloping the FTO surface. Further confirmation of the composite structure was provided by Raman analysis, which revealed the presence of a dense, homogeneous layer of $CuWO_4$ on the FTO surface, along with the presence of dandelion-like microspheres of WO_3 on this dense surface.

Further improvement of photoactivity of $CuWO_4/WO_3$ photoanode was examined by integrating NiCo-LDH co-catalysts into the system for the first time. The NiCo-LDH catalyst was synthesized via the hydrothermal method utilizing various precursor ratios. XPS measurements revealed that the oxidation state of Ni and Co in all synthesized samples was +2, consistent with the findings from XRD analysis. The XRD results indicated that the synthesized NiCo-LDH possessed a crystalline structure comprising a mixture of α-phase Co $(OH)_2$ and β-phase Ni $(OH)_2$. In terms of the photoelectrochemical (PEC) performance of the modified $CuWO_4/WO_3$ photoanode with different ratios of NiCo-LDH, the highest activity was

observed for NiCo-LDH with a (Ni:Co)(1:2). It is noteworthy that in samples with a higher proportion of Co in the mixture, the dominant phase is α-$Co(OH)_2$. The relatively wider interlayer spacing inherent to the α-LDH nanostructures (approximately 0.75 - 0.81 nm), compared to traditional metal hydroxides (especially β-phase hydroxides with an interlayer spacing of approximately 0.46 nm), allows for enhanced accessibility of electrolyte ions and water molecules to the active sites. Consequently, these interlayer regions could function as reservoirs for ion buffering in the aqueous electrolyte, facilitating accelerated electrochemical reactions.

The $CuWO_4/WO_3$ photoanode adorned with the optimized NiCo-LDH exhibits a photocurrent density of 0.17 $mA \cdot cm^{-2}$ at 1.23 V vs. RHE, a value twice as large as that of the pristine photoanode. The heightened photocurrent density observed in $CuWO_4/WO_3$ electrodes can be attributed to the accelerated oxidation kinetics of both Ni^{2+} and Co^{2+} ions by photogenerated holes, which outpaces direct H_2O oxidation. Consequently, the holes are promptly transferred with the assistance of NiCo-LDH, effectively suppressing electron-hole recombination. The generated Co^{3+} and Ni^{3+} species exhibit notable activity towards the oxygen evolution reaction (OER) owing to their favorable oxidation potentials. Importantly, these species undergo reduction back to Co^{2+} and Ni^{2+} as the OER progresses, establishing an oxidation-reduction cycle that ensures a sustained enhancement effect in photoactivity mediated by NiCo-LDH.
To evaluate the conversion efficiency of the modified photoanode, measurements of IPCE, APCE, and ABPE were performed. The findings revealed that the incorporation of the catalyst led to enhancements in all efficiency parameters. This outcome underscores the notable efficacy of the NiCo-LDH catalyst in facilitating the segregation of charge carriers. Furthermore, PEC measurements were conducted in the presence of Na_2SO_3, which acted as a suitable hole scavenger to assess the photoelectrode's efficacy in terms of charge separation efficiencies and interfacial charge injection. This resulted in enhanced photocurrent generation as compared to water oxidation. Through these measurements, we were able to elucidate the role that NiCo-LDH plays in the charge separation efficiency within the bulk, as well as in the charge injection efficiency at the photoanode surface.

In summary, the exemplary PEC performance of modified photoanodes highlights the crucial function of NiCo-LDH in promoting reactant and product diffusion, accelerating charge transfer, facilitating effective separation of photogenerated charge carriers, and expediting the consumption of accumulated holes on the electrode surface.

6 Outlook

To tackle the most significant global challenge of seeking out clean, secure, and sustainable energy resources, one potential avenue involves harnessing the visible energy emitted by sunlight. Within this particular approach, the primary objective of this research endeavors has been focused on utilizing tungsten-based photoanodes that possess a narrow band gap, rendering them active within the visible range of solar radiation. The $CuWO_4/WO_3$ photoanode that was fabricated demonstrated a band gap of 2.6 eV, thus exhibiting promising characteristics as a photoanode material suitable for the visible light spectrum. Nonetheless, there remains untapped potential to expand research efforts towards capturing a greater proportion of sunlight by employing semiconductors with an even lower band gap. Among these innovative tungsten-based compounds lies the α-$SnWO_4$ photoelectrode, which boasts a band gap of approximately 1.9 eV. To go deeper into this realm, further investigation may be conducted through the development of heterostructures comprising α-$SnWO_4$ photoanodes.

The facile hydrothermal synthesis method was employed in this study to fabricate the 3D dandelion-like $CuWO_4/WO_3$ photoanode. Numerous alternative techniques exist to produce tungsten-based photoanodes, with variations in dimensions and morphology of products. Thus, it is important to explore other fabrication methods such as electrodeposition and spray pyrolysis.

To the best of our knowledge, this study is the first to investigate the enhancement of the photoelectrochemical activity of the $CuWO_4$ photoanode through the utilization of layered double hydroxide (LDH) co-catalysts in a neutral electrolyte. In this preliminary investigation, the binary NiCo-LDH was examined as a co-catalyst for the system. Nevertheless, it is possible to develop other types of ternary and quaternary LDHs as novel oxygen evolution cocatalysts to improve the performance of solar-to-chemical energy conversion.

In view of the stability test measurements, it is evident that the modified photoanode did not exhibit substantial activity over extended periods of illumination. To enhance the longevity of the system, alternative techniques for modification, such as in-situ hydrothermal reaction and electrodeposition, could be subject to investigation.

7 References

[1] M. Grätzel, Photoelectrochemical cells, Nature, 414 (2001) 338-344.

[2] Bequerel, E. Recherches sur les effets de la radiation chimique de la lumière solaire, au moyen descourants électriques. C.R. Acad. Sci. 9 (1839) 145–149.

[3] C.V. Reddy, K.R. Reddy, N.P. Shetti, J. Shim, T.M. Aminabhavi, D.D. Dionysiou, Hetero-nanostructured metal oxide-based hybrid photocatalysts for enhanced photoelectrochemical water splitting – A review, Int J Hydrogen Energ, 45 (2020) 18331-18347.

[4] J. Joy, J. Mathew, S.C. George, Nanomaterials for photoelectrochemical water splitting – review, Int J Hydrogen Energ, 43 (2018) 4804-4817.

[5] Y. Shabdan, A. Markhabayeva, N. Bakranov, N. Nuraje, Photoactive Tungsten-Oxide Nanomaterials for Water-Splitting, Nanomaterials, 2020.

[6] A. Cecal, A.O. Paraschivescu, K. Popa, D. Colisnic, G.A. Timco, L. Singenerean, Radiolytic splitting of water molecules in the presence of some supramolecular compounds, Journal of The Serbian Chemical Society, 68 (2003) 593-598.

[7] Y. Bu, J.-P. Ao, A review on photoelectrochemical cathodic protection semiconductor thin films for metals, Green Energy & Environment, 2 (2017) 331-362.

[8] K. Maeda, K. Domen, Photocatalytic Water Splitting: Recent Progress and Future Challenges, The Journal of Physical Chemistry Letters, 1 (2010) 2655-2661.

[9] I. Akkerman, M. Janssen, J. Rocha, R.H. Wijffels, Photobiological hydrogen production: photochemical efficiency and bioreactor design, Int J Hydrogen Energ, 27 (2002) 1195-1208.

[10] J. Lédé, F. Lapicque, J. Villermaux, Production of hydrogen by direct thermal decomposition of water, Int J Hydrogen Energ, 8 (1983) 675-679.

[11] C. Ros, T. Andreu, J.R. Morante, Photoelectrochemical water splitting: a road from stable metal oxides to protected thin film solar cells, Journal of Materials Chemistry A, 8 (2020) 10625-10669.

[12] A. Fujishima, K. Honda, Electrochemical Photolysis of Water at a Semiconductor Electrode, Nature, 238 (1972) 37-38.

[13] T. Hisatomi, J. Kubota, K. Domen, Recent advances in semiconductors for photocatalytic and photoelectrochemical water splitting, Chemical Society Reviews, 43 (2014) 7520-7535.

[14] S. Kment, F. Riboni, S. Pausova, L. Wang, L. Wang, H. Han, Z. Hubicka, J. Krysa, P. Schmuki, R. Zboril, Photoanodes based on TiO_2 and α-Fe_2O_3 for solar water splitting – superior role of 1D nanoarchitectures and of combined heterostructures, Chemical Society Reviews, 46 (2017) 3716-3769.

[15] J.R. Bolton, S.J. Strickler, J.S. Connolly, Limiting and realizable efficiencies of solar photolysis of water, Nature, 316 (1985) 495-500.

[16] A.B. Murphy, P.R.F. Barnes, L.K. Randeniya, I.C. Plumb, I.E. Grey, M.D. Horne, J.A. Glasscock, Efficiency of solar water splitting using semiconductor electrodes, Int J Hydrogen Energ, 31 (2006) 1999-2017.

[17] A. Raveendran, M. Chandran, R. Dhanusuraman, A comprehensive review on the electrochemical parameters and recent material development of electrochemical water splitting electrocatalysts, RSC Advances, 13 (2023) 3843-3876.

[18] K.J. Pyper, J.E. Yourey, B.M. Bartlett, Reactivity of $CuWO_4$ in Photoelectrochemical Water Oxidation Is Dictated by a Midgap Electronic State, The Journal of Physical Chemistry C, 117 (2013) 24726-24732.

[19] D.K. Lee, D. Lee, M.A. Lumley, K.-S. Choi, Progress on ternary oxide-based photoanodes for use in photoelectrochemical cells for solar water splitting, Chemical Society Reviews, 48 (2019) 2126-2157.

[20] J. Yang, C. Li, P. Diao, Molybdenum doped $CuWO_4$ nanoflake array films as an efficient photoanode for solar water splitting, Electrochimica Acta, 308 (2019) 195-205.

[21] G. Wang, H. Wang, Y. Ling, Y. Tang, X. Yang, R.C. Fitzmorris, C. Wang, J.Z. Zhang, Y. Li, Hydrogen-Treated TiO_2 Nanowire Arrays for Photoelectrochemical Water Splitting, Nano Letters, 11 (2011) 3026-3033.

[22] D.H. Taffa, I. Hamm, C. Dunkel, I. Sinev, D. Bahnemann, M. Wark, Electrochemical deposition of Fe_2O_3 in the presence of organic additives: a route to enhanced photoactivity, RSC Advances, 5 (2015) 103512-103522.

[23] X. Yang, A. Wolcott, G. Wang, A. Sobo, R.C. Fitzmorris, F. Qian, J.Z. Zhang, Y. Li, Nitrogen-Doped ZnO Nanowire Arrays for Photoelectrochemical Water Splitting, Nano Letters, 9 (2009) 2331-2336.

[24] J.C. Hill, K.-S. Choi, Effect of Electrolytes on the Selectivity and Stability of n-type WO_3 Photoelectrodes for Use in Solar Water Oxidation, The Journal of Physical Chemistry C, 116 (2012) 7612-7620.

[25] J. Ke, M. Adnan Younis, Y. Kong, H. Zhou, J. Liu, L. Lei, Y. Hou, Nanostructured Ternary Metal Tungstate-Based Photocatalysts for Environmental Purification and Solar Water Splitting: A Review, Nano-Micro Letters, 10 (2018) 69.

[26] D.K. Zhong, M. Cornuz, K. Sivula, M. Grätzel, D.R. Gamelin, Photo-assisted electrodeposition of cobalt–phosphate (Co–Pi) catalyst on hematite photoanodes for solar water oxidation, Energy & Environmental Science, 4 (2011) 1759-1764.

[27] C. Li, P. Diao, Boosting the Activity and Stability of Copper Tungsten Nanoflakes toward Solar Water Oxidation by Iridium-Cobalt Phosphates Modification, Catalysts, 2020.

[28] F. Zhan, J. Li, W. Li, Y. Liu, R. Xie, Y. Yang, Y. Li, Q. Chen, In situ formation of $CuWO_4/WO_3$ heterojunction plates array films with enhanced photoelectrochemical properties, Int J Hydrogen Energ, 40 (2015) 6512-6520.

[29] J.E. Yourey, B.M. Bartlett, Electrochemical deposition and photoelectrochemistry of $CuWO_4$, a promising photoanode for water oxidation, Journal of Materials Chemistry, 21 (2011) 7651-7660.

[30] B. Babu, S.G. Peera, K. Yoo, Fabrication of $ZnWO_4$-SnO_2 Core–Shell Nanorods for Enhanced Solar Light-Driven Photoelectrochemical Performance, Inorganics, 2023.

[31] G. Dong, Y. Zhang, W. Wang, L. Wang, Y. Bi, Facile Fabrication of Nanoporous Bi_2WO_6 Photoanodes for Efficient Solar Water Splitting, Energy Technology, 5 (2017) 1912-1918.

[32] C. Janáky, K. Rajeshwar, N.R. de Tacconi, W. Chanmanee, M.N. Huda, Tungsten-based oxide semiconductors for solar hydrogen generation, Catalysis Today, 199 (2013) 53-64.

[33] J.E. Yourey, K.J. Pyper, J.B. Kurtz, B.M. Bartlett, Chemical Stability of $CuWO_4$ for Photoelectrochemical Water Oxidation, The Journal of Physical Chemistry C, 117 (2013) 8708-8718.

[34] C.R. Lhermitte, B.M. Bartlett, Advancing the Chemistry of $CuWO_4$ for Photoelectrochemical Water Oxidation, Accounts of Chemical Research, 49 (2016) 1121-1129.

[35] O.Y. Khyzhun, T. Strunskus, S. Cramm, Y.M. Solonin, Electronic structure of $CuWO_4$: XPS, XES and NEXAFS studies, Journal of Alloys and Compounds, 389 (2005) 14-20.

[36] O.Y. Khyzhun, V.L. Bekenev, Y.M. Solonin, First-principles calculations and X-ray spectroscopy studies of the electronic structure of $CuWO_4$, Journal of Alloys and Compounds, 480 (2009) 184-189.

[37] N. Gaillard, Y. Chang, A. Braun, A. DeAngelis, Copper Tungstate ($CuWO_4$)–Based Materials for Photoelectrochemical Hydrogen Production, MRS Online Proceedings Library, 1446 (2012) 31-36.

[38] Z. Liu, Q. Song, M. Zhou, Z. Guo, J. Kang, H. Yan, Synergistic enhancement of charge management and surface reaction kinetics by spatially separated cocatalysts and p-n heterojunctions in Pt/$CuWO_4$/Co_3O_4 photoanode, Chemical Engineering Journal, 374 (2019) 554-563.

[39] S.K. Pilli, T.G. Deutsch, T.E. Furtak, L.D. Brown, J.A. Turner, A.M. Herring, $BiVO_4$/$CuWO_4$ heterojunction photoanodes for efficient solar driven water oxidation, Physical Chemistry Chemical Physics, 15 (2013) 3273-3278.

[40] K. Li, C. Zhang, X. Li, Y. Du, P. Yang, M. Zhu, A nanostructured $CuWO_4$/Mn_3O_4 with p/n heterojunction as photoanode toward enhanced water oxidation, Catalysis Today, 335 (2019) 173-179.

[41] D. Wang, P.S. Bassi, H. Qi, X. Zhao, Gurudayal, L.H. Wong, R. Xu, T. Sritharan, Z. Chen, Improved Charge Separation in WO_3/$CuWO_4$ Composite Photoanodes for Photoelectrochemical Water Oxidation, Materials, 2016.

[42] N. Gaillard, Y. Chang, A. DeAngelis, S. Higgins, A. Braun, A nanocomposite photoelectrode made of 2.2 eV band gap copper tungstate ($CuWO_4$) and multi-wall carbon nanotubes for solar-assisted water splitting, Int J Hydrogen Energ, 38 (2013) 3166-3176.

[43] M. Valenti, D. Dolat, G. Biskos, A. Schmidt-Ott, W.A. Smith, Enhancement of the Photoelectrochemical Performance of $CuWO_4$ Thin Films for Solar Water Splitting by Plasmonic Nanoparticle Functionalization, The Journal of Physical Chemistry C, 119 (2015) 2096-2104.

[44] R. Salimi, A.A. Sabbagh Alvani, B.T. Mei, N. Naseri, S.F. Du, G. Mul, Ag-Functionalized $CuWO_4$/WO_3 nanocomposites for solar water splitting, New Journal of Chemistry, 43 (2019) 2196-2203.

[45] Z. Chen, M. Löber, A. Rokicińska, Z. Ma, J. Chen, P. Kuśtrowski, H.-J. Meyer, R. Dronskowski, A. Slabon, Increased photocurrent of $CuWO_4$ photoanodes by modification with the oxide carbodiimide $Sn_2O(NCN)$, Dalton Transactions, 49 (2020) 3450-3456.

[46] M. Davi, A. Drichel, M. Mann, T. Scholz, F. Schrader, A. Rokicinska, P. Kustrowski, R. Dronskowski, A. Slabon, Enhanced Photoelectrochemical Water Oxidation Efficiency of $CuWO_4$ Photoanodes by Surface Modification with Ag_2NCN, The Journal of Physical Chemistry C, 121 (2017) 26265-26274.

[47] W. Guo, Y. Wang, X. Lian, Y. Nie, S. Tian, S. Wang, Y. Zhou, G. Henkelman, Insights into the multiple effects of oxygen vacancies on $CuWO_4$ for photoelectrochemical water oxidation, Catalysis Science & Technology, 10 (2020) 7344-7351.

[48] Y. Tang, N. Rong, F. Liu, M. Chu, H. Dong, Y. Zhang, P. Xiao, Enhancement of the photoelectrochemical performance of $CuWO_4$ films for water splitting by hydrogen treatment, Applied Surface Science, 361 (2016) 133-140.

[49] A. Polo, C. Nomellini, I. Grigioni, M.V. Dozzi, E. Selli, Effective Visible Light Exploitation by Copper Molybdo-tungstate Photoanodes, ACS Applied Energy Materials, 3 (2020) 6956-6964.

[50] X. Chang, T. Wang, P. Zhang, J. Zhang, A. Li, J. Gong, Enhanced Surface Reaction Kinetics and Charge Separation of p–n Heterojunction $Co_3O_4/BiVO_4$ Photoanodes, Journal of the American Chemical Society, 137 (2015) 8356-8359.

[51] X.-T. Xu, L. Pan, X. Zhang, L. Wang, J.-J. Zou, Rational Design and Construction of Cocatalysts for Semiconductor-Based Photo-Electrochemical Oxygen Evolution: A Comprehensive Review, Advanced Science, 6 (2019) 1801505.

[52] M.W. Kanan, Y. Surendranath, D.G. Nocera, Cobalt–phosphate oxygen-evolving compound, Chemical Society Reviews, 38 (2009) 109-114.

[53] S. Chen, M.N. Hossain, A. Chen, Significant Enhancement of the Photoelectrochemical Activity of $CuWO_4$ by using a Cobalt Phosphate Nanoscale Thin Film, ChemElectroChem, 5 (2018) 523-530.

[54] X. Xiong, L. Fan, G. Chen, Y. Wang, C. Wu, D. Chen, Y. Lin, T. Li, S. Fu, S. Ren, Boosting water oxidation performance of $CuWO_4$ photoanode by surface modification of nickel phosphate, Electrochimica Acta, 328 (2019) 135125.

[55] E. Fabbri, A. Habereder, K. Waltar, R. Kötz, T.J. Schmidt, Developments and perspectives of oxide-based catalysts for the oxygen evolution reaction, Catalysis Science & Technology, 4 (2014) 3800-3821.

[56] L. Zhang, M. Yang, Z. Luo, J. Zhang, Y. Hou, Photodeposited CoO_x as highly active phases to boost water oxidation on $BiVO_4/WO_3$ photoanode, Int J Hydrogen Energ, 44 (2019) 25652-25661.

[57] X. Zhang, L. An, J. Yin, P. Xi, Z. Zheng, Y. Du, Effective Construction of High-quality Iron Oxy-hydroxides and Co-doped Iron Oxy-hydroxides Nanostructures: Towards the Promising Oxygen Evolution Reaction Application, Scientific Reports, 7 (2017) 43590.

[58] H. Zhang, L. Huang, J. Zhai, S. Dong, Water/Oxygen Circulation-Based Biophotoelectrochemical System for Solar Energy Storage and Release, Journal of the American Chemical Society, 141 (2019) 16416-16421.

[59] X. Chen, Z. Zhang, L. Chi, A.K. Nair, W. Shangguan, Z. Jiang, Recent Advances in Visible-Light-Driven Photoelectrochemical Water Splitting: Catalyst Nanostructures and Reaction Systems, Nano-Micro Letters, 8 (2016) 1-12.

[60] W. Fang, Y. Lin, R. Xv, L. Fu, Boosting Photoelectrochemical Performance of $BiVO_4$ Photoanode by Synergistic Effect of $WO_3/BiVO_4$ Heterojunction Construction and NiOOH Water Oxidation Cocatalyst Modification, ACS Applied Energy Materials, 5 (2022) 11402-11412.

[61] M. Zhou, Z. Liu, X. Li, Z. Liu, Promising Three-Dimensional Flowerlike $CuWO_4$ Photoanode Modified with CdS and FeOOH for Efficient Photoelectrochemical Water Splitting, Industrial & Engineering Chemistry Research, 57 (2018) 6210-6217.

[62] M. Gong, Y. Li, H. Wang, Y. Liang, J.Z. Wu, J. Zhou, J. Wang, T. Regier, F. Wei, H. Dai, An Advanced Ni–Fe Layered Double Hydroxide Electrocatalyst for Water Oxidation, Journal of the American Chemical Society, 135 (2013) 8452-8455.

[63] Z. Cai, X. Bu, P. Wang, J.C. Ho, J. Yang, X. Wang, Recent advances in layered double hydroxide electrocatalysts for the oxygen evolution reaction, Journal of Materials Chemistry A, 7 (2019) 5069-5089.

[64] G. Fan, F. Li, D.G. Evans, X. Duan, Catalytic applications of layered double hydroxides: recent advances and perspectives, Chemical Society Reviews, 43 (2014) 7040-7066.

[65] Q. Wang, D. O'Hare, Recent Advances in the Synthesis and Application of Layered Double Hydroxide (LDH) Nanosheets, Chemical Reviews, 112 (2012) 4124-4155.

[66] H. Liang, F. Meng, M. Cabán-Acevedo, L. Li, A. Forticaux, L. Xiu, Z. Wang, S. Jin, Hydrothermal Continuous Flow Synthesis and Exfoliation of NiCo Layered Double Hydroxide Nanosheets for Enhanced Oxygen Evolution Catalysis, Nano Letters, 15 (2015) 1421-1427.

[67] P. Yue, H. She, L. Zhang, B. Niu, R. Lian, J. Huang, L. Wang, Q. Wang, Super-hydrophilic CoAl-LDH on $BiVO_4$ for enhanced photoelectrochemical water oxidation activity, Applied Catalysis B: Environmental, 286 (2021) 119875.

[68] S. Bai, X. Yang, C. Liu, X. Xiang, R. Luo, J. He, A. Chen, An Integrating Photoanode of WO_3/Fe_2O_3 Heterojunction Decorated with NiFe-LDH to Improve PEC Water Splitting Efficiency, ACS Sustainable Chemistry & Engineering, 6 (2018) 12906-12913.

[69] Y. He, T. Hamann, D. Wang, Thin film photoelectrodes for solar water splitting, Chemical Society Reviews, 48 (2019) 2182-2215.

[70] D. Kang, T.W. Kim, S.R. Kubota, A.C. Cardiel, H.G. Cha, K.-S. Choi, Electrochemical Synthesis of Photoelectrodes and Catalysts for Use in Solar Water Splitting, Chemical Reviews, 115 (2015) 12839-12887.

[71] X. Chen, S.S. Mao, Synthesis of Titanium Dioxide (TiO_2) Nanomaterials, ChemInform, 37 (2006).
[72] X. Wang, Z. Li, J. Shi, Y. Yu, One-Dimensional Titanium Dioxide Nanomaterials: Nanowires, Nanorods, and Nanobelts, Chemical Reviews, 114 (2014) 9346-9384.

[73] X. Chen, S.S. Mao, Titanium Dioxide Nanomaterials: Synthesis, Properties, Modifications, and Applications, Chemical Reviews, 107 (2007) 2891-2959.

[74] H. Ahmadian, F.S. Tehrani, M. Aliannezhadi, Hydrothermal synthesis and characterization of WO3 nanostructures: effects of capping agent and pH, Materials Research Express, 6 (2019) 105024.

[75] K. Lee, A. Mazare, P. Schmuki, One-Dimensional Titanium Dioxide Nanomaterials: Nanotubes, Chemical Reviews, 114 (2014) 9385-9454.

[76] H. Han, F. Riboni, F. Karlicky, S. Kment, A. Goswami, P. Sudhagar, J. Yoo, L. Wang, O. Tomanec, M. Petr, O. Haderka, C. Terashima, A. Fujishima, P. Schmuki, R. Zboril, α-Fe_2O_3/TiO_2 3D hierarchical nanostructures for enhanced photoelectrochemical water splitting, Nanoscale, 9 (2017) 134-142.

[77] L. Vayssieres, N. Beermann, S.-E. Lindquist, A. Hagfeldt, Controlled Aqueous Chemical Growth of Oriented Three-Dimensional Crystalline Nanorod Arrays: Application to Iron(III) Oxides, Chemistry of Materials, 13 (2001) 233-235.

[78] K. Sivula, F. Le Formal, M. Grätzel, Solar Water Splitting: Progress Using Hematite (α-Fe_2O_3) Photoelectrodes, ChemSusChem, 4 (2011) 432-449.

[79] L. Bertoluzzi, S. Ma, On the methods of calculation of the charge collection efficiency of dye sensitized solar cells, Physical Chemistry Chemical Physics, 15 (2013) 4283-4285.

[80] J. Zhang, Z. Liu, Z. Liu, Novel WO_3/Sb_2S_3 Heterojunction Photocatalyst Based on WO_3 of Different Morphologies for Enhanced Efficiency in Photoelectrochemical Water Splitting, ACS Applied Materials & Interfaces, 8 (2016) 9684-9691.

[81] S. Xu, D. Fu, K. Song, L. Wang, Z. Yang, W. Yang, H. Hou, One-dimensional WO_3/$BiVO_4$ heterojunction photoanodes for efficient photoelectrochemical water splitting, Chemical Engineering Journal, 349 (2018) 368-375.

[82] S. Hoang, S.P. Berglund, R.R. Fullon, R.L. Minter, C.B. Mullins, Chemical bath deposition of vertically aligned TiO_2 nanoplatelet arrays for solar energy conversion applications, Journal of Materials Chemistry A, 1 (2013) 4307-4315.

[83] M. Ji, J. Cai, Y. Ma, L. Qi, Controlled Growth of Ferrihydrite Branched Nanosheet Arrays and Their Transformation to Hematite Nanosheet Arrays for Photoelectrochemical Water Splitting, ACS Applied Materials & Interfaces, 8 (2016) 3651-3660.

[84] W. Ye, F. Chen, F. Zhao, N. Han, Y. Li, $CuWO_4$ Nanoflake Array-Based Single-Junction and Heterojunction Photoanodes for Photoelectrochemical Water Oxidation, ACS Applied Materials & Interfaces, 8 (2016) 9211-9217.

[85] C. Cheng, H.J. Fan, Branched nanowires: Synthesis and energy applications, Nano Today, 7 (2012) 327-343.

[86] P.-F. Yin, T. Ling, Y.-R. Lu, Z.-W. Xu, S.-Z. Qiao, X.-W. Du, CdS Nanoflake Arrays for Highly Efficient Light Trapping, Advanced Materials, 27 (2015) 740-745.

[87] X. Gao, L. Jiang, Water-repellent legs of water striders, Nature, 432 (2004) 36-36.

[88] H. Wang, Investigations into Carbon Nitrides and Carbon Nitride Derivatives, Ludwig-Maximilians-Universität München, 2013.

[89] B.J. Inkson, Materials Characterization Using Nondestructive Evaluation (NDE) Methods, Woodhead Publishing2016.

[90] M.A.R. M. Abd Mutalib, M.H.D. Othman, A.F. Ismail, J. Jaafar, Membrane Characterization, Elsevier2017.

[91] J. Kampmann, Designing Semiconductors and Catalysts for Photoelectrochemical Hydrogen Production, Ludwig-Maximilians-Universität München, 2020.

[92] J.F. Moulder, W.F. Stickle, P.E. Sobol, K.D. Bomben, Handbook of X-ray Photoelectron Spectroscopy, Perkin-Elmer Corporation1992.

[93] W.D.K. D. Brandon, Microstructural Characterization of Materials, John Wiley & Sons Ltd2008.

[94] J.D. Andrade, X-ray Photoelectron Spectroscopy (XPS), in: J.D. Andrade (Ed.) Surface and Interfacial Aspects of Biomedical Polymers: Volume 1 Surface Chemistry and Physics, Springer US, Boston, MA, 1985, pp. 105-195.

[95] J. Tauc, Optical properties and electronic structure of amorphous Ge and Si, Materials Research Bulletin, 3 (1968) 37-46.

[96] A.P. Finlayson, V.N. Tsaneva, L. Lyons, M. Clark, B.A. Glowacki, Evaluation of Bi–W-oxides for visible light photocatalysis, physica status solidi (a), 203 (2006) 327-335.

[97] F.A. Settle, Handbook of Instrumental Techniques for Analytical Chemistry, Prentice Hall1997.

[98] G.S. Bumbrah, R.M. Sharma, Raman spectroscopy – Basic principle, instrumentation and selected applications for the characterization of drugs of abuse, Egyptian Journal of Forensic Sciences, 6 (2016) 209-215.

[99] C. Jiang, Novel electrocatalysts for the electrochemical and photoelectrochemical water oxidation reaction, University College London, 2019.

[100] J.R. Connolly, Introduction to X-ray Powder Diffraction, 2005.

[101] J. Brentano, Focussing method of crystal powder analysis by X-rays, Proceedings of the Physical Society of London, 37 (1924) 184.

[102] D.M. J. Als-Nielsen, Elements of Modern X-ray Physics, Second Edition, John Wiley & Sons, Ltd2011.

[103] M. F.Toney, Encyclopedia Of Materials Characterization Surfaces, Interfaces, Thin Films, Butxetworch-Heinemann1992.

[104] I. Stabrawa, A. Kubala-Kukuś, D. Banaś, G. Pepponi, J. Braziewicz, M. Pajek, M. Teodorczyk, Characterization of the morphology of titanium and titanium (IV) oxide nanolayers deposited on different substrates by application of grazing incidence X-ray diffraction and X-ray reflectometry techniques, Thin Solid Films, 671 (2019) 103-110.

[105] M. Kato, J.Z. Zhang, N. Paul, E. Reisner, Protein film photoelectrochemistry of the water oxidation enzyme photosystem II, Chemical Society Reviews, 43 (2014) 6485-6497.

[106] Z. Chen, T.F. Jaramillo, T.G. Deutsch, A. Kleiman-Shwarsctein, A.J. Forman, N. Gaillard, R. Garland, K. Takanabe, C. Heske, M. Sunkara, E.W. McFarland, K. Domen, E.L. Miller, J.A. Turner, H.N. Dinh, Accelerating materials development for photoelectrochemical hydrogen production: Standards for methods, definitions, and reporting protocols, Journal of Materials Research, 25 (2010) 3-16.

[107] Z.C.H.N. Dinh, E. Miller, Photoelectrochemical Water Splitting Standards, Experimental Methods, and Protocols, Springer 2013.

[108] E. Gent, Self-powered Solar-driven Water Splitting Photoelectrochemical Cell by a Hematite Photoanode in Tandem with an Organic Solar Cell, University of Oldenburg, 2016.

[109] M.G. Roel van de Krol, Photoelectrochemical Hydrogen Production, Springer 2012.

[110] P.M. Rao, I.S. Cho, X. Zheng, Flame synthesis of WO_3 nanotubes and nanowires for efficient photoelectrochemical water-splitting, Proceedings of the Combustion Institute, 34 (2013) 2187-2195.

[111] I.S. Cho, C.H. Lee, Y. Feng, M. Logar, P.M. Rao, L. Cai, D.R. Kim, R. Sinclair, X. Zheng, Codoping titanium dioxide nanowires with tungsten and carbon for enhanced photoelectrochemical performance, Nature Communications, 4 (2013) 1723.

[112] X. Shi, K. Zhang, K. Shin, J.H. Moon, T.-W. Lee, J.H. Park, Constructing inverse opal structured hematite photoanodes via electrochemical process and their application to photoelectrochemical water splitting, Physical Chemistry Chemical Physics, 15 (2013) 11717-11722.

[113] P.M. Rao, L. Cai, C. Liu, I.S. Cho, C.H. Lee, J.M. Weisse, P. Yang, X. Zheng, Simultaneously Efficient Light Absorption and Charge Separation in WO_3/$BiVO_4$ Core/Shell Nanowire Photoanode for Photoelectrochemical Water Oxidation, Nano Letters, 14 (2014) 1099-1105.

[114] X. Shi, L. Cai, M. Ma, X. Zheng, J.H. Park, General Characterization Methods for Photoelectrochemical Cells for Solar Water Splitting, ChemSusChem, 8 (2015) 3192-3203.

[115] J. Gan, X. Lu, Y. Tong, Towards highly efficient photoanodes: boosting sunlight-driven semiconductor nanomaterials for water oxidation, Nanoscale, 6 (2014) 7142-7164.

[116] T.W. Kim, K.-S. Choi, Nanoporous $BiVO_4$ photoanodes with dual-layer oxygen evolution catalysts for solar water splitting, Science (New York, N.Y.), 343 (2014) 990-994.

[117] G.V. Govindaraju, G.P. Wheeler, D. Lee, K.-S. Choi, Methods for Electrochemical Synthesis and Photoelectrochemical Characterization for Photoelectrodes, Chemistry of Materials, 29 (2017) 355-370.

[118] X. Zhu, N. Guijarro, Y. Liu, P. Schouwink, R.A. Wells, F. Le Formal, S. Sun, C. Gao, K. Sivula, Spinel Structural Disorder Influences Solar-Water-Splitting Performance of $ZnFe_2O4$ Nanorod Photoanodes, Advanced Materials, 30 (2018) 1801612.

[119] J. Hou, Z. Wang, C. Yang, H. Cheng, S. Jiao, H. Zhu, Cobalt-bilayer catalyst decorated Ta_3N_5 nanorod arrays as integrated electrodes for photoelectrochemical water oxidation, Energy & Environmental Science, 6 (2013) 3322-3330.

[120] W.P. Gomes, D. Vanmaekelbergh, Impedance spectroscopy at semiconductor electrodes: Review and recent developments, Electrochimica Acta, 41 (1996) 967-973.

[121] J. Aguedo, L. Lorencova, M. Barath, P. Farkas, J. Tkac, Electrochemical Impedance Spectroscopy on 2D Nanomaterial MXene Modified Interfaces: Application as a Characterization and Transducing Tool, Chemosensors, 2020.

[122] A. Banerjee, B. Mondal, A. Verma, V.R. Satsangi, R. Shrivastav, A. Dey, S. Dass, Enhancing efficiency of Fe_2O_3 for robust and proficient solar water splitting using a highly dispersed bioinspired catalyst, Journal of Catalysis, 352 (2017) 83-92.

[123] A.W. Bott, Electrochemistry of Semiconductors, (1998).

[124] A.J. Nozik, Photoelectrochemistry: Applications to Solar Energy Conversion, Annual Review of Physical Chemistry, 29 (1978) 189-222.

[125] P.H. Karpinski, J.S. Wey, 6 - Precipitation processes, in: A.S. Myerson (Ed.) Handbook of Industrial Crystallization (Second Edition), Butterworth-Heinemann, Woburn, 2002, pp. 141-160.

[126] Y. Gao, K. Koumoto, Bioinspired Ceramic Thin Film Processing: Present Status and Future Perspectives, Crystal Growth & Design, 5 (2005) 1983-2017.

[127] T. Wang, X. Fan, B. Gao, C. Jiang, Y. Li, P. Li, S. Zhang, X. Huang, J. He, Self-Assembled Urchin-Like $CuWO_4/WO_3$ Heterojunction Nanoarrays as Photoanodes for Photoelectrochemical Water Splitting, ChemElectroChem, 8 (2021) 125-134.

[128] A.E.B. Lima, M.J.S. Costa, R.S. Santos, N.C. Batista, L.S. Cavalcante, E. Longo, G.E. Luz, Facile preparation of $CuWO_4$ porous films and their photoelectrochemical properties, Electrochimica Acta, 256 (2017) 139-145.

[129] M. Antoniadou, M.K. Arfanis, I. Ibrahim, P. Falaras, Bifunctional g-C_3N_4/WO_3 Thin Films for Photocatalytic Water Purification, Water, 2019.

[130] N.S. Murthy, C. Bednarczyk, H. Minor, Depth-profiles of structure in single- and multilayered commercial polymer films using grazing-incidence X-ray diffraction, Polymer, 41 (2000) 277-284.

[131] R. Li, Z. Hu, X. Shao, P. Cheng, S. Li, W. Yu, W. Lin, D. Yuan, Large Scale Synthesis of NiCo Layered Double Hydroxides for Superior Asymmetric Electrochemical Capacitor, Scientific Reports, 6 (2016) 18737.

[132] H. Li, J. Zhang, T. Yang, Y. Wang, H. Gao, X. Wang, Z. Chai, $SnNb_2O_6$/NiCo-LDH Z-scheme heterojunction with regulated oxygen vacancies obtained by engineering the crystallinity for efficient and renewable photocatalytic H_2 evolution, Catalysis Science & Technology, 11 (2021) 6281-6290.

[133] S. A, B. T, G. V, S. D, N. Kulal, S. A, Framework of ruthenium-containing nickel hydrotalcite-type material: preparation, characterisation, and its catalytic application, RSC Advances, 8 (2018) 25248-25257.

[134] W. Wang, K. Feng, Z. Wang, Y. Ma, S. Zhang, Y. Liang, Controllable synthesis and growth mechanism of α-$Co(OH)_2$ nanorods and nanoplates by a facile solution-phase route, Journal of Solid State Chemistry, 184 (2011) 3299-3302.

[135] D. Zhang, X. Tang, Z. Yang, Y. Yang, H. Li, Construction of honeycomb-like Te-doped NiCo-LDHs for aqueous supercapacitors and as oxygen evolution reaction electrocatalysts, Materials Advances, 3 (2022) 1286-1294.

[136] J. Yang, C. Yu, C. Hu, M. Wang, S. Li, H. Huang, K. Bustillo, X. Han, C. Zhao, W. Guo, Z. Zeng, H. Zheng, J. Qiu, Surface-Confined Fabrication of Ultrathin Nickel Cobalt-Layered Double Hydroxide Nanosheets for High-Performance Supercapacitors, Advanced Functional Materials, 28 (2018) 1803272.

[137] B. Patil, C. Park, H. Ahn, Scalable nanohybrids of graphitic carbon nitride and layered NiCo hydroxide for high supercapacitive performance, RSC Advances, 9 (2019) 33643-33652.

[138] C.-H. Lin, H.-L. Chu, W.-S. Hwang, M.-C. Wang, H.-H. Ko, Synthesis and optical properties of Mg-Al layered double hydroxides precursor powders, AIP Advances, 7 (2017).

[139] H.N. Dhandapani, D. Mahendiran, A. Karmakar, P. Devi, S. Nagappan, R. Madhu, K. Bera, P. Murugan, B.R. Babu, S. Kundu, Boosting of overall water splitting activity by regulating the electron distribution over the active sites of Ce doped NiCo–LDH and atomic level understanding of the catalyst by DFT study, Journal of Materials Chemistry A, 10 (2022) 17488-17500.

[140] Z. Liu, R. Ma, M. Osada, K. Takada, T. Sasaki, Selective and Controlled Synthesis of α- and β-Cobalt Hydroxides in Highly Developed Hexagonal Platelets, Journal of the American Chemical Society, 127 (2005) 13869-13874.

[141] J.P. Cheng, L. Liu, J. Zhang, F. Liu, X.B. Zhang, Influences of anion exchange and phase transformation on the supercapacitive properties of α-$Co(OH)_2$, Journal of Electroanalytical Chemistry, 722-723 (2014) 23-31.

[142] A.P. Grosvenor, M.C. Biesinger, R.S.C. Smart, N.S. McIntyre, New interpretations of XPS spectra of nickel metal and oxides, Surface Science, 600 (2006) 1771-1779.

[143] J. Huang, G. Hu, Y. Ding, M. Pang, B. Ma, Mn-doping and NiFe layered double hydroxide coating: Effective approaches to enhancing the performance of α-Fe_2O_3 in photoelectrochemical water oxidation, Journal of Catalysis, 340 (2016) 261-269.

[144] M.C. Biesinger, B.P. Payne, A.P. Grosvenor, L.W.M. Lau, A.R. Gerson, R.S.C. Smart, Resolving surface chemical states in XPS analysis of first row transition metals, oxides and hydroxides: Cr, Mn, Fe, Co and Ni, Applied Surface Science, 257 (2011) 2717-2730.

[145] G. Wang, B. Wang, C. Su, D. Li, L. Zhang, R. Chong, Z. Chang, Enhancing and stabilizing α-Fe_2O_3 photoanode towards neutral water oxidation: Introducing a dual-functional NiCoAl layered double hydroxide overlayer, Journal of Catalysis, 359 (2018) 287-295.

[146] X. Dai, Y. Dai, J. Lu, L. Pu, W. Wang, J. Jin, F. Ma, N. Tie, Cobalt oxide nanocomposites modified by NiCo-layered double hydroxide nanosheets as advanced electrodes for supercapacitors, Ionics, 26 (2020) 2501-2511.

[147] T. Zhu, M.N. Chong, E.S. Chan, J.D. Ocon, Electrochemically-synthesized tungstate nanocomposites γ-WO_3/$CuWO_4$ and γ-WO_3/$NiWO_4$ thin films with improved band gap and photoactivity for solar-driven photoelectrochemical water oxidation, Journal of Alloys and Compounds, 762 (2018) 90-97.

[148] C. Mahala, M.D. Sharma, M. Basu, 2D Nanostructures of $CoFe_2O_4$ and $NiFe_2O_4$: Efficient Oxygen Evolution Catalyst, Electrochimica Acta, 273 (2018) 462-473.

[149] T.-G. Vo, K.-F. Chang, C.-Y. Chiang, Valence modulation on zinc-cobalt-vanadium layered double hydroxide nanosheet for accelerating $BiVO_4$ photoelectrochemical water oxidation, Journal of Catalysis, 391 (2020) 336-345.

[150] J. Guo, C. Mao, R. Zhang, M. Shao, M. Wei, P. Feng, Reduced titania@layered double hydroxide hybrid photoanodes for enhanced photoelectrochemical water oxidation, Journal of Materials Chemistry A, 5 (2017) 11016-11025.

[151] J.C. Hill, Y. Ping, G.A. Galli, K.-S. Choi, Synthesis, photoelectrochemical properties, and first principles study of n-type $CuW_{1-x}Mo_xO_4$ electrodes showing enhanced visible light absorption, Energy & Environmental Science, 6 (2013) 2440-2446.

[152] D. Bohra, W.A. Smith, Improved charge separation via Fe-doping of copper tungstate photoanodes, Physical Chemistry Chemical Physics, 17 (2015) 9857-9866.

[153] C. Li, B. Guo, B. Peng, C. Yue, P. Diao, Copper Tungstate ($CuWO_4$) Nanoflakes Coupled with Cobalt Phosphate (Co-Pi) for Effective Photoelectrochemical Water Splitting, International Journal of Electrochemical Science, 14 (2019) 9017-9029.

[154] C. Wang, X. Long, S. Wei, T. Wang, F. Li, L. Gao, Y. Hu, S. Li, J. Jin, Conformally Coupling CoAl-Layered Double Hydroxides on Fluorine-Doped Hematite: Surface and Bulk Co-Modification for Enhanced Photoelectrochemical Water Oxidation, ACS Applied Materials & Interfaces, 11 (2019) 29799-29806.

[155] L. Sun, J. Sun, X. Yang, S. Bai, Y. Feng, R. Luo, D. Li, A. Chen, An integrating photoanode consisting of $BiVO_4$, rGO and LDH for photoelectrochemical water splitting, Dalton Transactions, 48 (2019) 16091-16098.

[156] S. Bai, J. Han, K. Zhang, J. Sun, J. Guo, R. Luo, D. Li, A. Chen, Triadic Layered Double Hydroxide Modified Semiconductor Heterojunction for PEC Water Splitting, ACS Sustainable Chemistry & Engineering, 8 (2020) 4076-4084.

8 Abbreviations and symbols

Abbreviation	Full name
1-D	one-dimensional
2-D	two-dimensional
3-D	three-dimensional
A	absorptance, photoactive area
ABPE	applied bias photon-to-current efficiency
ALD	atomic layer deposition
APCE	absorbed photon-to-current efficiency
AM 1.5G	air mass 1.5 global
a.u.	arbitrary unit
c_{elec}	concentration electrolyte
C	capacity
CA	chronoamperometry
CB	conduction band
CBD	chemical bath deposition
CE	counter electrode
C_{elec}	concentration electrolyte
CLV	chopped light voltammetry
Co-Pi	cobalt phosphate
CV	cyclic voltammetry
CVD	chemical vapor deposition
DC	direct current
DI	water de-ionized
e^-	electron
e^-/h^+	electron/hole pair
E	potential
EC	electrochemistry
EDS	energy dispersive X-ray spectroscopy
$E_{Ag/AgCl(sat.\ KCl)}$	potential against the redox couple Ag/AgCl(sat. KCl)
E_{app}	applied bias potential
E_b	binding energy
E_{CB}	conduction band edge
E_f	fermi level
E_{fb}	flat band potential
E_g	band gap energy
E_{kin}	kinetic energy
E_{vac}	vacuum energy
E_{VB}	valence band edge
$E^0_{X/Y}$	standard redox potential of a redox couple X/Y
$E_{X/Y}$	measured redox potential of a redox couple X/Y
EA	elemental analysis
ED	electrochemical deposition
EI	electronic ionization
EIS	electrochemical impedance spectroscopy
F	faraday's constant

Fig.	figure
FSI	front-side illumination
FTO	fluorine-doped tin oxide ($F:SnO_2$)
FT-IR	fourier transform infrared spectroscopy
h^+	hole
h	planck constant
HER	hydrogen evolution reaction
HT	hydrothermal
I_{ph}	photocurrent
IPCE	incident photon-to-electron conversion efficiency
IQE	internal quantum efficiency
ITO	indium tin oxide
$J_{1.23V.RHE}$	photocurrent density at 1.23 V vs. RHE
J_{abs}	photon absorption rate
J_{SC}	short circuit current density
J_{ph}	photocurrent density
J_{max}	theoretical maximum photocurrent
$J_{sulfite}$	the maximal photocurrent in sulfite elecyrolyte
k_B	boltzmann constant
LDH	layered double hydroxide
LED	light emitting devices
LHE	light harvesting efficiency
LSV	linear sweeping voltammetry
MS	mott-Schottky
NHE	normal hydrogen electrode
N_D	the number of donors
Ns	number of surface atoms
OEC	oxygen evolution catalyst
OER	oxygen evolution reaction
Pin	incident (solar) power flux
PA	photoanode
PBS	phosphate buffer solution
PC	photocathode
PEC	photoelectrochemical
PED	photoelectrochemical deposition
PV	photovoltaic
Q	amount of charge
R	reflectance or resistance
RE	reference electrode
RHE	reversible hydrogen electrode
RT	room temperature
$R_{ct,ss}$	charge-transfer resistance at the surface-electrolyte interface
R_s	resistance from the bulk thin film, the electrolyte, and the electrical contacts
R_{trap}	resistance of trapped electrons at the surface
SCE	saturated calomel electrodes
SEM	scanning electron microscopy
STH	solar-to-hydrogen conversion
T	absolute temperature or transmission
TCO	transparent conductive oxides

UHV	ultrahigh vacuum
UV-vis	ultraviolet–visible spectroscopy
VB	valence band
VOC	open circuit potential
VRHE	potential against the reversible hydrogen electrode
WD	width of depletion layer
WE	working electrode
XPS	X-ray photoelectron spectroscopy
XRD	X-ray diffraction
η_{abs}	light absorption efficiency
$\eta_{bul}k$	charge separation efficiency in bulk
$\eta_{surface}$	charge transfer efficiency on the surface
η_{OER}	overpotential of oxygen evolution reaction
λ	wavelength
τ	carrier lifetime

9 Declaration

I hereby declare that this thesis is my summary of original PhD work and has not been presented or submitted to any other University. All the sources and materials used in this thesis are duly acknowledged and cited.

Sima Nouhi